Theses and Dissertations--Mechanical Engineering

Mechanical Engineering

2015

EFFECTS OF MAGNETIC FIELD ON THE SHAPE MEMORY BEHAVIOR OF SINGLE AND POLYCRYSTALLINE MAGNETIC SHAPE MEMORY ALLOYS

Ali S. Turabi

University of Kentucky, sadi.turabi@uky.edu

Click here to let us know how access to this document benefits you.

Recommended Citation

STUDENT AGREEMENT:

I represent that my thesis or dissertation and abstract are my original work. Proper attribution has been given to all outside sources. I understand that I am solely responsible for obtaining any needed copyright permissions. I have obtained needed written permission statement(s) from the owner(s) of each third-party copyrighted matter to be included in my work, allowing electronic distribution (if such use is not permitted by the fair use doctrine) which will be submitted to UKnowledge as Additional File.

I hereby grant to The University of Kentucky and its agents the irrevocable, non-exclusive, and royalty-free license to archive and make accessible my work in whole or in part in all forms of media, now or hereafter known. I agree that the document mentioned above may be made available immediately for worldwide access unless an embargo applies.

I retain all other ownership rights to the copyright of my work. I also retain the right to use in future works (such as articles or books) all or part of my work. I understand that I am free to register the copyright to my work.

REVIEW, APPROVAL AND ACCEPTANCE

The document mentioned above has been reviewed and accepted by the student's advisor, on behalf of the advisory committee, and by the Director of Graduate Studies (DGS), on behalf of the program; we verify that this is the final, approved version of the student's thesis including all changes required by the advisory committee. The undersigned agree to abide by the statements above.

Ali S. Turabi, Student

Dr. Haluk E. Karaca, Major Professor

Dr. Haluk E. Karaca, Director of Graduate Studies

EFFECTS OF MAGNETIC FIELD ON THE SHAPE MEMORY BEHAVIOR OF SINGLE AND POLYCRYSTALLINE MAGNETIC SHAPE MEMORY ALLOYS

DISSERTATION

A dissertation submitted in partial fulfillment of the

requirements for the degree of Doctor of Philosophy in the

College of Engineering

at the University of Kentucky

By

Ali Sadi Turabi

Lexington, Kentucky

Director: Dr. Haluk E. Karaca, Professor of Mechanical Engineering

Lexington, Kentucky

2015

ABSTRACT OF THE DISSERTATION

EFFECTS OF MAGNETIC FIELD ON THE SHAPE MEMORY
BEHAVIOR OF SINGLE AND POLYCRYSTALLINE MAGNETIC
SHAPE MEMORY ALLOYS

Magnetic Shape Memory Alloys (MSMAs) have the unique ability to change their shape within a magnetic field, or in the presence of stress and a change in temperature. MSMAs have been widely investigated in the past decade due to their ability to demonstrate large magnetic field induced strain and higher frequency response than conventional shape memory alloys (SMAs). NiMn-based alloys are the workhorse of metamagnetic shape memory alloys since they are able to exhibit magnetic field induced phase transformation. In these alloys, martensite and austenite phases have different magnetization behavior, such as the parent phase can be ferromagnetic and martensite phase can be weakly magnetic. The magnetization difference between the transforming phases creates Zeeman energy, which is the main source for magnetic field induced phase transformation, is unlimited with applied field and orientation independent. Thus, metamagnetic shape memory alloys can be employed in polycrystalline form and provide higher actuation stress than conventional MSMAs. High actuation stress levels and frequencies in metamagnetic shape memory alloys are promising for magnetic actuation applications.

Effects of heat treatments and cooling rates on the transformation temperatures, magnetization response and shape memory behavior under compressive stress were explored in $Ni_{45}Mn_{36.5}Co_5In_{13.5}$ [100] oriented single crystalline alloys to obtain high transformation temperatures, large magnetization difference, and low hysteresis behavior. It was found that transformation temperatures increase with higher heat treatment temperatures and decrease drastically at lower cooling rates. Temperature hysteresis decreased with increasing heat treatment temperatures. It was revealed that transformation temperatures, hysteresis, and magnetization response can be tailored by heat treatments via modifying interatomic order.

Magnetic and mechanical results of NiMn-based metamagnetic alloys in single and polycrystalline forms as functions of composition, stress, temperature and magnetic field (up to 9 Tesla) were revealed through thermal-cycling under stress and magnetic field; stress-cycling as functions of temperature and magnetic field; and magnetic-field-cycling under stress at several temperatures experiments. Single crystalline samples of NiMnCoIn showed recoverable strain of 1.5 % due to magnetic field induced reversible phase transformation under constant stress and strain of 3.7 % by magnetic field induced recovery after variant reorientation of martensite. The magnetic field effect on the superelasticity

and shape memory effects were also explored in selected orientations of [100], [110] and [111].

Fe-based ferromagnetic shape memory alloys have received considerable attention due to their better workability, strength, and lower cost compared with commercial NiTi based SMAs. The shape memory properties of a ferrous single crystalline alloy, FeNiCoAlNb, were investigated along the [100] orientation by thermal cycling under constant stress and superelasticity tests in both tension and compression. Aging was used to form nano-size precipitates to demonstrate shape memory behavior and tailor the shape memory properties. It was found that after proper heat treatments, [001] oriented FeNiCoAlNb showed a compressive strain of 15%, low temperature dependent superelastic behavior, high compression-tension asymmetry, and high compressive strength (~3GPa). The orientation dependence of the mechanical properties of FeNiCoAlNb single crystals were investigated along the [100], [110], [012] and [113] orientations. In addition, martensite phase showed higher magnetization than austenite phase as opposed to NiMn-based metamagnetic shape memory alloys. This magnetization difference is promising because it can allow magnetic field induced forward transformation. Ferrous alloys have great potential for high strength, temperature independent, and large scale actuator applications.

KEYWORDS: Shape-Memory Materials, Metamagnetic, Zeeman, Magnetostress, Actuation

Ali Sadi Turabi

Student's Signature

07/21/2015

Date

EFFECTS OF MAGNETIC FIELD ON THE SHAPE MEMORY
BEHAVIOR OF SINGLE AND POLYCRYSTALLINE MAGNETIC
SHAPE MEMORY ALLOYS

By

Ali Sadi Turabi

Haluk E. Karaca

Director of Dissertation

Haluk E. Karaca

Director of Graduate Studies

07/21/2015

This work is dedicated to my parents

ACKNOWLEDGEMENTS

Table of Contents

List of Figures

List of Tables

1   Introduction

1.1   Motivation

Shape memory alloys have been investigated as novel active materials for actuation applications during the past few decades due to their unique features, namely superelasticity and shape memory effect. SMAs can produce large recoverable deformations, generate large forces, and have been widely used in many applications. They have many medical device applications, such as endovascular stents, orthopedic implants, cardiovascular devices, and surgical instruments, due to their shape memory behavior and biocompatibility. The high elasticity and low deformation force of NiTi, for example, make it promising for medical applications. It should be noted that although Ni is extremely toxic, the formation of a passive titanium-oxide layer (TiO_2) in NiTi shape memory alloys results in biocompatible behavior [1, 2].Shape memory alloys are also used as hysteresis-induced damping materials in civil structures [3]. More recently, thin film SMAs have been identified as very promising candidates for micro actuators due to their high work output density. Some interesting applications include micro grippers, micro pumps, micro cantilever switches and scanners [4]. SMA components also exhibit highly nonlinear, loading history and temperature dependent behavior as a result of the inhomogenities of stress and temperature fields in the structures. Typically, SMA actuators are driven by electric current heating and convective cooling to trigger phase transformations between martensite and austenite to generate the actuator deformations/forces. These are strong thermo-mechanically coupled problems because of the latent heat released and absorbed during austenite-martensite phase transformations.

Magnetic shape memory alloys have been widely investigated in the past decade in the interest of their ability to produce large magnetic field induced strain, and show high frequency response [5-8]. NiMnGa alloys are the workhorse of magnetic shape memory alloys that show high magnetic field induced strain (5-10 %) by variant reorientation, and have high thermal stability in single crystalline form [7, 9-11]. In NiMnGa alloys, magnetic actuation occurs by variant reorientation of ferromagnetic martensite phase [9]. Drawbacks of NiMnGa alloys are their brittleness, low actuation stress (due to limited magnetic energy), limited operation temperature, and high orientation dependence [9, 12]. The main magnetic energy source of the variant reorientation mechanism is magnetocrystalline anisotropy energy (MAE), which is limited and does not increase with applied field after a critical value, resulting in low magnetostress values. It should also be noted that NiMnGa alloys can only be utilized in single crystalline or textured forms since MAE is highly orientation dependent, and they are very brittle. Thus, NiMnGa alloys have limited potential for actuator applications

In order to observe magnetic field induced martensitic phase transformation, magnetic driving force should be high enough to move phase fronts or variants. The maximum stress from magnetic energy in NiMnGa alloys is less than 6 MPa, while the required critical stress for phase transformation is an order higher (it is highly temperature dependent). Therefore, magnetic field induced phase transformation is usually omitted in these alloys due to insufficient magnetic energy [9]. Field induced phase transformation in NiMnGa is only possible under special conditions, such as at temperatures very close to A_s or when X-phase, a new phase present before 10M martensite [13], is observed [14, 15].

However, the available magnetic energy for phase transformation is still limited, resulting in low magnetostress values.

NiMn-based metamagnetic shape memory alloys, such as NiMnIn [16], NiMnSn [17], and NiMnCoSb [18] have received much attention since they are able to exhibit magnetic field induced phase transformation. In general, austenite is ferromagnetic and martensite is weakly magnetic in these alloys. Thereby, the difference between the magnetization values of phases creates Zeeman energy, which is the main source of field induced phase transformation. Kainuma et al. [19] reported that in the metamagnetic $Ni_{45}Mn_{36.6}Co_5In_{13.4}$ alloy, phase transformation occurs between 375 K and 390 K from the paramagnetic martensite to ferromagnetic austenite during heating under 0.5 kOe magnetic field. The magnetization difference between austenite and martensite phases increase while transformation temperatures decrease with magnetic field, as shown in figure 1.1.
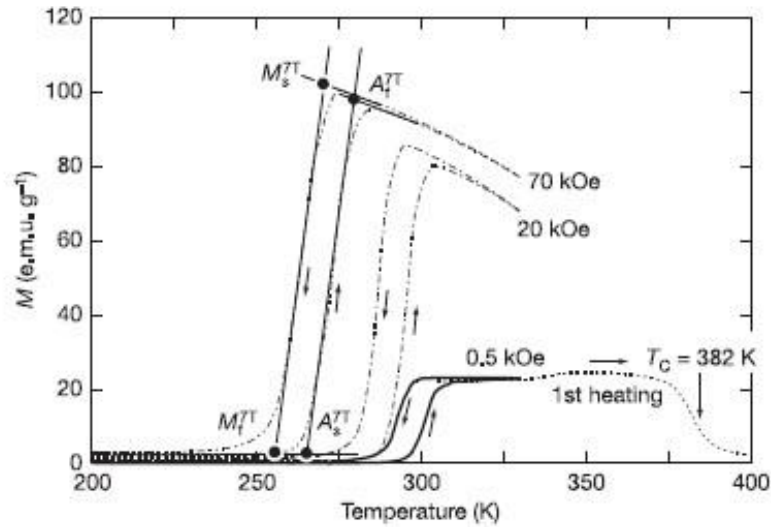
Figure 1.1 Thermo-magnetization curves of the $Ni_{45}Mn_{36.6}Co_5In_{13.4}$ alloy under selected magnetic fields [20].

It should be noted that Zeeman energy increases with applied field, and it is orientation independent. In accordance with this metamagnetic shape memory alloys could work in polycrystalline form and provide higher actuation stress values than conventional NiMnGa alloys. Previously, Karaca et al. observed a high magnetostress value of nearly 30 MPa under 1.6 Tesla in NiMnCoIn alloys which is almost five times higher than what has been observed in NiMnGa alloys (6 MPa) [12], as shown in figure 1.2. Kainuma et al. theoretically calculated the expected magnetostress value as 108 MPa under 7 T for NiMnCoIn metamagnetic shape memory alloys [19]. High actuation stress levels and low hysteresis in metamagnetic shape memory alloys are very attractive for magnetic actuation applications.
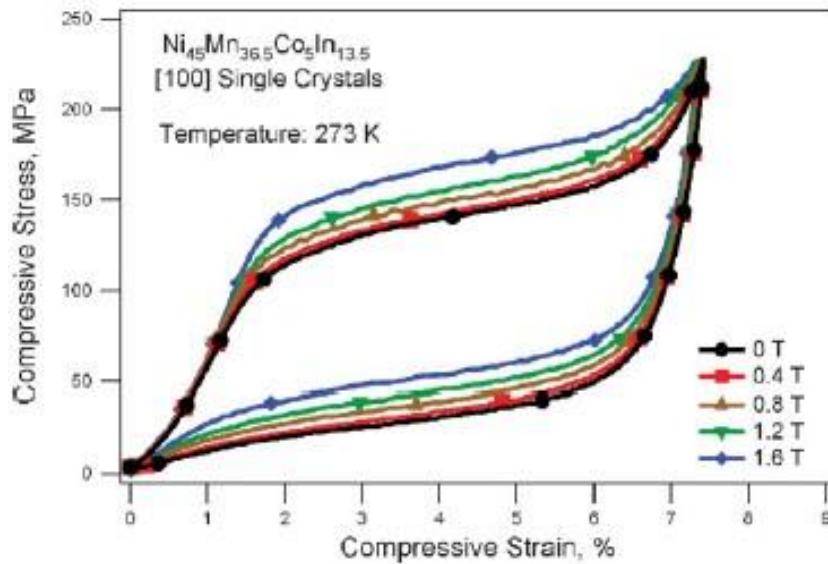
Figure 1.2 Superelastic behavior of $Ni_{45}Mn_{36.5}Co_5In_{13.5}$ single crystalline at selected magnetic fields up to 1.6 Tesla [13].

In order to observe transformation strain in shape memory alloys, favored martensite variants should be formed instead of self-accommodating martensite variants. Since ferromagnetic austenite and weakly magnetic martensite have negligible MAEs, self-

accommodating martensite variants cannot be biased within a magnetic field. Krenke et al. reported that in the absence of applied stress, $Ni_{50}Mn_{34}In_{16}$ polycrystalline alloy exhibits only 0.12 % strain with magnetic superelasticity due to magnetic field induced phase transformation [20]. Liu et al. is also studied the effects of temperature and training of a textured $Ni_{45.2}Mn_{36.7}In_{13}Co_{5.1}$ and maximum magnetostrain was found to be 0.25 % under 5 T magnetic field after magnetic training [21]. Hence, either external stress should be applied or the material should be trained to show two-way shape memory effect to produce large magnetic field induced strain.

Metamagnetic shape memory alloys with magnetic field induced phase transformation mechanism provide many advantages for practical applications by presenting high magnetostress. In literature, magnetostress values were determined by using single crystalline samples because of their brittleness problem. Since the magnetic field induced phase transformation mechanism is orientation independent, ductile polycrystalline materials are required for mechanical characterization. However, they require high magnetic fields (4 Tesla and up) to realize reversible phase transformation [12, 19]. The critical field can be reduced by diminishing thermal hysteresis or by increasing the difference between saturation magnetizations of the transforming phases. Hysteresis is also a strong function of applied stress, and should be characterized before utilizing these materials as magnetic actuators.

Heat treatment is one of the most effective methods to tailor transformation temperatures, temperature hysteresis, and magnetization by changing atomic ordering in magnetic shape memory alloys [22-26]. Ito et al. studied crystal structures and magnetic properties of $Ni_{45}Co_5Mn_{36.7}In_{13.3}$ and found that martensitic transformation was observed

5

from B2 to $L1_0$ by quenching from 923 K while $L2_1$ austenite was transformed to 6M martensite phase in the specimen which was quenched at 623 K. Moreover, atomic ordering plays an important role to change the magnetic response due to interatomic distance change in Mn-Mn spacing and magnetic exchange interactions [23]. Sanches-Alarcos reported that magnetization difference, martensitic transformation temperature was increased and curie temperature was decreased with increasing aging temperature by changing the degree of ordering [25]. In NiMn-based Heusler alloys, degree of ordering is the key parameter to adjust the magnetization response, temperature hysteresis, and transformation temperatures by heat treatment.

Cooling rate is another factor to modify the degree of atomic ordering. Quenching is especially important as it provides rapid cooling and allows the material to partially retain the low atomic order, and can be observed by high temperature quenching in NiMn-based magnetic shape memory alloys. Slow cooling, which is furnace or air cooling, is required to reach long range atomic order [24, 26]. Perez-Landazabal reported that quenching method presented higher disordering than air cooling process in $Ni_{45}Co_5Mn_{36.7}In_{13.3}$ alloys, in results martensitic transformation was increased in quenched specimens.

Practical applications of magnetic shape memory alloys are limited by their extreme brittleness which hinders their use in polycrystalline form. In order to overcome the brittleness obstacle in polycrystalline form, alloying with quaternary elements such as Fe [27, 28], Co [29, 30], Cu [31], and B [32] is employed to alter the mechanical properties of NiMnGa alloys.

Co addition to NiMnGa alloys provides an opportunity to control the Curie temperatures of transforming phases where ferromagnetic austenite can transform to paramagnetic martensite [33, 34]. Co addition also increases the ductility of the alloy through the formation of ductile second phases [30], as shown in figure 1.3. NiMnCoGa alloys can be classified as meta-magnetic SMAs (like NiMnCoIn alloys) where magnetic field induced phase transformation may result in one order of higher actuation stress than that of variant reorientation in NiMnGa alloys.
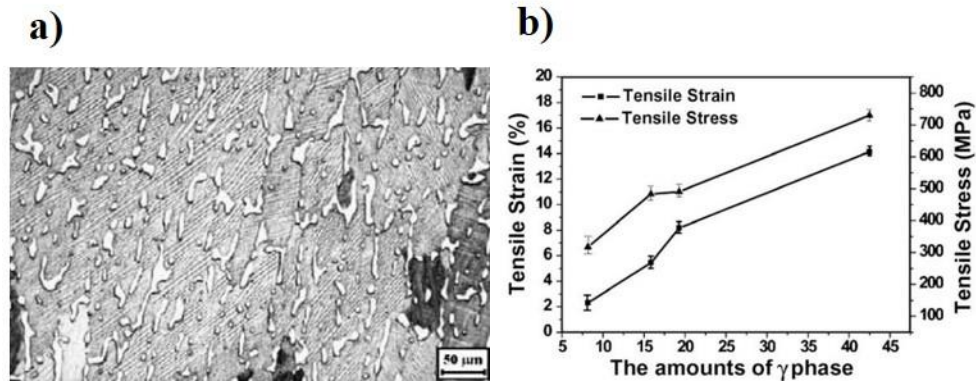
Figure 1.3 a) Optical image of microstructure and b) tensile strain and stress of NiMnCoGa polycrystalline alloys [33].

Moreover, CoNiAl [35, 36], CoNiGa [35], and NiFeGa [37] Heusler alloys were investigated to achieve shape memory properties of NiMnGa with better ductility in polycrystalline form. Recently, Mn rich Mn-Ni-X (Ga, In, Sn) alloys have been investigated due to their high saturation magnetization difference between the transforming phases [38-40]. In Ni-Mn based metamagnetic alloys, magnetization strongly depends on the Mn-Mn interatomic distance. Thus, increasing the Mn content is promising to have higher saturation magnetization which alters Zeeman energy. Liu et al. studied the [100]-oriented Mn_2NiGa single crystals and showed that magnetic field assisted strain of 4 % can

7

be observed when magnetization difference of transforming phases was around 9 emu/g . Wu et al. reported that $Mn_{50}Ni_{37}In_{10}Co_3$ polycrystalline alloy exhibited high saturation magnetization around 118 emu/g in parent phase and the magnetization difference between the transforming phases was 89 emu/g [41]. High magnetization difference of Mn rich alloy systems are promising to improve actuation stress by reason of an increase of Zeeman Energy

In addition to NiMn-based shape memory alloys, ferrous shape memory alloys (FeSMAs), such as Fe-Ni-C [42], Fe-Mn-Si [43, 44], Fe-Mn-Al [45], and Fe-Ni-Co-Ti [46-48] have received considerable attention due to their better workability, weldability, and lower cost compared to the commercially available NiTi based SMAs. They have the potential to be utilized in many industries, such as construction, that requires the employment of a large quantity of materials. The main disadvantages of FeSMAs are that they mostly exhibit non-thermoelastic transformation that results in very large temperature hysteresis (>300 ˚C), and no superelasticity [49]. Composition alteration and precipitation were successfully employed to obtain thermoelastic transformation in FeSMAs with lower temperature hysteresis [50, 51]. However, their recoverable shape memory strains were lower than 3 %. This restrained their application to special cases, like that of large diameter pipe couplings [52, 53].

Although FeSMAs have been known about for a long time, the breakthrough for the alloy design has been achieved by the discovery of FeNiCoAlTaB [53] and FeMnAlNi [54] alloys. FeNiCoAlTaB alloys exhibit high strength (1 GPa), huge superelasticity (13 %), high damping ability, and good plasticity in the polycrystalline form [53], as shown in figure 1.4. With this in mind, it should be noted that they showed these remarkable

properties only after they are alloyed by Boron for grain refinement, textured along the [100] orientation by cold rolling and then precipitation hardened [53].
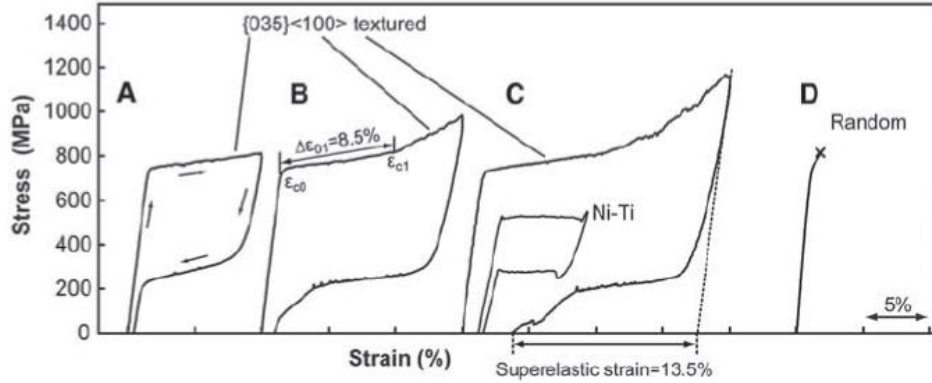
Figure 1.4 Superelastic behavior of FeNiCoAlTaB textured polycrystalline alloys [57].

Later, thermoelastic martensitic transformation and orientation dependence of superelasticity in single crystalline of FeNiCoAlTa was studied by I. Kireeva et al.[55, 56] and they found that these alloys show superelastic strain of 6.8 %, stress hysteresis of 130 MPa and large superelastic temperature interval of 130 ˚C in [001]-oriented single crystalline form in tension [55, 56]. Ma et al. [57] investigated the tension-compression asymmetry along the [100] orientation of FeNiCoAlTa and observed transformation strain of 3.5 % in tension and 2 % in compression. Evirgen et al. [58] studied the effects of aging on FeNiCoAlTa single crystals and revealed superelasticity with 3.4 % tensile strain. The experimental superelastic strains are seen to be lower than theoretical strain levels which is attributed to higher volume fraction of precipitates and lower tetragonality. In addition, FeNiCoAlTa single crystals were reported as a metamagnetic which transformation occurs

9

from strong ferromagnetic martensite to weakly ferromagnetic austenite as opposed to NiMnCoIn alloys, as shown in figure 1.5.
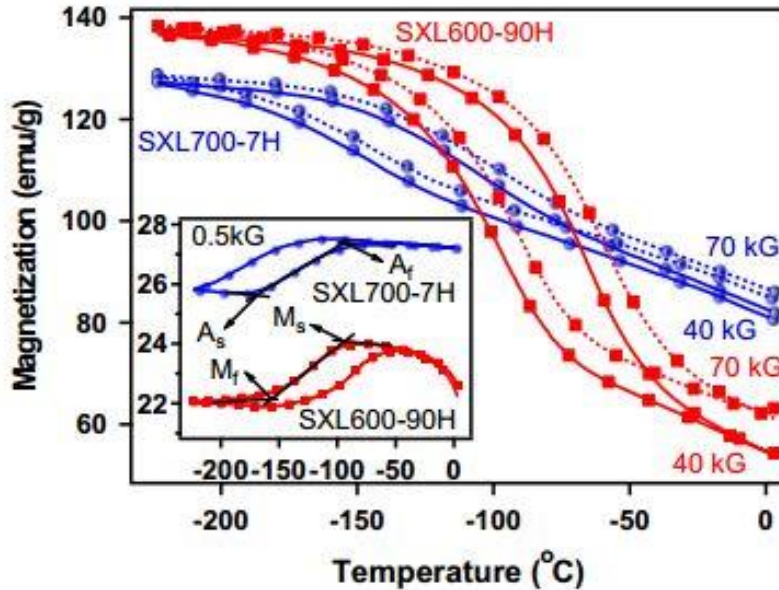
Figure 1.5 Magnetization response of FeNiCoAlTa single crystalline alloy [62].

Recently, Omori et al. studied the shape memory properties of FeNiCoAlNbB alloys and found that the alloy has high ductility, and it shows superelasticity with 5 % strain after texture formation [59]. Shape memory and superelastic behaviors are functions of a large number of factors that include microstructural features such as grain size, orientation and precipitation characteristics, as well as external influences such as applied stress and temperatures [60].

In this study, transformation temperatures, magnetization behavior, crystal structures, lattice parameters and microstructure of single and polycrystalline metamagnetic shape memory alloys were characterized, and systematic shape memory effect under constant stress and magnetic field, isothermal stress cycling under magnetic field and thermal cycling under magnetic field experiments were conducted in compression. A brief introduction of magnetic shape memory alloys is presented in Chapter

2. Experimental procedures and setup are explained in Chapter 3. Aging and cooling rate effects on the shape memory behavior and stress assisted magnetic field induced strain due to phase transformation are revealed in single crystalline of NiMnCoIn alloys in Chapter 4. Chapter 5 presents the effects of magnetic field and orientation on the superelasticity and shape memory behavior of NiMnCoIn single crystalline alloys. Shape memory properties of polycrystalline NiMnCoGa and MnNiSn MSMAs under magnetic field are revealed in Chapter 6. Chapter 7 presents the tension and compression responses of FeNiCoAlNb single crystalline alloys along the selected orientations and magnetization behavior of transforming phases. Lastly, conclusions are given in Chapter 8.

1.2   Objectives

The main objectives of this study are to:

- Explore the effects of cooling rate and heat treatments on the transformation temperatures, magnetization response, and shape memory behavior of NiMnCoIn single crystals under compressive stress.

- Determine the effects of high magnetic field (up to 9 Tesla) on the shape memory and superelastic responses of NiMnCoIn under compression

- Reveal the effects of Fe addition to MnNiSn alloys, and determine their conventional and magnetic shape memory properties as functions of stress and magnetic field.

- Investigate the effects of Co addition to polycrystalline NiMnGa alloys on their magnetic and shape memory properties under compression.

- Explore tension/compression responses of FeNiCoAlNb magnetic shape memory alloys, and reveal the effects of aging and orientation on their shape memory behavior.

2 Background

2.1 Active Materials

Active materials undergo a substantial change in one or more properties in response to a change in external conditions such as stress, temperature, or electrical and magnetic fields. Piezoelectrics, magnetostrictives, thermoelectrics, shape memory alloys and magnetic shape memory alloys are the main active materials groups that have been utilized for practical applications. These materials can transform one form of energy into another. In addition, they are capable of direct and inverse effects leading to applications as both actuators and sensors. An ideal active material would be the one that has high-frequency response, large strain and force outputs, high durability, and low cost.

Piezoelectric and magnetostrictive materials are the common actuation materials as a result of their high frequency response and large actuation stress; however, they have low deformation strain range (in micron level) [61]. Maximum actuation stress and strain of lead zirconate titane piezoceramics were observed around 100 MPa and 0.1 % [62], respectively, under several hundred V/cm electrical field [63]. In addition, magnetostrictive Terfanol-D produced around 60 MPa actuation stress and less than 0.2 % strain under low magnetic field around 0.3 T [64] .

The development of novel materials is very important for the advancement of materials engineering. The shape memory alloys are called active or multifunctional materials. Shape memory alloys have the ability to recover their deformed shape by heating or conduced electric field.

A high actuation frequency and energy density are very important properties of ideal active materials. The actuation energy densities of some common active materials are given

in Figure 2.1 [65]. The actuation energy density that is shown by the dotted lines in Figure 2.1 is the product of the actuation strain with the actuation stress with the assumption is that the active material is operating under constant stress. The specific actuation energy density can be calculated from Figure 2.1 by dividing the actuation energy density by the mass density. SMAs have high actuation energy density as shown in Figure 2.1.
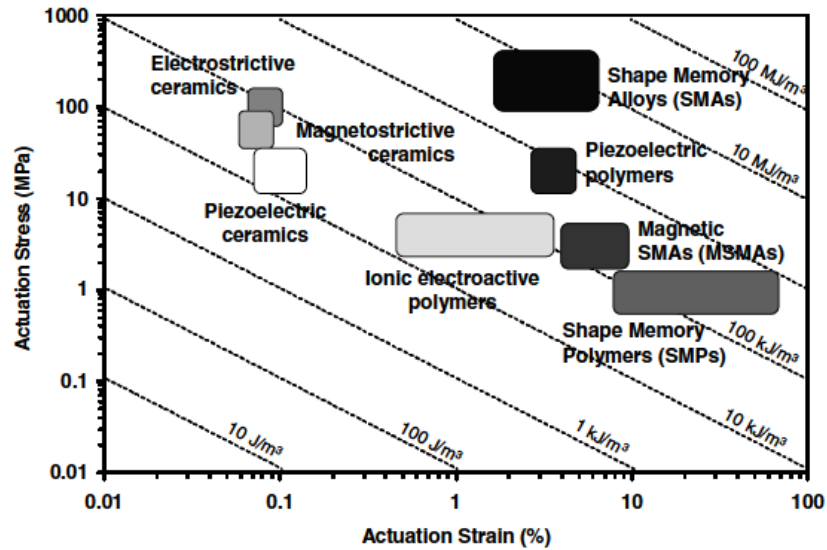
Figure 2.1 Actuation energy density diagram indicating typical ranges of actuation stress, actuation strain, and the actuation energy densities of different active materials [69].

Shape memory alloys can show high actuation stress around 400 MPa and large transformation strain (8 %), yet they have a low frequency response due to heat transfer [66]. In magnetic shape memory alloys, magnetic field induced strain can be 10 % which is higher than other magnetostrictive and piezoelectric materials. Magnetic shape memory alloys show higher frequencies when compared with conventional shape memory alloys, as shown in table 2.1.

Table 2.1 Comparison of the active materials

Actuation	Smart Materials		Strain (%)	Stress (MPa)	Frequency (Hz)
Heat	Shape memory alloys (NiTi)		2-8	400	1
Electric field	Ferroelectric		0.1	3	100,000
	Piezoelectric (PZT)		0.2	70	100,000
Magnetic field	Magneto-strictive (Terfenol-D)		0.2	80	10,000
	Ni_2MnGa	V.R.	5-10	5	1000
	NiMnIn	P.T.	0.5-4	20-100	-

2.1.1 Thermodynamics of martensitic transformations in SMAs

Unusual behavior of SMAs is caused by the reversible shape changes by *Martensitic Phase Transformations.* A martensitic transformation is an example of a displacive (diffusionless shear transformation) transition, in which there is cooperative motion of a relatively large number of atoms, each being displaced by only a small distance and they move in an organized manner relative to their neighbors. This homogeneous shearing of the parent phase creates a new crystal structure, without any compositional change (no diffusion). A simple thermodynamic analysis of the phase transformations is given here. The Gibbs free energy general form is given by;

$$\Delta G = \Delta H - T\Delta S \tag{2.1}$$

where ΔH is the enthalpy change, ΔS is the entropy change and T is temperature. For simplicity, the Gibbs free energies of martensite and austenite can be assumed to be decreasing linearly with temperature. At the intersection of their Gibbs free energy curves, the transforming phases have the same free energy and are in equilibrium at the equilibrium temperature (T_0). Below T_0, martensite has lower free energy and therefore it is favored

thermodynamically. Above T₀, austenite is stable. In figure 2.2, energy curves for austenite and martensite (forward) phase transformation are schematized. G_{ch}^A and G_{ch}^M are the chemical energies of austenite and martensite, respectively.
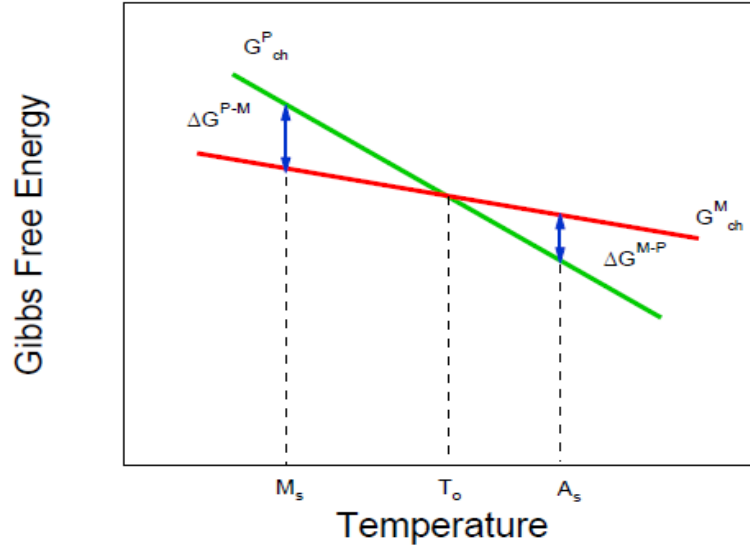
Figure 2.2 Schematics of the free-energy curves of martensite and austenite

$\Delta G_{ch}^{P \to M}$ is the chemical driving force for phase transformation from parent phase (austenite) to martensite and $\Delta G_{ch}^{M \to P}$ is vice versa. Parent phase starts transforming to martensite at M$_s$ (martensite start temperature) and martensite starts transforming to parent phase at A$_s$ (austenite start temperature) when there is a sufficient driving force in the system. When the G_{ch}^M and G_{ch}^A are equal to each other, no transformation is expected since there is no difference (driving force) between the chemical energies of transforming phases. The general thermodynamical equilibrium equiations for the forward transformation can be written of the forms [67];

$$\Delta G_{total}^{P \to M} = \Delta G_{ch}^{P \to M} - \Delta G_{mech}^{P \to M} + \Delta G_{nc}^{P \to M} = \Delta G_{el}^{P \to M} + \Delta G_{irr}^{P \to M} \qquad (2.2)$$

where $\Delta G_{total}^{P \to M}$ is the total Gibbs free energy difference to initiate the martensitic transformation, $\Delta G_{ch}^{P \to M}$ is the change in chemical energy, $\Delta G_{mech}^{P \to M}$ is the mechanical energy provided by the externally applied load upon the martensitic transformation, $\Delta G_{nc}^{P \to M}$ is the change in non-chemical energy. $\Delta G_{nc}^{P \to M}$ energy can be expressed as a combination of $\Delta G_{el}^{P \to M}$, the change in elastic energy and $\Delta G_{irr}^{P \to M}$, the irreversible energy during the phase transformation from austenite to martensite [68]. The $\Delta G_{total}^{P \to M}$ term should be smaller than zero in order to initiate the martensitic transformation. At T_0, since there is no driving force to trigger the martensitic transformation, an additional energy should be supplied (by cooling or heating) to initiate the transformation.

Additional cooling (T_0-M_s) below T_0 is necessary for parent phase to martensite transformation and additional heating (A_s-T_0) beyond T_0 is required for martensite to parent phase transformation assuming negligible elastic energy storage. Shape memory effect and pseudoelasticity/superelasticity originate from the thermoelastic martensitic transformation [69]. $\Delta G_{el}^{P \to M}$ is the stored elastic energy during the forward transformation and it is released completely upon back transformation from martensite to austenite. Therefore, the elastic energy storage is a reversible process [67]. The amount of the stored elastic energy should be equal to the released energy upon back transformation if there is no plastic relaxation due to dislocation generation/plastic deformation after a full transformation cycle [50, 70].

The irreversible energy, $\Delta G_{irr}^{P \to M}$, can be assumed as a combination of mainly frictional energy that is required to move phase front (between transforming phases), friction between martensite variants and internal twins in variants in addition to plastic

relaxation energy due to dislocation generation. Both of the abovementioned mechanisms result in dissipation of energy and consequently, hysteresis in SMAs [71].

2.1.2   Thermal Analysis of Shape Memory Alloys

Transformation Temperatures (TTs) are some of the most important shape memory properties. In SMAs, the martensite to austenite transformation (backward transformation) is an endothermic reaction (heat absorbing), while the austenite to martensite transformation (forward transformation) is an exothermic reaction (heat emitting) [72]. The Differential Scanning Calorimeter (DSC) is the most well-known equipment to determine the latent heat, enthalpy and transformation temperatures [73]. Figure 2.3 illustrates a typical DSC response. When the material is heated up, transformation begins at A_s and completes at A_f (austenite finish temperature). During cooling, austenite to martensite transformation starts at M_s and ends at M_f (martensite finish temperature). On the calorimetric graph, phase transformations are depicted as peaks and the areas under those peaks indicate the energies of transformations. Using these peaks, the critical transition temperatures can be determined. The most common method to measure the transformation temperatures is the intersection method. Tangents are drawn at the start and end of the transformation peaks and the base line of the heating and cooling curves. The inter sections of those tangent lines are accepted as the transformation temperatures. The enthalpy change of the phase transition can be found by integrating the area between to selected temperatures as shown in the Figure 2.3. Then, the transformation temperatures and enthalpies can be determined from the DSC profiles. Since the transformations occur without any external stress applied, they are also called zero-stress or stress-free transformation temperatures.
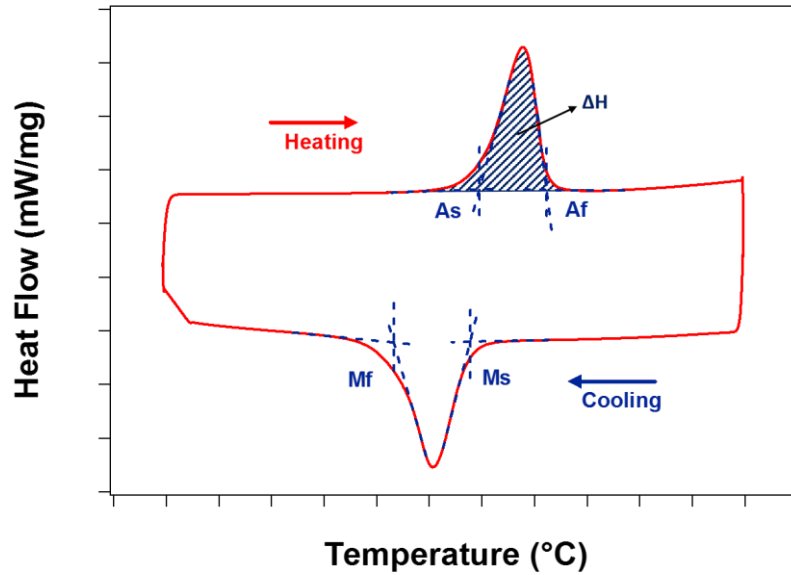
Figure 2.3 Schematic of DSC result and analyze method

2.1.3 Mechanical Characterization

Thermal analysis supplies useful information about transformation temperatures, but still they do not provide any information about the shape memory properties such as transformation strain and critical stress for transformation which are crucial parameters for actuator applications. Therefore, thermomechanical experiments are required to observe shape change in terms of strain during phase transformation.

2.1.3.1 Shape Memory Effect

A schematic of the shape memory effect during the thermal cycling under constant stress is shown in Figure 2.4. Stress is applied in the austenite phase and kept constant during the thermal cycling. Austenite transforms to martensite and stress favored martensite variants are formed during cooling, resulting in a shape change. Upon heating, the shape change is recovered by martensite to austenite transformation. From these experiments, transformation temperatures, recoverable strain and temperature hysteresis

can be determined as a function of stress. It should be noted that, in general, shape change cannot be observed if external stress is not applied due to the formation of self-accommodating (temperature-induced) martensite structure. Upon the application of stress, self-accommodating martensite variants can be disrupted and favored martensite variants can be formed, resulting in a shape change. The volume fraction of favored martensite variants and the transformation strain increase with stress. Figure 2.4 also covers the graphical method to determine transformation strain, temperatures and hysteresis. If there is no plastic deformation, the recoverable strain is equal to the transformation and total strain. However, further increase in applied stress could result in plastic deformation where the total strain will be the sum of recoverable and irrecoverable strains. It should also be noted that irrecoverable strain could stem from the plastic deformation and/or remnant martensite.
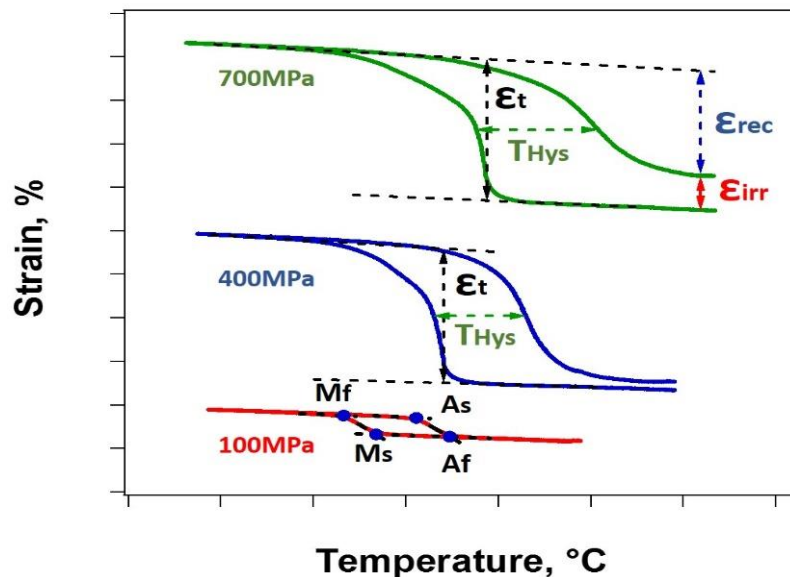
Figure 2.4 Shape memory effect of $Ni_{50.4}Ti_{29.9}Hf_{19.3}Zr_{0.4}$ SMA as a function of applied stress

The transformation temperatures can be determined by the intersection method similar to the one applied to DSC tests. Total strain can be obtained from the difference between the strains of austenite and martensite at a selected temperature, as shown in figure 2.4. Since austenite and martensite have different thermal expansion coefficients, total strain can be temperature dependent. Thus, in general total strain is calculated at M_s, A_f or at the mid-temperature of the thermal hysteresis.

Irrecoverable strain can be calculated at a temperature above A_f and recoverable strain can be calculated either at the same temperature or by subtracting irrecoverable strain from total strain. There are several methods to determine temperature hysteresis; i) the temperature difference during cooling and heating at the midpoint of the total strain, ii) $(A_f-M_s)/2$ and iii) $(A_f-M_f)/2$.

Thermal hysteresis is related to the energy dissipation during the phase transformation. Friction between the austenite and martensite interphases, dissipation during detwinning, incompatibility of transforming phases and slip are the main factors of energy dissipation. In the absence of plastic deformation, hysteresis could either increase or decrease with stress, depending on the compatibility of the transforming phases.

2.1.3.2 Superelasticity

The sample is loaded above A_f where elastic deformation of austenite is initially observed. When the load reaches a critical value, stress induced austenite to martensite transformation occurs where in most cases a plateau is observed at this stage. Further loading results in elastic deformation of martensite and detwinning of martensite. If it is unloaded at this region, shape recovery starts with elastic deformation recovery of the martensite, followed by the martensite to austenite transformation and elastic deformation

recovery of austenite. If there is no plastic deformation, the fully reversible shape recovery will be obtained. Further loading after phase transformation could result in exceeding the critical stress for slip deformation where another plateau-like behavior can be observed. Upon unloading after this stage, specimen will not show full recovery due to plastic deformation. This plastic strain is due to the generation and propagation of dislocations and results in martensite stabilization. Figure 2.5 shows the typical superelasticity behavior of shape memory alloys. Young moduli of austenite(E_A) and martensite(E_M), critical stresses of forward($\sigma_{cr,ft}$) and back ($\sigma_{cr,bt}$) transformation$s$, critical stress for plastic deformation($\sigma_{cr,pd}$), mechanical hysteresis (Δ_{σ}), elastic strain (ε_{el}), superelastic strain (ε_{SE}) and irrecoverable strain (ε_{irr}) can be determined from the superelasticity curves.
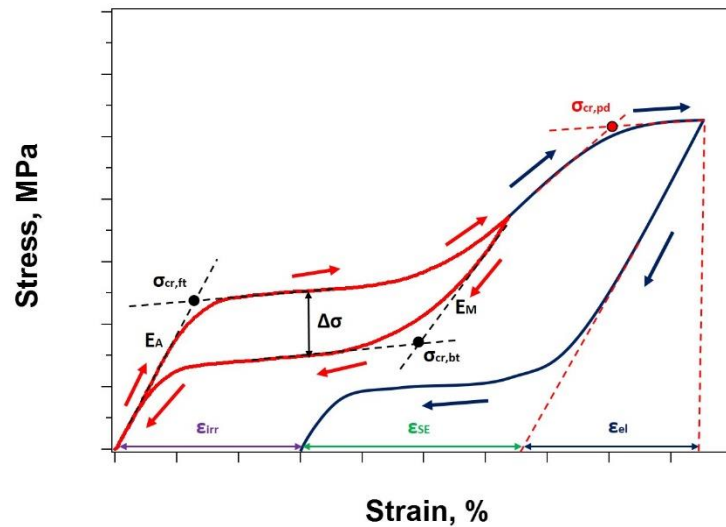
Figure 2.5 A schematic of the superelasticity behavior of shape memory alloys

Critical stresses for martensite reorientation, martensitic transformation and slip are strongly testing temperature dependent. If the material is in martensite and deformed below A_s, critical stress for the martensite reorientation decreases with temperature due to increased mobility of internal twins and martensite plates boundaries. If the material is in austenite and deformed between M_s and A_f ($M_s<T<A_f$), stress induced martensite is formed during loading where critical stress for martensitic transformation increases with temperature and shape recovery cannot be observed upon unloading, as shown in figure 2.6b. Shape recovery occurs when the temperature is increased above A_f temperature. Superelasticity is observed when the sample deformed between A_f and M_d ($A_f<T<M_d$). Stress induced martensite cannot be observed above M_d (martensite desist temperature) and alloys deform like conventional materials [74]. M_d can be considered as the intersection of critical stresses of martensitic transformation and slip, as shown in figure 2.6b. If the material is not strong enough or temperature is close to M_d, partial recovery can be observed since martensitic transformation and plastic deformation occur simultaneously. If the sample is deformed above M_d, plastic deformation takes place before martensitic transformation where shape recovery cannot be observed during unloading. Thus, superelasticity can only be observed between A_f and M_d where the difference between these temperatures is called superelastic window (see figure 2.6b).
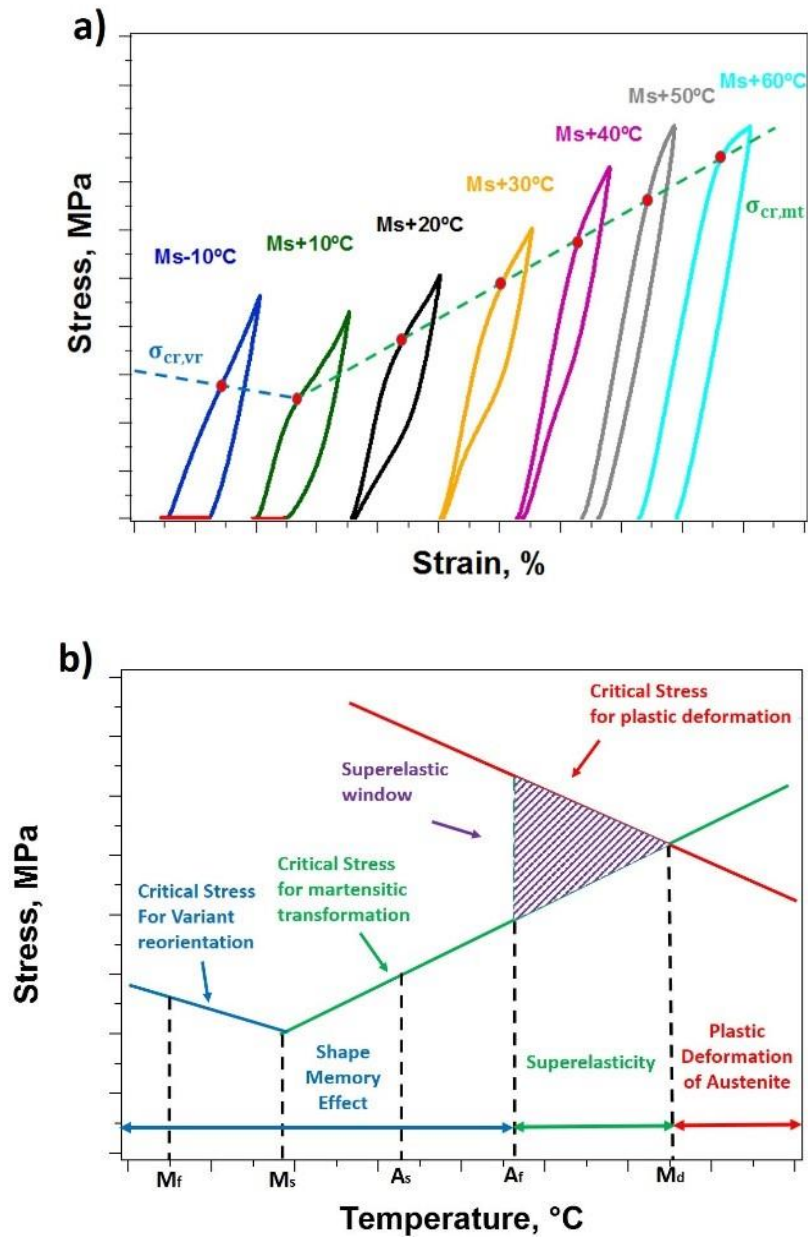
Figure 2.6 a) Schematic of stress-strain curves, b) critical stress of SMAs as a

function of temperature

2.2   Magnetic Shape Memory Alloys

Magnetic Shape Memory Alloys have the ability to change their shape when a magnetic field is applied, and then have the ability to return to their former state when the stimulus is removed. Magnetic shape memory alloys can work in high frequencies which offers actuation, sensing and power generation capabilities at higher frequency levels than conventional shape memory alloys [75-78], as shown in figure 2.7. Not only MSMAs show higher frequency responses, but they also have comparable actuation strain to conventional shape memory alloys. High actuation stress and strain, operating temperature and range, frequency range and low magnetic field requirement and cost are the ideal expectations from magnetic shape memory alloys for actuation and sensing applications. In order to achieve these ideal properties, magneto-thermo-mechanical characterization of magnetic shape memory alloys is required.
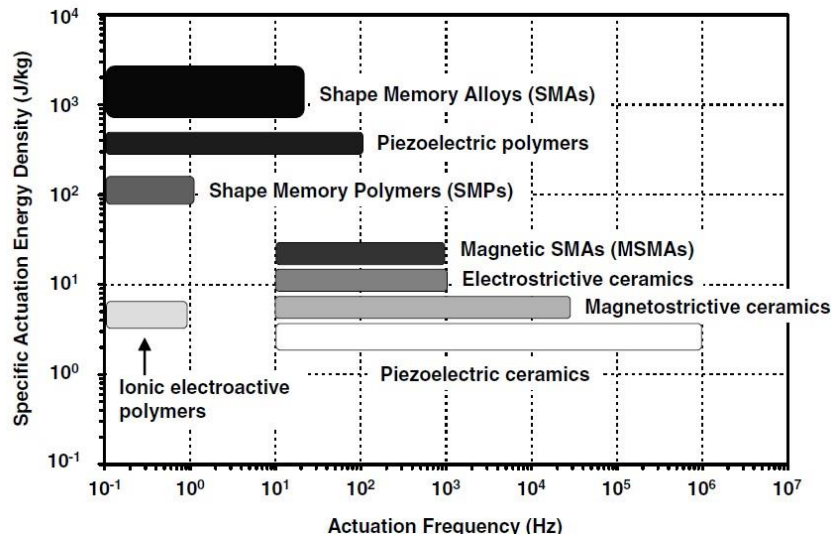
Figure 2.7 Actuation energy density diagram [69]

2.2.1 Thermodynamics of martensitic transformations in MSMAs

The Gibbs free energy difference between the austenite and martensite phases during a thermoelastic martensitic transformation under magnetic field can be written as [8];

$$\Delta G_{total}^{P \to M}(T, \sigma, H) = \Delta G_{ch}^{P \to M} - \Delta G_{mech}^{P \to M} + \Delta G_{el}^{P \to M} + \Delta G_{irr}^{P \to M} - \Delta G_{mag}^{P \to M} + \Delta G_{MAE}^{P \to M} \quad (2.3)$$

where $\Delta G_{mag}^{P \to M}$ is the Zeeman energy difference (ZE) and $\Delta G_{MAE}^{P \to M}$ is the magnetocrystalline anisotropy energy between martensite and austenite phase.

Required mechanical energy for the stress-induced martensitic transformation and superelasticity with and without a magnetic field at a temperature above the equilibrium temperature can be expressed as;

$$\Delta G_{mech}^{P \to M}(T,H) - \Delta G_{mech}^{P \to M}(T,0) = -\Delta G_{mag}^{P \to M} + \Delta G_{MAE}^{P \to M} \quad (2.4)$$

The mechanical energy can be written in terms of the stress level and transformation strain in case of no hardening;

$$\sigma_{mag} = \sigma_{c,forward}^{H} - \sigma_{c,forward} = \frac{-\Delta G_{mag}^{P \to M} + \Delta G_{MAE}^{P \to M}}{\varepsilon_0} \quad (2.5)$$

where ε_0 is the maximum transformation strain. In the NiMnCoIn alloys, the $\Delta G_{MAE}^{P \to M}$ term is negligible since martensite phase is weakly magnetic, and the MAE of austenite is very low.

It should be noted that magnetostress depends on the magnetization difference between transforming phases and transformation strain. In order to determine large magnetostress, a large magnetization difference between martensite and austenite is desired.

2.2.2 Magnetic Measurements

Magnetic measurement is one of the alternative methods to determine the shape memory properties including transformation temperatures and temperature hysteresis. Magnetization of the material can be measured as a function of temperature under an external magnetic field. This method is very effective for revealing the transformation behavior of magnetic shape memory alloys where transforming phases have different magnetization behavior. Transformation temperatures can be measured by the tangent method as described for DSC measurements.

Figure 2.8 shows the transformation behavior of $Ni_{45}Mn_{36.5}Co_5In_{13.5}$ single crystalline alloy where the change of its magnetization response with temperature is recorded under a constant applied magnetic field [12]. In general, austenite phase is ferromagnetic and martensite phase is weakly magnetic in NiMnCoIn magnetic shape memory alloys. Thus, during cooling, magnetization drops due to forward transformation from highly magnetic austenite to weakly magnetic martensite, and back transformation occurs with increasing magnetization level during heating. Temperature cycling under magnetic field provides the transformation temperatures and hysteresis as a function of applied magnetic field.
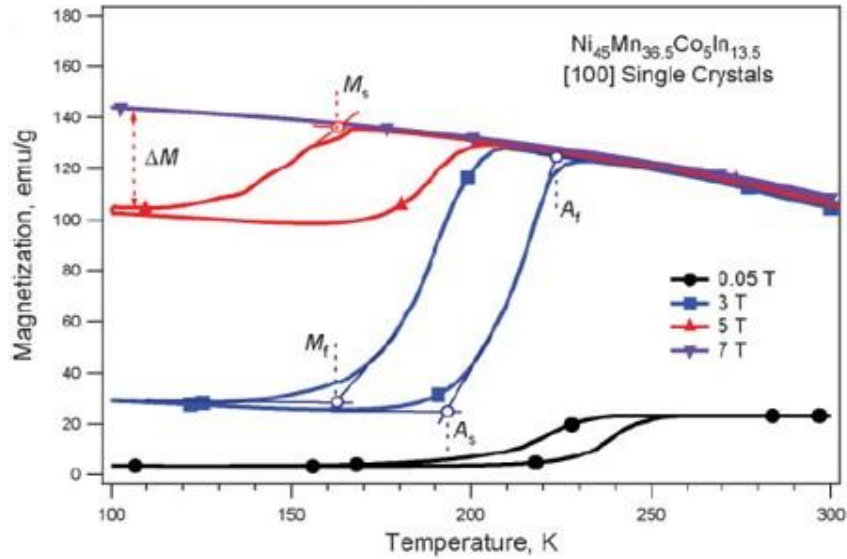
Figure 2.8 Magnetization of NiMnCoIn single crystalline alloys as a function of

temperature under selected magnetic fields [83]

2.2.3 Properties of Magnetic Shape Memory Alloys

2.2.3.2 Magnetic Field-Induced Variant Reorientation

External shape change by magnetic field is frequently based on rearrangement of martensite variants by detwinning [5, 6, 8, 79]. NiMnGa alloys are the most widely explored MSMAs [5, 8, 78, 79] among others such as FePt [80] , FePd [5, 81], CoNiAl [36, 82, 83], CoNiGa [84], CoNi [85], NiFeGa [37, 86], and NiFeGaCo [87] due to their low stress requirements for detwinning and high magnetocrystalline anisotropy energy. Magnetocrystalline anisotropy energy is the main source of variant reorientation. MAE is the area between the magnetization response of ferromagnetic single martensite variants along the easy and hard axes, as shown figure 2.9. MAE is orientation dependent and limited. MAE does not increase after a certain limit with applied field [7-11, 88].
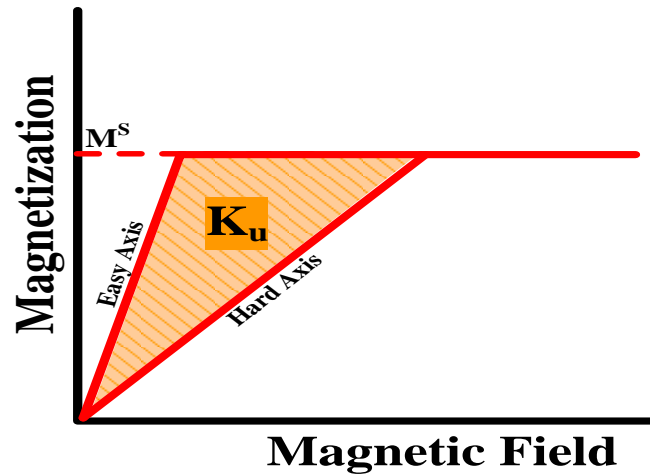
Figure 2.9 Magnetocrystalline anisotropy energy, Ku [21].

When there is no external magnetic field, magnetic domains have a tendency to orient along the easy axis of magnetization. If a magnetic field is applied along a direction other than the easy axis, the magnetization direction of the domains will rotate from their easy axis towards the applied field direction as, shown in figure 2.10. The energy required for the magnetization rotation from the easy axis to the applied field direction is given by the magnetocrystalline anisotropy energy. If the MAE is higher than the energy needed for detwinning, variant reorientation can occur.
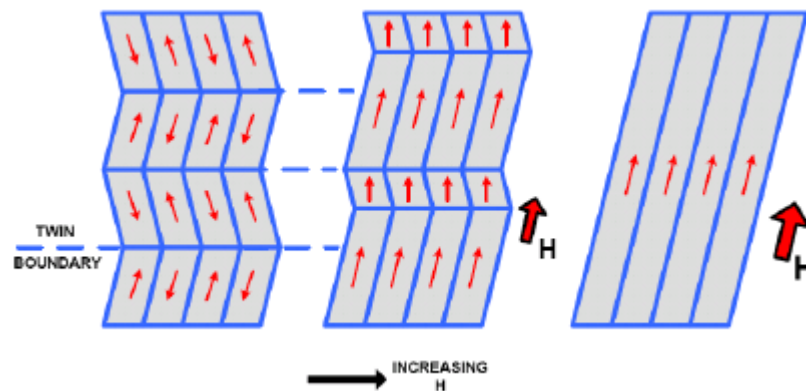
Figure 2.10 Magnetic field induced variant reorientation mechanism [11].

There are two main parameters other than the magnetic field induced strain (MFIS) level that are used to quantify the performance of MSMAs. The first one is the blocking stress or maximum actuation stress. Magnetostress, the second parameter, is defined as the increase in stress required for detwinning under a constant magnetic field. One of the main issues in development of MSMAs is low blocking and magnetostress levels (<2 MPa) observed [77, 89] which impedes the utilization of these alloys in practical applications where high actuation forces are required.

2.2.3.3 Magnetic Field-Induced Phase Transformation

In addition to variant reorientation, magnetic field induced strain can also be observed by phase transformation in which magnetic state of the transforming phases are required to be different. In MSMAs, drastic change in magnetization can be observed during the phase transformation from ferromagnetic austenite to antiferro/paramagnetic martensite or vice versa. These alloys which have different magnetic states of phases are called metamagnetic shape memory alloys, and magnetic field induced strain can be observed by phase transformation. The main source of phase transformation is Zeeman energy, as shown in figure 2.11. $Ni_2Mn_{1+x}Y_{1-x}$ (Y=In, Sn and Sb) metamagnetic shape memory alloys have received considerable attention due to their giant magnetoresistance [90-93], shape recovery [94], or large inverse magnetocaloric effect [20, 95-105]. In contrast, some magnetic shape memory alloys (e.g NiMnGa) have either ferromagnetic or partially paramagnetic martensite and austenite phases, so external shape change can only occur by variant reorientation. Actuation stress of magnetic field induced phase transformation could be one order of magnitude higher than variant reorientation in the NiMnGa magnetic shape memory alloys.
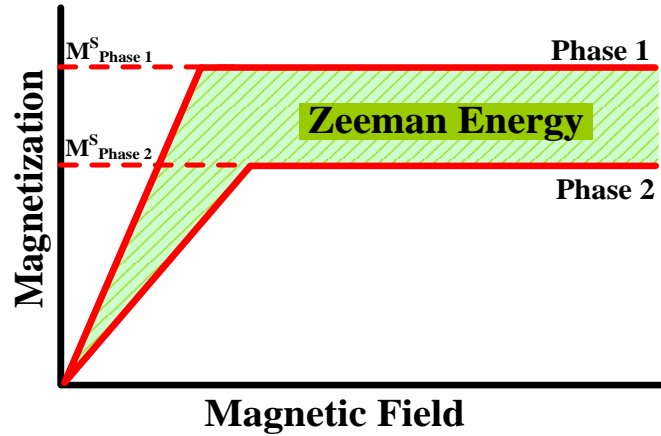
Figure 2.11 Zeeman Energy [21].

Zeeman Energy (ZE) is calculated as $E_{ZE} = \mu_0 \times \Delta M \times H$, where μ_0 is magnetic constant, ΔM is magnetization difference of transforming phases and H is the applied magnetic field.

The main requirement for the field-induced phase transformation is that the magnetic driving energy must be sufficient to move the phase front, as shown 2.12. The irreversible field-induced martensitic phase transformation has been detected in several ferromagnetic materials, especially in iron based alloys such as Fe-C and Fe-Ni, under very high field magnitudes (>15 Tesla) without any report of observed MFIS levels.
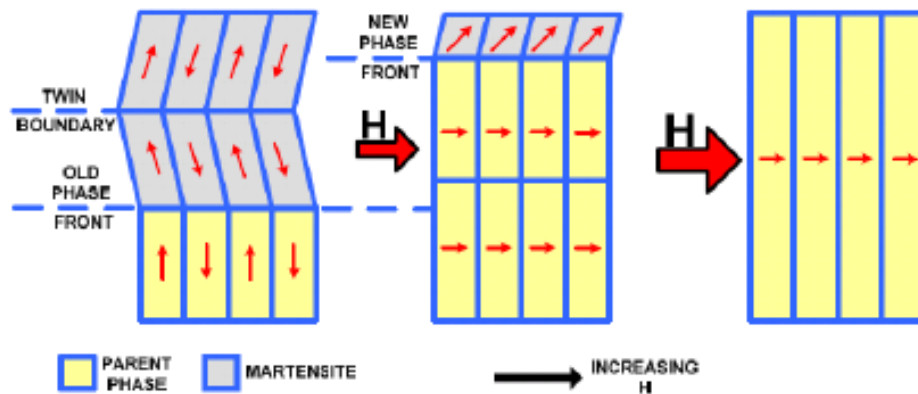
Figure 2.12 Magnetic field induced phase transformation mechanism [11].

3 Experimental Procedures

3.1 Sample Preparation

$Ni_{45}Mn_{36.5}Co_5In_{13.5}$ (at. %) alloy was fabricated by using induction melting under vacuum. Bridgman technique with He atmosphere was used to grow single crystals. Compression specimens (4x4x8 mm^3) were cut with the long axis along the [001] orientation of the austenite phase. The NiMnCoIn specimens were homogenized at 900 °C for 24 hours, and followed by different cooling rates such as furnace cooling, air cooling, and water quenching. After homogenization, the specimens were subjected to additional heat treatment in which the aging temperature varied from 300 °C to 800 °C incremented by 50 °C for 3 hours, followed by water quenching.

Polycrystalline specimens with chemical compositions $Ni_{50-x}Co_xMn_{32}Ga_{18}$ (at%) x=0,4,6,7,8 were prepared by the conventional arc melting method in an argon atmosphere using high purity elements of Ni (99.9%); Mn (99.99%); Co (99.9%) and Ga (99.999%). Then, the arc melted buttons were annealed at 850 °C for 72 hours under vacuum and slowly cooled down to room temperature in the furnace.

Polycrystalline $Mn_{49}Ni_{42}Sn_9$ and $Mn_{49}Ni_{39}Sn_9Fe_3$ (at%) were prepared by conventional arc induction melting method in argon atmosphere. MnNiSn and MnNiSnFe alloys were homogenized at 900 °C for 72 hours. An additional heat treatment of 900 °C for 30 min was also conducted in MnNiSnFe alloys. The samples were quenched in water after their selected heat treatments.

The single crystal samples were grown by the Bridgman technique in a He atmosphere by using a material with nominal composition of $Fe_{41}Ni_{28}Co_{17}Al_{11.5}Nb_{2.5}$ (at.%). Compression specimens (4x4x8 mm^3) were cut with their long axes along the [001]

orientation of the austenite phase. The single crystals were solutionized at 1200 ℃ for 5 hours in a vacuum, and quenched in water. Then, they were heat treated at their selected conditions. A Lindberg/Blue M BF5114841 box furnace was used for heat treatments, as shown in figure 3.1.

Figure 3.1 Lindberg/Blue M BF5114841 box furnace.

Compression specimens were cut by Electro Discharge Machine (EDM) (Figure 3.2.).

Figure 3.2 Electro Discharge Machine.

3.2 DSC and TEM

Transformation temperatures were determined by a Perkin Elmer PYRIS 1 DSC, as shown in figure 3.3. The microstructure, after aging, was investigated by transmission electron microscopy (TEM). The thin foil specimens for TEM were prepared with a twinjet electropolishing device in a solution consisting of (all vol. %) 8 % perchloric acid, 72 % acetic acid, 12 % methanol and 8 % ethylene glycol at room temperature. The TEM observations were carried out by JEOL JEM-2100HR (and HC) operated at acceleration voltage of 200 kV.

Figure 3.3 Perkin-Elmer Pyris 1 Differential Scanning Calorimetry.

3.3 Magnetic Measurements

Quantum Design (QD) 14 T Physical Properties Measurement System (PPMS) was used for magnetization experiment to determine martensitic phase transformation during heating and cooling under applied magnetic field, as shown in figure 3.4.

Figure 3.4 Quantum Design (QD) 14 T Physical Properties Measurement System

(PPMS)

3.4 Hardness Testing

Vickers hardness values were determined by using Sun-Tec model FM-7 micro-hardness test equipment (Figure 3.5). Before the hardness test, samples are placed in epoxy and polished. Hardness tests were performed with a 100 gf force and 15 seconds dwell time. The hardness test was conducted ten times for each sample, where the lowest and the highest values were omitted and the average of the remaining eight values were taken as the final hardness result for the sample.

Figure 3.5 Sun-tec model FM-7 micro-hardness test equipment.

3.5 Mechanical Testing

100 kN MTS servohydraulic test frame was used for compression tests with the strain rate of 10^{-4}, as shown in figure 3.6. An Omega CN8200 series temperature controller was used to govern a heating rate of 10 °C/min and a cooling rate of 5 °C/min. The temperature of the sample was monitored using K-type thermocouples attached to the sample and grips.

Figure 3.6 MTS Landmark servo-hydraulic machine.

Magnetic field was applied by Cryogenic Limited 9 Tesla PID controlled cryogen free superconducting magnet which is attached to MTS servohydraulic test frame, as shown in figure 3.7. Transformation strain was measured by a capacitec sensor. The temperature of the sample was monitored using T-type thermocouples.
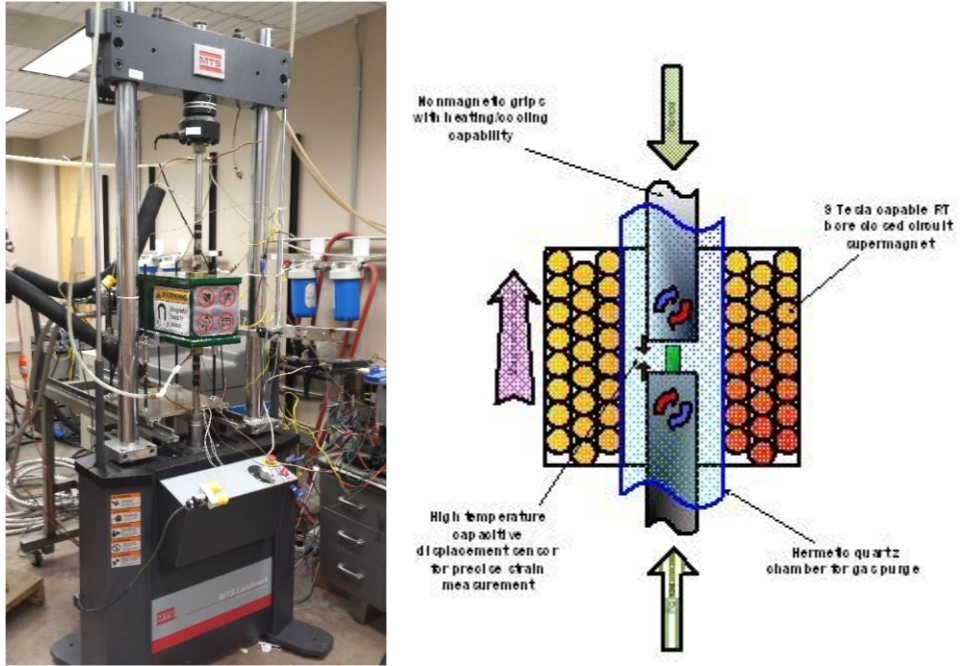
Figure 3.7 Schematic of MTS setup with superconducting magnet

3.6   XRD Analysis

X-ray diffraction (XRD) measurements, that revealed the lattice parameters, were carried out on a Bruker AXS D8 Discover diffractometer using Cu Kα radiation (Figure3.8). The highly polished specimens were scanned at room temperature to capture the crystalline structure of the samples.

Figure 3.8 Bruker AXS D8 Discover diffractometer.

4   Effects of Heat Treatment and Cooling Rate on the Shape Memory Behavior of [001]-Oriented NiMnCoIn Metamagnetic Shape Memory Alloys

4.1   Introduction

In this chapter, the effects of heat treatment temperature and cooling rate on shape memory behavior, namely transformation temperatures, magnetic and mechanical properties in NiMnCoIn [001] oriented single crystalline metamagnetic shape memory alloys were investigated. Transformation temperatures after selected heat treatment conditions, crystal structures and lattice parameters of transforming phases, magnetization behavior of martensite and austenite and mechanical behavior of NiMnCoIn MSMAs under compression will be revealed.

In order to determine magnetic field induced reversible strain, low hysteresis is desired in order to separate superelastic loops and thermal cycling curves with/without the presence of a magnetic field. The purpose of the study is to identify appropriate heat treatments to obtain low hysteresis for magnetic experiments in NiMnCoIn single crystalline alloys. Moreover, the effects of magnetic field on superelasticity, shape memory effect, and stress assisted magnetic field induced reversible phase transformation will be revealed.

4.2   DSC Results

Figure 4.1 shows the DSC curves for $Ni_{45}Mn_{36.5}Co_5In_{13.5}$ [100] oriented single crystalline shape memory alloys to determine the influence of the cooling rate on transformation temperatures. The specimens were homogenized at 900 °C for 24 hours and then cooled at different rates be means of furnace cooling, air cooling, and water

quenching. Water quenched specimen exhibited clear and sharp transformation peaks compared to air cooled specimen. The water quenched specimen started transforming from austenite to martensite at 4 °C upon cooling. The martensite start temperature drastically decreased from around 41 °C to -37 °C in the air cooled specimen. The change in transformation temperatures can be explained by the change in the degree of interatomic ordering. Since the specimen homogenized at 900 °C, quenching at that high temperature resulted in keeping the B2 disordered atomic structure. Higher degree of ordering (L2$_1$) was obtained by slow cooling in the air cooled sample. Thus, transformation temperatures decreased with increased cooling time [24-26]. The transformation peaks were not observed in the furnace cooled specimen. It is clear that by controlling the cooling rate, transformation temperatures can be tailored for a wide temperature range for envisioned applications.
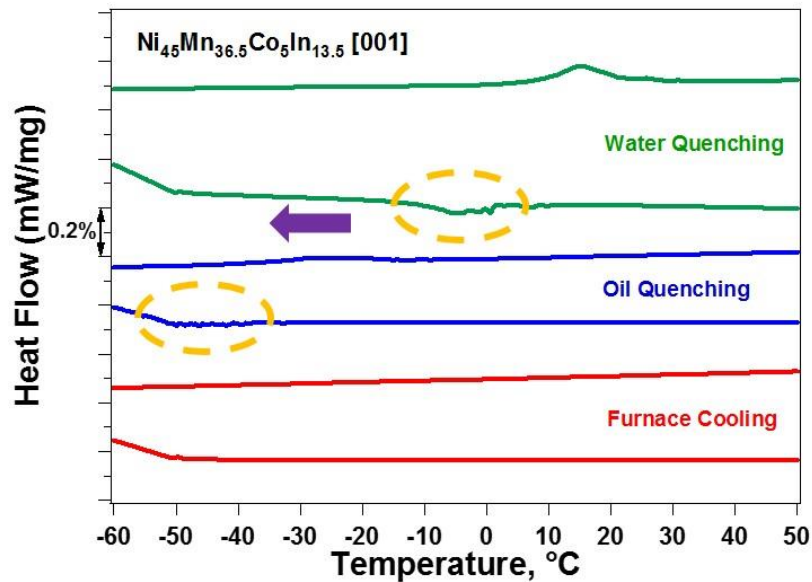
Figure 4.1 DSC curves to observe cooling rate effect on transformation

temperatures

In order to determine whether heat treatment or cooling rate is more effective to alter transformation temperatures, two different DSC experiments were conducted by changing the heat treatment sequences. Firstly, the specimens were homogenized for 24 hours at 900 °C and then water quenched. After the homogenization, they were heat treated for 3 hours at 600 °C followed by water quenching, air cooling, or furnace cooling. The DSC results are shown in Figure 4.2a. It is clear that transformation temperatures decreased with increased cooling time. For instance, M_s of water quenched sample was 31 °C and decreased to − 62 °C in air cooled sample. Transformation peaks were not observed in furnace cooled sample. In the second procedure, homogenized samples (24 hours at 900 °C) were cooled down by water quenching, oil quenching, and furnace cooling. Then, they were heat treated for 3 hours at 600 °C followed by water quenching. Since all specimens were quenched in water after the heat treatment, transformation temperatures of each specimen were close to each other (Figure 4.2b). For instance, M_s was determined as 31 °C, 24 °C, and 29 °C for initially water quenched, air cooled and furnace cooled specimens, respectively. As a result, post heat treatment and cooling rate dominated the interatomic ordering which influenced transformation temperatures.
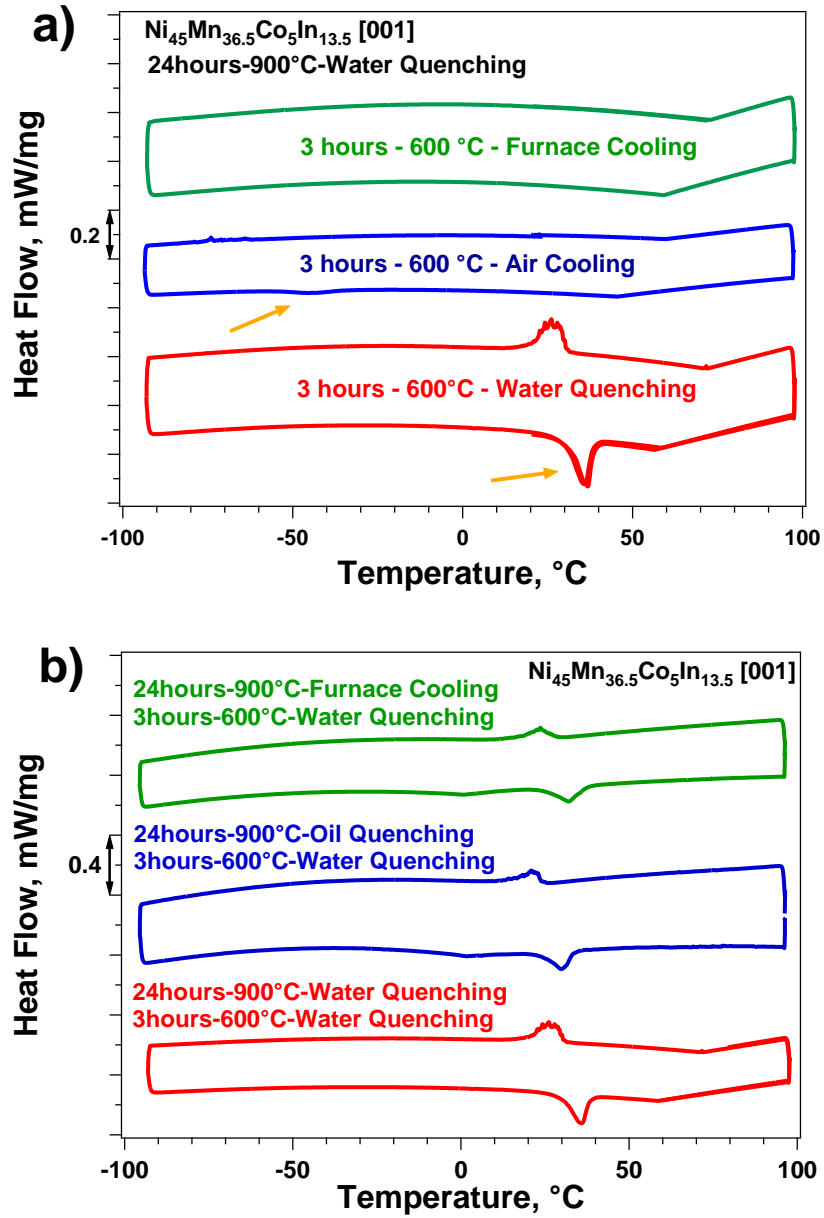
Figure 4.2 a) DSC response of specimens which were initially homogenized at 900 °C for 24 hours and quenched in water and additionally heat treated at 600 °C for 3 hours followed by water quenching, air cooling, or furnace cooling. b) DSC responses of samples which were initially homogenized at 900 °C for 24 hours followed by water quenching, oil quenching, and furnace cooling and additionally heat treated at 600 °C for 3 hours followed by water quenching.

In order to determine the effects of heat treatment temperature on transformation temperatures, the specimens (homogenized at 900 °C for 24 hours and quenched in water) were heat treated from 300 °C to 800 °C for 3 hours and water quenched. DSC curves of heat treated samples were shown in Figure 4.3a. The transformation peaks were not observed for samples heat treated below 500 °C and above 750 °C. M_s and A_f of heat treated specimen at 500 °C was -10 °C and 7 °C, respectively. In 700 °C heat treated specimen, M_s and A_f were 44 °C and 51 °C, respectively. Transformation temperatures were initially increased with heat treatment temperature and then saturated above 700 °C, as shown Figure 4.3b. Effects of disordering on the transformation temperatures were reported in the literature as transformation temperatures increase with increasing the disordering in NiMn-based magnetic shape memory alloys [24-26, 106]. The degree of ordering decreased with increasing heat treatment temperature by transforming ordered $L2_1$ to disordered B2 structure. Moreover, temperature hysteresis was decreased from 20 °C in 500 °C heat treated specimen to 9 °C in 700 °C heat treated specimen (Figure 4.3c).
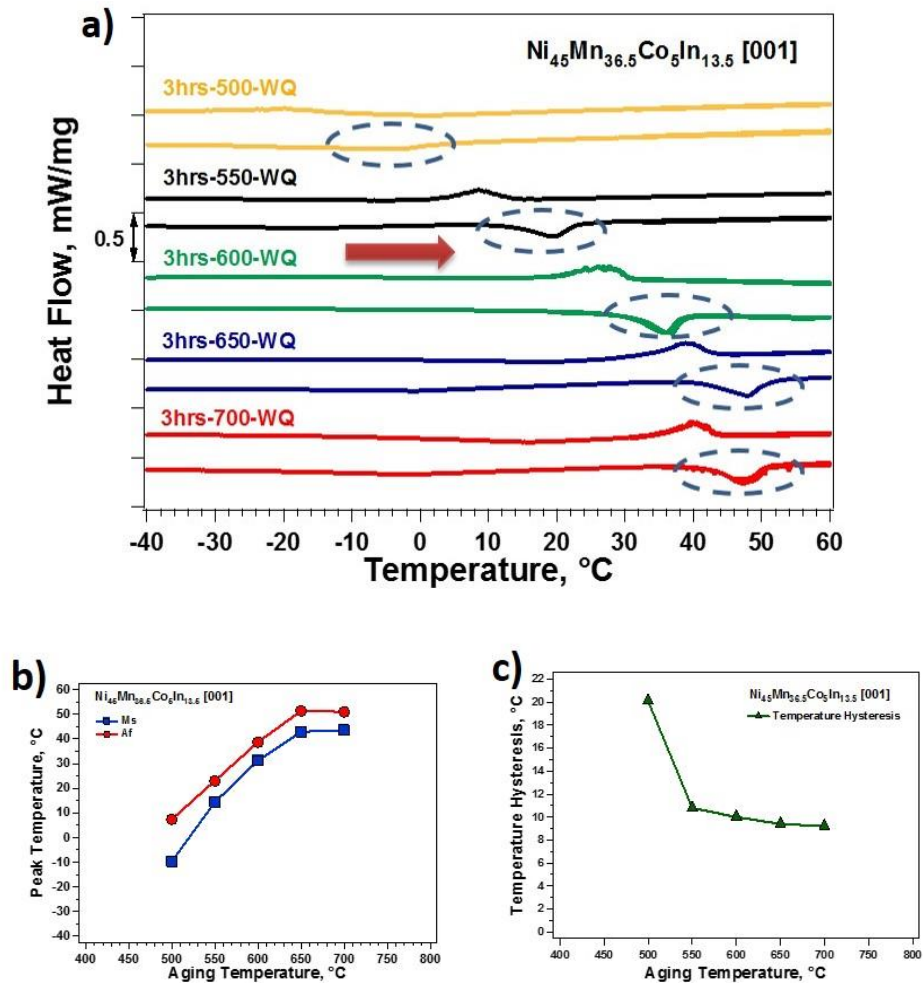
Figure 4.3 a) DSC responses of additionally heat treated NiMnCoIn alloys b) Change of transformation temperatures with heat treatment temperature c) Change of temperature hysteresis with heat treatment temperature

4.3   XRD Results

X-ray diffraction measurements were carried out to determine the crystal structures of austenite and martensite phases of the $Ni_{45}Mn_{36.5}Co_5In_{13.5}$ alloy. Figure 4.4 shows the XRD patterns obtained at room temperature and 200 °C for the [100]-oriented $Ni_{45}Mn_{36.5}Co_5In_{13.5}$ single crystal. At 200 °C, there are (200) and (400) reflections of $L2_1$ austenite at around 30° and 62°, respectively. The lattice parameter of the cubic $L2_1$

austenite is a = 0.5975 nm. The Ni$_{45}$Mn$_{36.5}$Co$_5$In$_{13.5}$ alloy consists of a single martensite

phase at room temperature, which is consistent with the DSC result shown in Figure 4.1.

The crystal structure of the martensite phase can be determined as monoclinic 14M with

lattice parameters of a = 0.4346 nm, b = 0.5571 nm, c = 3.0697 nm and β = 93.5°.
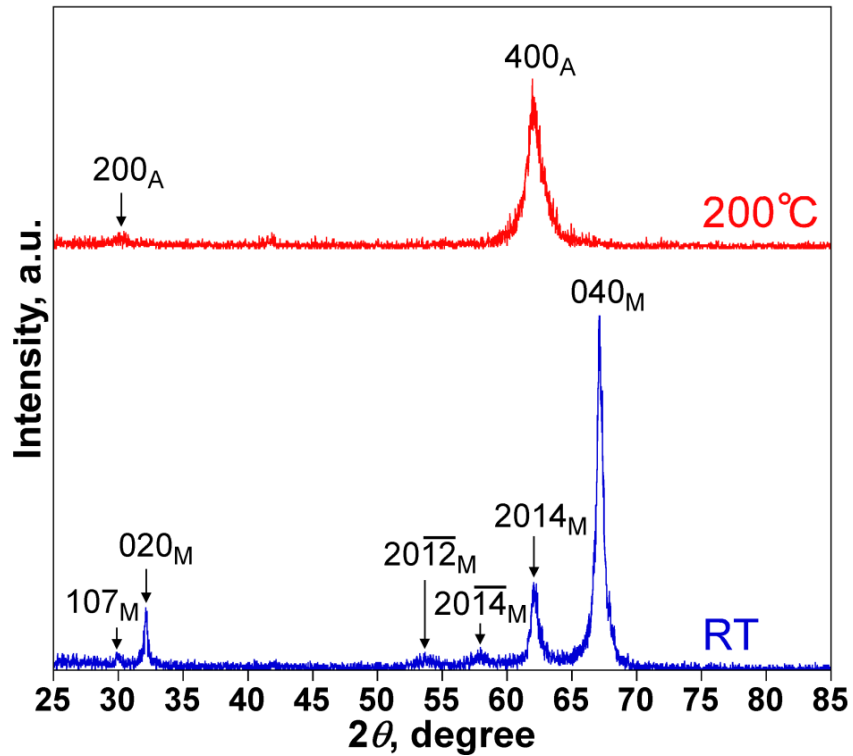
Figure 4.4 XRD patterns of the [100]-oriented Ni$_{45}$Mn$_{36.5}$Co$_5$In$_{13.5}$ single crystal obtained

at room temperature (RT) and 200 °C. Subscripts A and M represent L2$_1$ austenite and

14M martensite, respectively.

4.4   TEM Results

Figures 4.5a and 4.5b are the bright field transmission electron microscope image of the $Ni_{45}Mn_{36.5}Co_5In_{13.5}$ single crystal showing 14M martensite plates and the selected area diffraction (SAD) pattern taken from the martensite plate A in Figure 4.5a, respectively. There are fine striations in the 14M martensite plates on the $(001)_{14M}$ planes. The striations are considered to be stacking faults on the $(001)_{14M}$ basal planes since Figure 4.5b shows only reflections from a single 14M martensite variant. Figure 4.5c shows the SAD pattern obtained at the interface between the martensite plates A and B in Figure 4.5a. The martensite plates A and B are twin-related with respect to the $(107)_{14M}$ compound twinning plane. The twinning elements of the $(107)_{14M}$ compound twin calculated by the Bilby-Crocker theory [107] are $K_1 = (107)_{14M}$, $K_2 = (\bar{1}07)_{14M}$, $\eta_1 = [\bar{7}01]_{14M}$, $\eta_2 = [701]_{14M}$ and $s = 0.01803$.
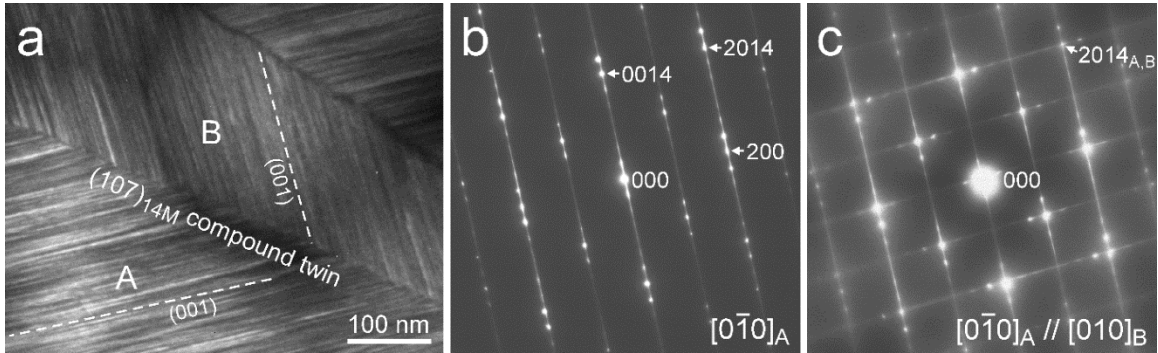
Figure 4.5 a) Bright field TEM micrograph of the $Ni_{45}Mn_{36.5}Co_5In_{13.5}$ single crystal at room temperature. b) SAD pattern taken from the martensite plate A in (a). c) SAD pattern obtained at the interface between the martensite plates A and B in (a).

4.5   Magnetic Measurements

Magnetization measurements were conducted to reveal magnetization behavior of parent and martensite phases as shown in Figure 4.6 Heat treated specimen at 700 °C for 3 hours, followed by water quenching was heated up to a temperature above A_f and then cooled down to a temperature below M_f under 0.05 T. After the thermal cycle was completed, the applied magnetic field was increased to next level and thermal cycling was repeated under 1 T and 7 T. Martensitic transformation occurred from weakly magnetic martensite to ferromagnetic austenite during heating under 0.05 T, and vice versa. Magnetic field favors austenite formation due to its ferromagnetic behavior Thus, transformation temperatures decrease with an increase in magnetic field. M_s was 37 °C under 0.05 T and decreased to 17 °C under 7 T. Magnetization difference between austenite and martensite phases increased with increasing applied magnetic field level. Kinetic arrest phenomena was not observed even under high magnetic field (7 T) because of high transformation temperatures.
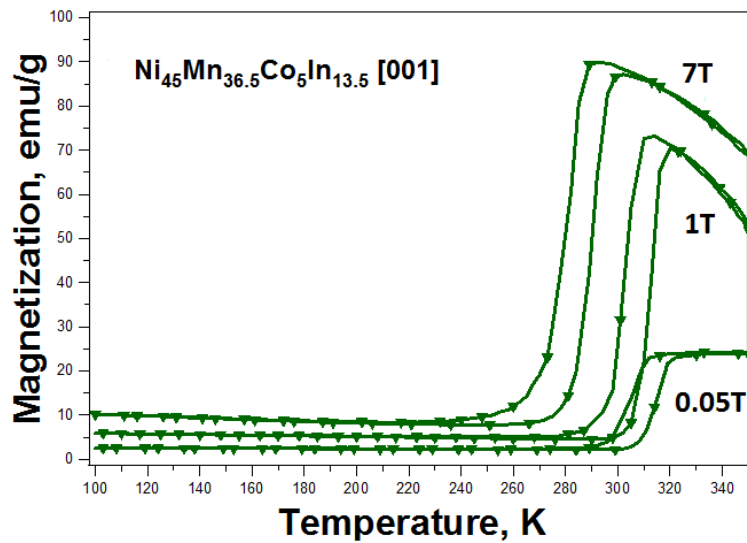
Figure 4.6 Heating cooling under applied magnetic field for magnetization measurement

Figure 4.7 shows magnetization measurements of the specimens which were heat treated at various temperatures for 3 hours. Heating cooling experiment were performed under 7 Tesla for the specimens heat treated for 3 hours at 400 °C, 500 °C, 600 °C and 700 °C. The specimen heat treated at 400 °C did not exhibit martensitic transformation under 7 Tesla which is in good agreement with DSC result. Transformation temperatures increased with heat treatment temperature. M_s of the specimen heat treated at 500 °C was -66 °C and increased to 25 °C with 700 °C heat treatment. Also, temperature hysteresis decreased drastically from 38.7 °C after 500 °C heat treatment to 10.3 °C after 700 °C heat treatment. Magnetization measurements show good agreement with DSC results in terms of transformation temperatures and hysteresis change with respect to heat treatment temperature.

In the NiMnCoIn metamagnetic shape memory alloys, Ito et al. showed kinetic arrest phenomena where martensitic transformation was interrupted at about 150 K during cooing under magnetic field [108]. Kinetic arrest was observed at around 150 K on the specimen heat treated at 500 °C during cooling under 7 T, as shown Figure 4.7. Because of this, austenite was not fully transformed to martensite. Temperature hysteresis of the specimen heat treated at 500 °C was higher than others by cause of kinetic arrest at low temperature. The specimens heat treated at 600 °C and 700 °C were not affected by kinetic arrest phenomena due to higher temperature transformation temperatures. Magnetization difference was higher after heat treatment at 600 °C than the heat treatment at 700 °C. The degree of ordering decreased with increased heat treatment temperature. Ito et al. reported that increasing degree of ordering results in higher curie temperature of austenite [23].

Thus, magnetization difference of transforming temperatures might decrease with increased heat treatment temperature from 600 °C to 700 °C.
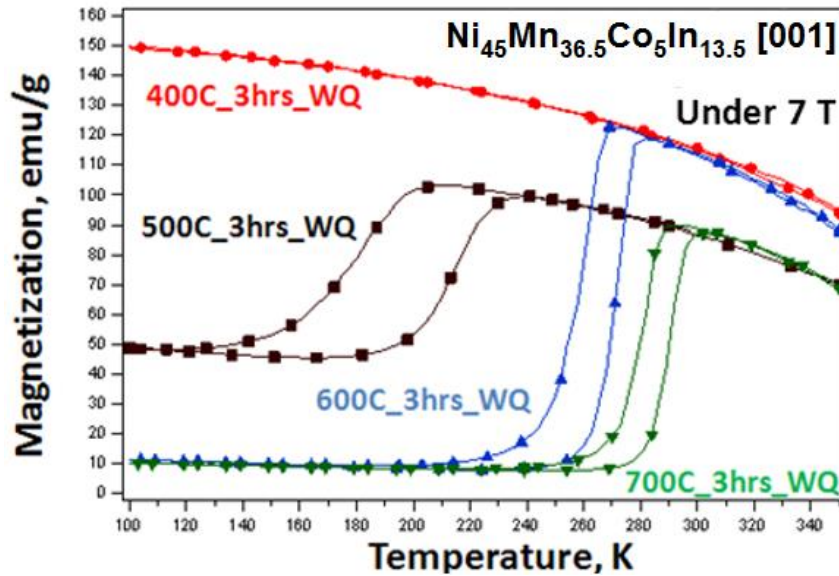
Figure 4.7 Magnetization measurement for the specimen aged at various

temperature for 3 hours

4.6   Mechanical Characterization

4.6.1   Thermal Cycling Under Constant External Stress

Thermal cycling under constant stress experiments were conducted to determine the effects of cooling rate on the shape memory effect in $Ni_{45}Mn_{36.5}Co_5In_{13.5}$ [100] oriented single crystalline shape memory alloys, as shown in Figure 4.8. Compressive stress was applied in parent phase, and thermal cycling was performed under constant stress, and then repeated for selected stress levels. Martensitic transformation was not observed below 50 MPa in furnace cooled specimen. Transformation temperatures increased with stress. Furnace cooled and oil quenched specimens were crushed during heating under 175 MPa and 100 MPa, respectively. Transformation temperatures of oil quenched specimen were

lower than the TTs of water quenched specimen and higher than the TTs of furnace cooled specimen as shown previously in DSC results.
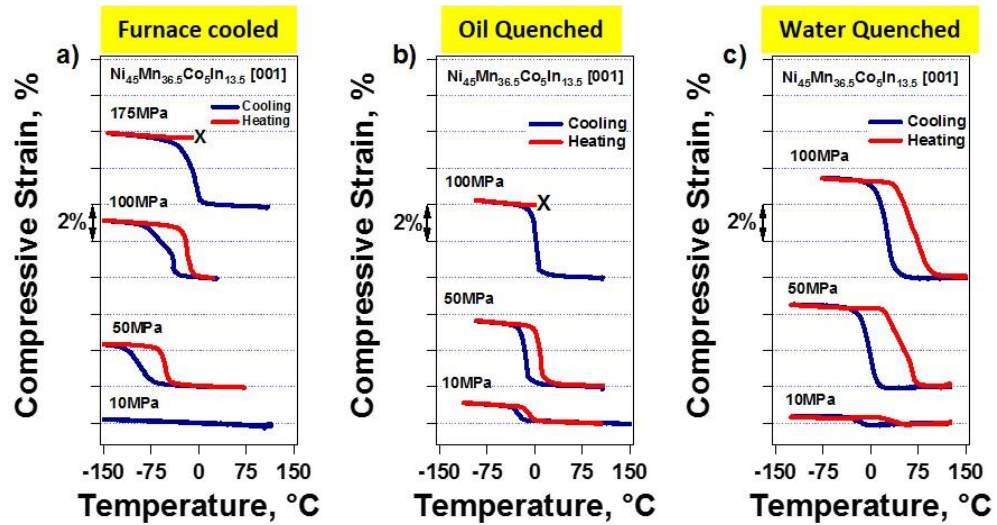
Figure 4.8 Thermal cycling test under constant compressive stress of furnace cooled, oil quenched and water quenched NiMnCoIn single crystals

Figure 4.9 shows the transformation strain as a function of applied stress determined from Figure 4.8 for each cooling condition. Transformation strain increases and then saturates with stress since the volume fraction of selected martensite variants increases with stress and transformation strain saturates by forming a single variant with sufficient applied stress. Water quenched specimen exhibited higher transformation strain of 5.5 % under 75 MPa compared with strain of 3.6 % in oil quenched and strain of 2.3 % in furnace cooled samples. It should be noted that martensitic transformation occurs from $L2_1$ Heusler type ordered cubic structure of austenite to 14M modulated structure in furnace cooled specimen [19]. Increasing the cooling rate modifies the crystal structure of austenite and makes it B2 disordered structure. Therefore, lattice parameters of the crystal structures could change slightly. Water quenched specimen with B2 disordered structure exhibited

49

higher transformation strain compared with furnace cooled or oil quenched samples which can be attributed to the change in crystal structure.
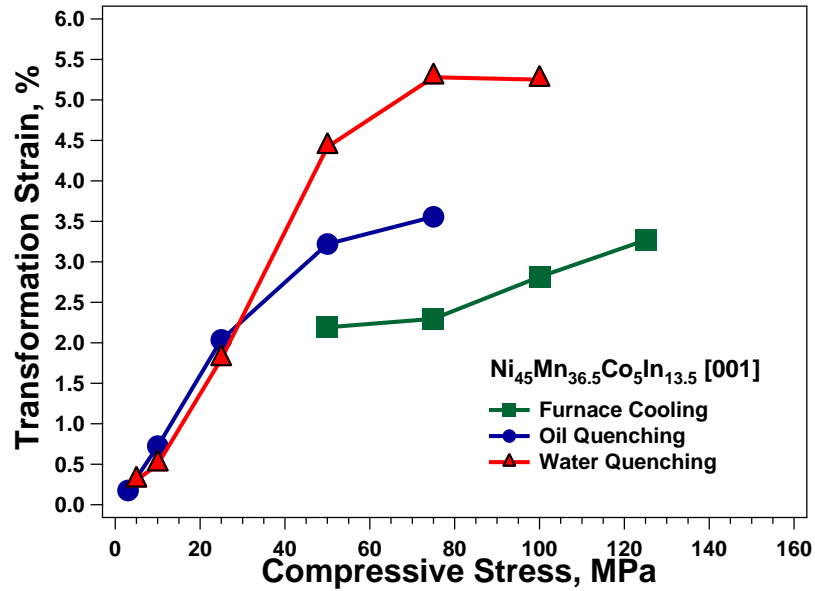
Figure 4.9 Transformation strain as a function of applied compressive stress

Temperature hysteresis, determined from Figure 4.8, with respect to compressive stress was plotted in Figure 4.10. Temperature hysteresis of oil quenched specimen was increased while furnace cooled and water quenched specimens were decreased with stress. Hysteresis in the water quenched sample was 58 °C under 10 MPa and decreased to 42 °C under 100 MPa where it was 40 °C under 50 MPa in furnace cooled sample and decreased to 24 °C. Hysteresis of the oil quenched sample was 16 °C under 10 MPa, which is lower than hysteresis of water quenched and furnace cooled specimens, and increased up to 31 °C under 75 MPa. In general, hysteresis is a result of dissipation energy, and arises from dislocation generation, friction of phase front movement and interaction of martensite variants. Since there was no irrecoverable strain observed during thermal cycling in each cooling condition of specimen, hysteresis can mainly be related to the compatibility of

transforming phases. The decrease of hysteresis with increasing stress can be explained with the decrease in dissipation due to less variant-variant interactions.
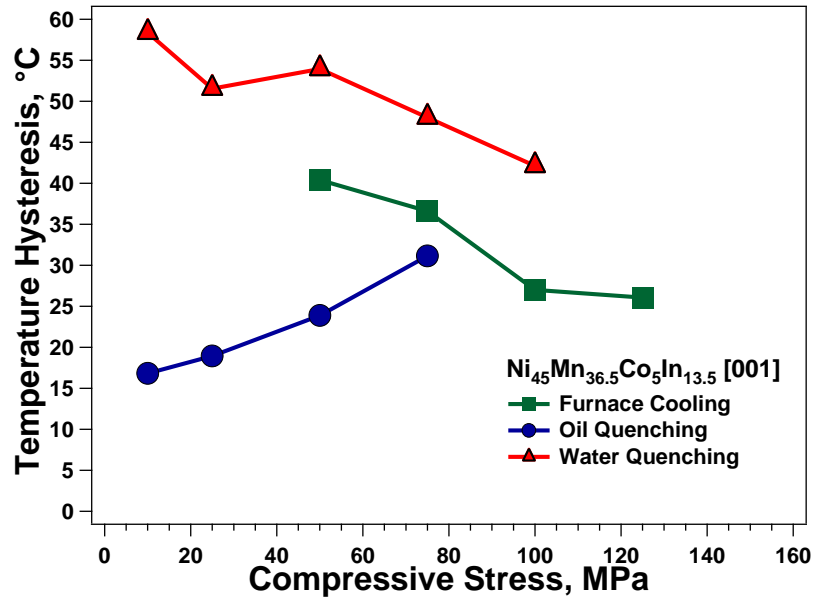
Figure 4.10 Temperature hysteresis vs. stress curve for furnace cooled, oil

quenched and water quenched sample

The results depicted in Figure 4.8 were used to plot M_s vs. stress as shown in Figure 4.11. In SMAs, M_s increases linearly with stress which is known as Clausius-Clapeyron (C-C) relationship. This linear behavior can be expressed:

$$\frac{\Delta\sigma}{\Delta T} = -\frac{\Delta H}{T_o \varepsilon_{tr}^{max}}$$

(4.1)

where $\Delta\sigma$ is the change in the critical stress, ΔT is the change in temperature, ΔH is the transformation enthalpy, T_o is the equilibrium temperature, and ε_{tr}^{max} is the maximum transformation strain. M_s of water quenched sample was determined to be -10 °C under 5 MPa from thermal cycling under stress experiments. According to C-C relationship, 1.98 MPa stress is required to modify M_s of water quenched sample per 1 °C. M_s under stress

free condition is expected to be -12.5 °C; however, it was found 4 °C from the DSC experiment. M_s values do not match exactly but close each other.

It should be noted that the transformation was not observed below 50 MPa in furnace cooled specimen. It is clear that M_s can easily be tailored to desired temperatures by changing the cooling rate for specific industrial applications.
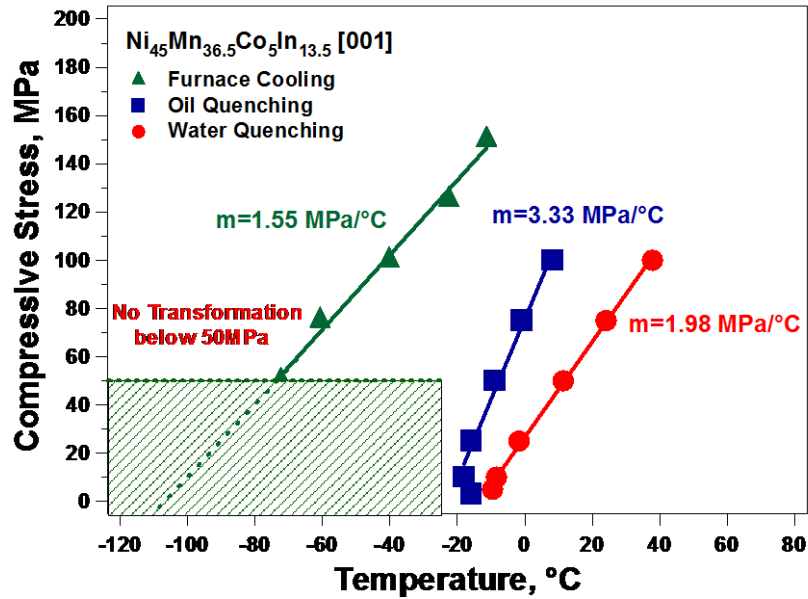
Figure 4.11 The change of Ms as a function of stress for furnace cooled, oil quenched and water quenched samples

Figure 4.12 shows the thermal cycling under compressive stress curves for the 24 hours at 900 °C homogenized sample followed by oil quenching and then heat treated for 3 hours at 600 °C followed by water quenching. The thermal cycles were repeated under 3 MPa, 10 MPa, 25 MPa and 50 MPa. Transformation temperatures and strains increased with increasing stress levels. The specimen was crushed during heating under 50 MPa. For comparison, the thermal cycling of the homogenized specimen under 25 MPa was added to the figure 4.12 with dotted lines. Transformation temperatures were higher while temperature hysteresis was lower in heat treated specimen compared with homogenized

specimen. Temperature hysteresis of solutionized specimen was obtained as 51 °C under 25 MPa and decreased to 17 °C under same stress level after the heat treatment at 600 °C for 3 hours. Additional heat treatment is an effective way to reduce temperature hysteresis drastically and increase transformation temperatures by changing the degree of interatomic ordering.
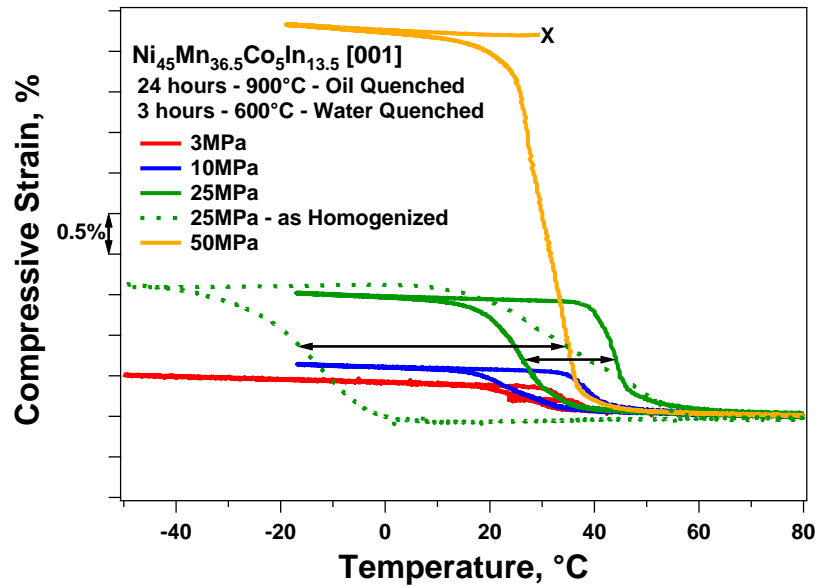
Figure 4.12 Thermal cycling under stress responses of $Ni_{45}Mn_{36.5}Co_5In_{13.5}$ single crystals heat treated for 3 hours at 600 °C followed by water quenching after the homogenization

4.6.2 Magneto-Thermo-Mechanical Experiments

Magnetic field induced shape memory effect was determined in NiMnCoIn single crystalline. The specimen was heat treated for 3 hours 650 °C after homogenization and water quenched. The sample was loaded at 10 °C (below M_f) until 4 % strain to observe stress induced strain by variant reorientation (1 to 2), as shown in figure 4.13a. After obtaining detwinned martensite, the sample was unloaded and a retained strain of 3.8 %

was observed (2 to 3). Then, magnetic field was applied up to 7 T at 10 °C to observe field induced shape recovery due to martensite to austenite transformation (3 to 4). Critical magnetic field of back transformation from detwinned martensite to austenite was 2.6 T and transformation was completed at 4.2 T magnetic field (3 to 4), as shown in figure 4.13b. Magnetic field induced strain of 3.8 % was obtained because of shape recovery during back transformation. Kainuma et al. reported magnetic field induced shape recovery around 2.9 % after pre-strain of 3 % in NiMnCoIn shape memory alloys [19]. The critical magnetic field of shape recovery was recorded above 2 T and it is in good agreement with the current study.
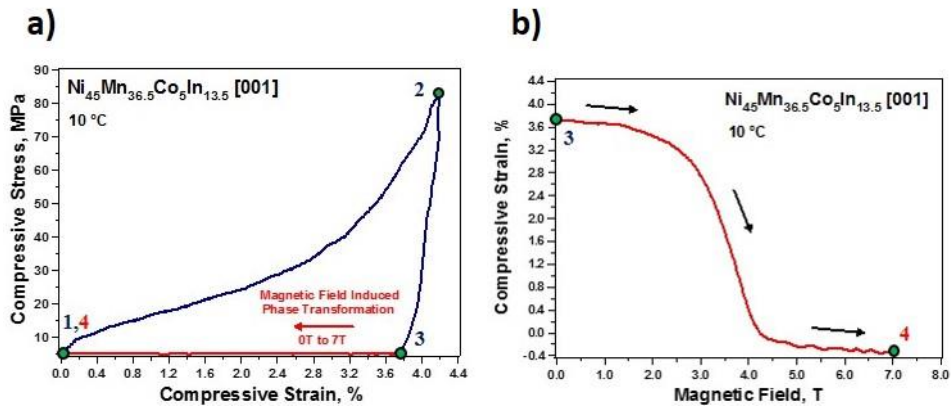
Figure 4.13 Shape memory effect in NiMnCoIn single crystalline, a) stress vs strain response b) strain recovery by applied magnetic field

In order to determine the effects of magnetic field on superelastic behavior under compressive stress, superelasticity experiments were conducted under selected constant magnetic fields, as shown in Figure 4.14. The sample was aged for 3 hours at 700 °C followed by water quenching after the homogenization. The specimen was loaded until a total strain of 1.5 % and then unloaded at 50 °C, which is close to A_f, to observe full recovery. The superelastic cycle was repeated under constant magnetic fields of 3 T, 6 T

and 9 T. Perfect superelasticity with recoverable strain of 1.5 % was observed under selected magnetic field levels. Magnetic field favors the austenite phase due to its ferromagnetism. Accordingly, additional stress is needed to induce martensite. Critical stress for martensitic transformation increased with applied magnetic field. Magnetostress, stress difference between superelastic loops, was measured at 1 % strain level for each superelastic cycle and determined as 62 MPa under 9 T magnetic field.
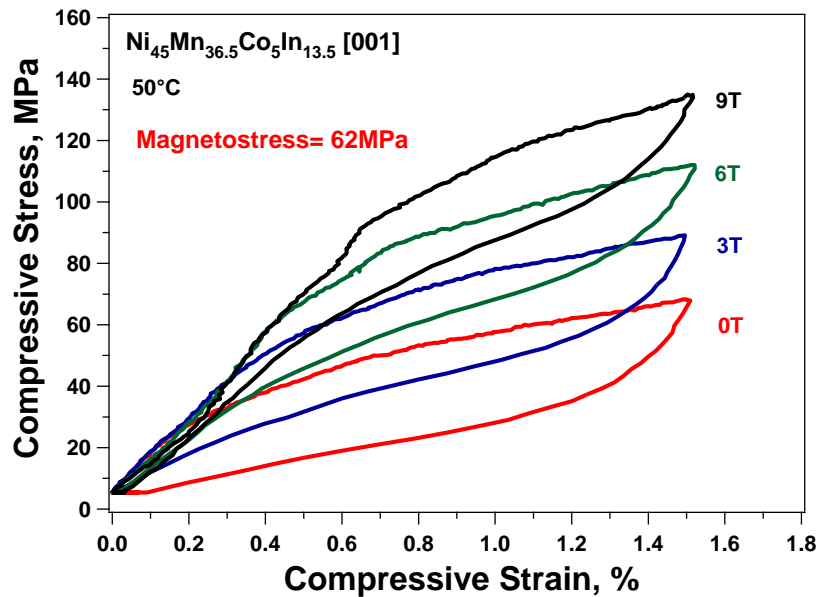
Figure 4.14 Superelastic behavior at 50 °C under magnetic field in

$Ni_{45}Mn_{36.5}Co_5In_{13.5}$ single crystalline

Superelastic loops under 9 T and field free condition were separated due to low stress hysteresis and large Zeeman energy, as shown in figure 4.14. This provides a unique opportunity to observe magnetic field induced strain under constant stress. At 90 MPa, the sample is austenite under 9 T while it is martensite under 0 T. Thus, loading the sample to 90 MPa under 9 T and then removing magnetic field results in austenite to martensite transformation. If magnetic field is applied again, martensite transforms back to austenite. Reversible MFIS could be determined by stress assisted magnetic cycling in terms of

removing and reapplying magnetic field at a constant stress. The specimen was loaded to 90 MPa at 50 °C under 9 T magnetic field where the specimen is still in austenite phase. Then, magnetic field (9 T) was removed under constant compressive stress of 90 MPa. Since applied stress is high enough for martensitic transformation under 0 Tesla and the sample transformed from austenite to martensite. Upon application of magnetic field martensite transformed back to austenite, where 1.5 % of magnetic field induced strain due to reversible phase transformation was observed, as shown in figure 4.15. The magnetic field was cycled three times to determine the stability of reversible field induced phase transformation.
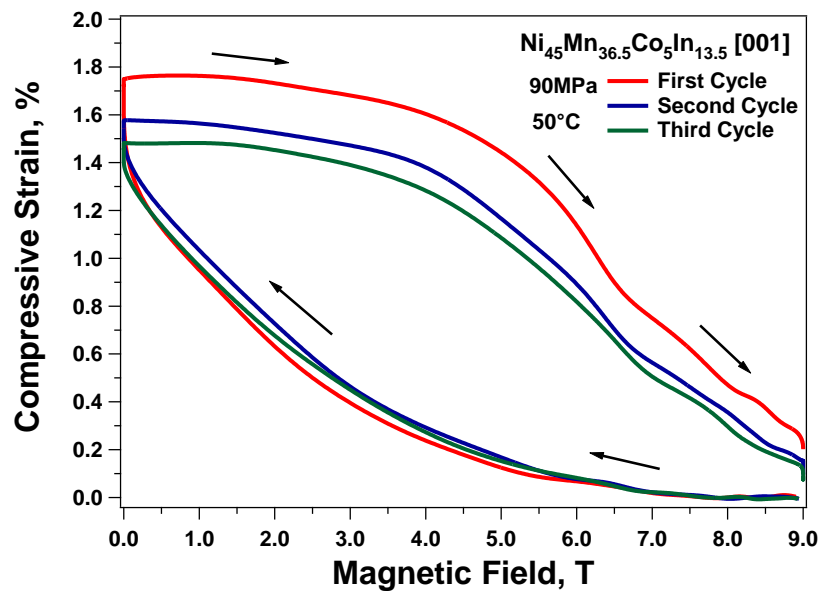
Figure 4.15 Magnetic field induced reversible phase transformation in

Ni$_{45}$Mn$_{36.5}$Co$_5$In$_{13.5}$ single crystalline under 90 MPa at 50 °C

Magnetic field induced strain in magnetic shape memory alloys has been widely investigated to achieve large MFIS and high output stress for actuators and sensors applications. Large MFIS by variant reorientation was reported in many magnetic shape memory alloys. Limited driving force in variant reorientation mechanism lead to explore the potential of the magnetic field induced phase transformation (MFIPT) mechanism in metamagnetic shape memory alloys. Krenke et al. reported strain of 0.12 % with magnetic superelasticity of $Ni_{50}Mn_{34}In_{16}$ polycrystalline without stress [20]. Liu et al. showed magnetostrain of 0.25 % under 5T magnetic field after magnetic training in textured $Ni_{45.2}Mn_{36.7}In_{13}Co_{5.1}$ [21]. Kainuma et al. presented 0.3 % reversible magnetic field induced strain in NiCoMnSn polycrystalline [109]. In the current study, 1.5 % reversible magnetic field induced strain and 62 MPa magnetostress in NiMnCoIn single crystalline show very promising properties for actuator applications.

Effects of magnetic field on the shape memory effect were revealed by thermal cycling under 25 MPa with selected magnetic fields of 0, 3, 6 and 9 T, as shown in Figure 4.16. Transformation strain under 25 MPa was approximately 3.5 % and decreased slightly with applied magnetic field due to incomplete martensitic transformation. Transformation temperatures shifted to lower temperatures with magnetic field where M_s was decreased by 39 °C when 9 T was applied.
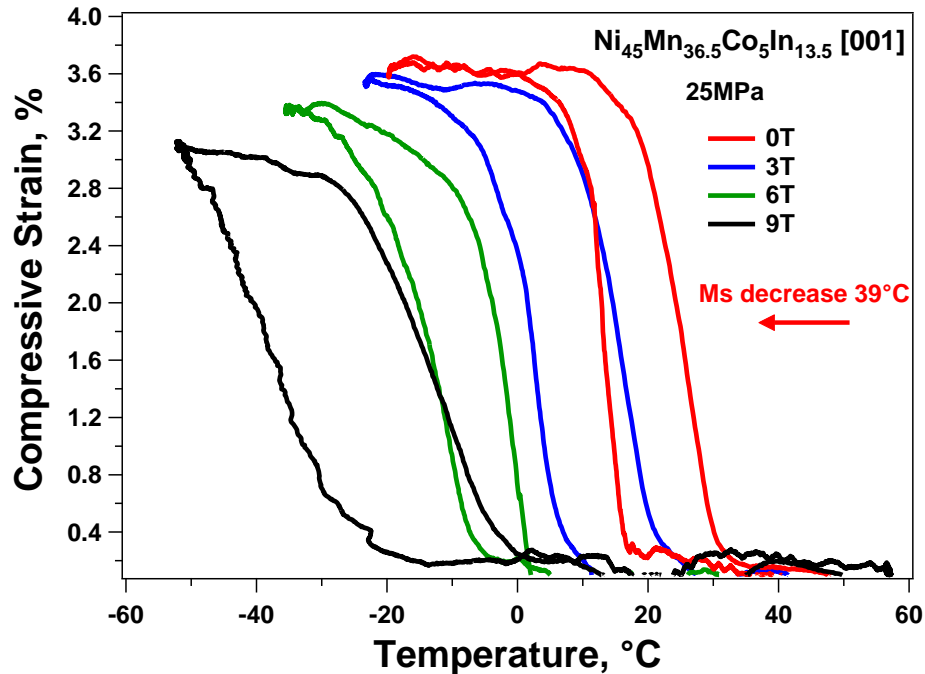
Figure 4.16 Heating cooling under constant stress and magnetic field in

$Ni_{45}Mn_{36.5}Co_5In_{13.5}$ single crystalline

4.7   Conclusions

Effects of heat treatment temperature and cooling rate on the transformation temperatures, magnetizations behavior, hysteresis and mechanical properties were studied in NiMnCoIn single crystals along the [001] orientation. Moreover, the effect of magnetic field on superelasticity and thermal cycling experiments were conducted. The summarization of the results:

1. Transformation temperatures can be tailored by adjusting the cooling rates and heat treatment temperatures by virtue of the modification of interatomic ordering. Crystal structure of austenite changes from ordered $L2_1$ cubic to B2 disordered structure with increased cooling rate. Moreover, transformation temperatures were increased and saturated with increasing heat treatment temperature. Last heat

treatment and cooling rate were effective on transformation temperatures when more than one heat treatment was conducted. Temperature hysteresis also decreased with increasing second heat treatment temperature.

2. XRD experiments were conducted at room temperature and 200 °C to reveal lattice parameters and crystal structure of transforming phases. Crystal structures of martensite and austenite were determined as monoclinic 14M and cubic $L2_1$, respectively. The lattice parameter of the cubic $L2_1$ austenite is $a = 0.5975$ nm and monoclinic 14M is $a = 0.4346$ nm, $b = 0.5571$ nm, $c = 3.0697$ nm and $\beta = 93.5°$.

3. Ferromagnetic parent phase and weakly magnetic martensite phase were confirmed with magnetic measurement. Magnetic field decrease the transformation temperatures due to ferromagnetic parent phase. Heat treatment temperature increase the TTs and magnetic measurement was in good agreement with DSC results.

4. Thermal cycling under stress experiments showed that water quenched specimen presented higher transformation strain of 5.5 % under 75 MPa compared with strain of 3.6 % in oil quenched, and strain of 2.3 % in furnace cooled samples. Furnace cooled samples did not show any transformation below 50 MPa. Crystal structure difference between water quenched and furnace cooled samples influenced the recoverable strain. Moreover, temperature hysteresis under 25 MPa decreased 34 °C with additional heat treatment at 600 °C for 3 hours, followed by water quenching.

5. Upon application of 7 T, magnetic field induced recovery strain of 3.8 % was determined after stress induced martensite reorientation at 10 °C. Critical magnetic

field of back transformation was recorded as 2.6 T and recovery completed at 4.2 T.

6. Magnetostress of 62 MPa was obtained in superelasticity experiments with strain of 1.5 % at 50 °C under 9 T magnetic field. Stress assisted magnetic field induced reversible phase transformation tests were conducted and recoverable strain of 1.5 % under 90 MPa were determined. Reversible MFIS of 1.5 % is five times higher than achievement of previous studies in magnetic shape memory alloys.

7. Thermal cycling under stress and magnetic field experiment showed that transformation temperatures decreased 39 °C when magnetic field of 9 T applied under 25 MPa

5 Magneto-Thermo-Mechanical Behavior of Single Crystalline of NiMnCoIn Metamagnetic Shape Memory Alloys

5.1 Introduction

The effects of the magnetic field on the shape memory behavior of [001]-oriented metamagnetic NiMnCoIn shape memory single crystals were investigated. Transformation temperatures, magnetization behavior of austenite and martensite under various magnetic field and microstructure will be presented in this chapter.

In addition, thermal cycling under constant stress and magnetic field, and superelasticity under constant magnetic field tests were conducted to understand their magneto-thermo-mechanical behavior. Phase diagrams under magnetic field will be revealed. Moreover, orientation dependence of shape memory behavior and magnetostress will be exhibited.

5.2 DSC Results

Figure 5.1a shows the DSC response of the NiMnCoIn single crystal. The exothermic peak corresponds to the forward transformation upon cooling and the endothermic peak corresponds to the back transformation during heating. During cooling, the M_s and M_f were found to be 91.2 °C and 37.2 °C, respectively. A_s and A_f were determined to be 56.9 °C and 104.1 °C. The small peak observed at 115 °C indicates the Curie temperature of austenite. Figure 5.1b shows the microstructure of as-grown sample at room temperature. The sample was found to be in martensite phase at room temperature since M_f was determined as 37.2 °C by DSC. In addition to martensite variants, second phase structures can be clearly seen in the optical micrograph. The chemical composition of matrix and second phases were determined by SEM/EDS. Composition of the martensite

matrix was found as $Ni_{44.6}Mn_{36.6}Co_{4.8}In_{14}$, whereas second phase (dark region) and small particles (white region, highly Co rich) were obtained as $Ni_{44}Mn_{36.1}Co_{5.7}In_{14.2}$ and $Ni_{40.1}Mn_{38.6}Co_{20.2}In_{1.1}$, respectively. It should be noted that the transformation temperatures of $Ni_{44.6}Mn_{36.6}Co_{4.8}In_{14}$ were determined relatively higher than expected in $Ni_{45}Mn_{36.5}Co_5In_{13.5}$ from literature due to slightly different matrix composition and second phase formation during fabrication which can be seen clearly from optical image in figure 5.1b [12].
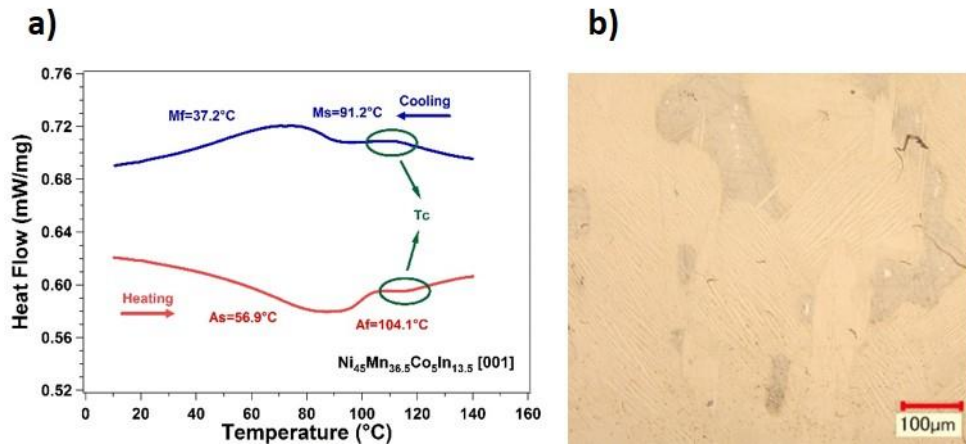
Figure 5.1 a) DSC response of NiMnCoIn single crystal and b) Optical image of microstructure at room temperature

5.3 Magnetic Measurements

Phase transformation behavior of the single crystals was monitored by the change in magnetization during temperature cycling under constant magnetic field experiments, as shown in Figure 5.2. Selected magnetic fields from 0.05 T to 12 T were applied in austenite phase and temperature was cycled between 127 °C and -173 °C. Under 0.05 T, forward transformation began at 79 °C and ended at 12°C while back transformation began at 33 °C and completed at 95 °C. Under 12 T, austenite transformed to martensite between 25

°C and -69 °C, while the reverse martensitic transformation started at -30 °C and ended at 57 °C. It is clear that transformation temperatures shifted to lower temperatures by increasing the magnetic field. On the contrary, the maximum difference of magnetization between the austenite and martensite phases was determined to be 32.4 emu/g under 0.05 T, 41.1 emu/g under 3 T and 30.4 emu/g under 12 T. Ito et al. reported that martensitic transformation is arrested during field cooling and is not continued with further cooling in metamagnetic shape memory alloys due to disappearance of driving force [108]. Thus, we can conclude that in NiMnCoIn single crystals, austenite stabilizes at low temperatures upon field cooling under magnetic fields of 3 T or higher, resulting in incomplete phase transformation and decreased magnetization difference.
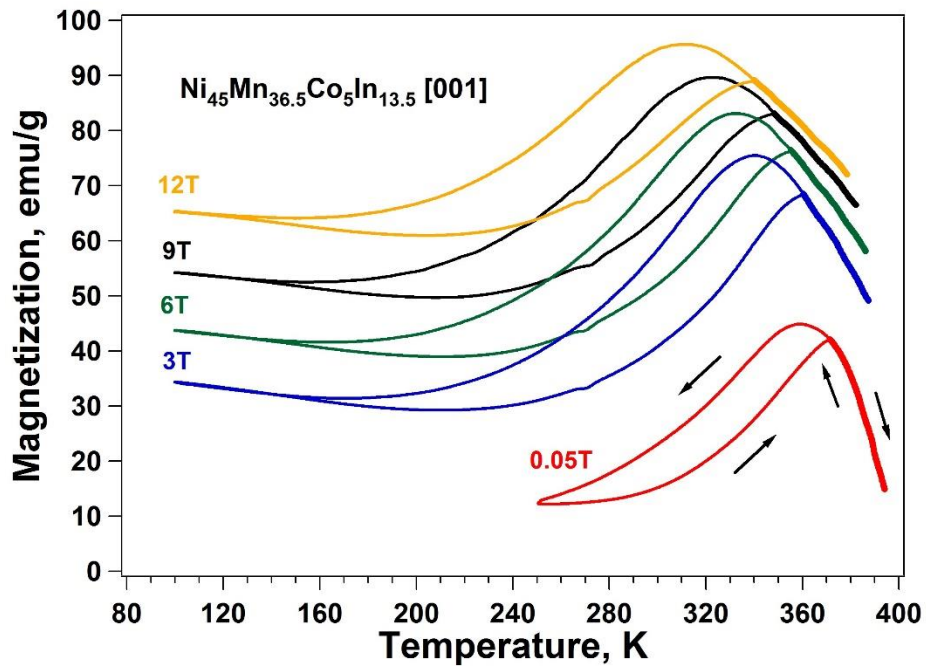
Figure 5.2 Magnetization vs. temperature response of NiMnCoIn single crystal under selected magnetic fields

Magnetization versus magnetic field responses of NiMnCoIn single crystals were measured at selected temperatures to reveal the magnetic field induced phase transformation behavior, as shown in Figure 5.3. The specimen was cooled down to -113 °C and heated up to selected temperatures of -73 °C, -33 °C and 7 °C to ensure that the initial structure is in fully martensite phase. Measurement temperatures were selected to be close to A_s in order to observe the reversible phase transformation by applied magnetic field. Magnetic field is applied up to 14 T and then removed at constant temperature. It is clear from the magnetization response with hysteresis that magnetic field induced martensite to austenite phase transformation was occurred with applied magnetic field. Depending on the temperature, austenite transformed back fully (-73 °C) or partially (7 °C) to martensite upon removing the magnetic field.
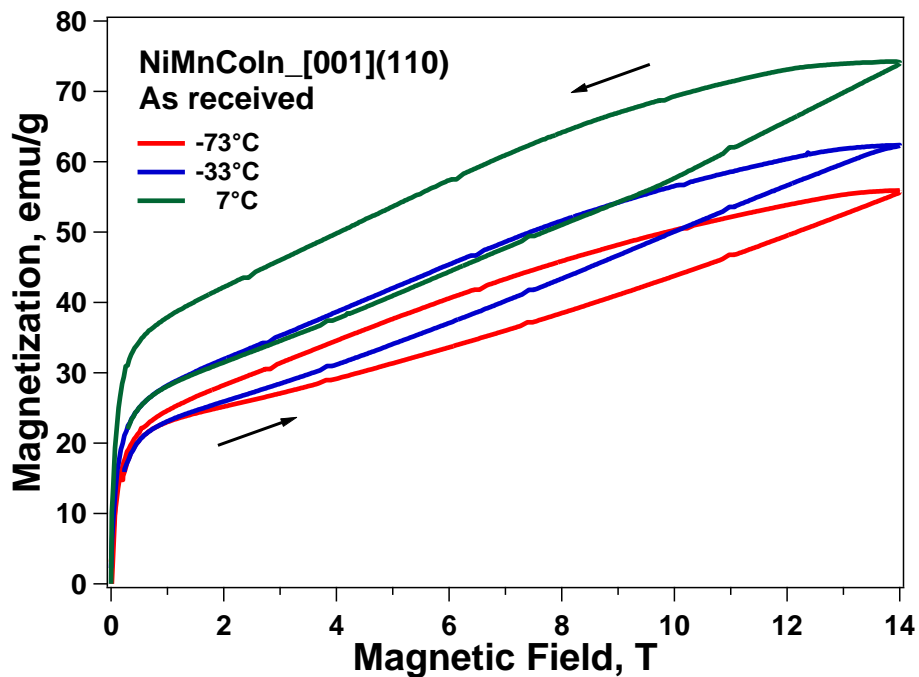
Figure 5.3 Magnetization curves at several temperatures in martensite phase

It should be noted that although magnetization as a function of temperature under constant magnetic field or magnetic field at selected temperatures provides useful information about the magnetization behavior and transformation temperatures, it does not provide any information about the shape memory properties such as transformation strain and critical stress for transformation which are very important parameters for actuator applications.

5.4   Thermal Cycling Under External Stress

Cooling–heating under constant compressive stress experiments were conducted to determine the shape-memory behavior and the effects of applied stress on the transformation temperatures, as shown in Figure 5.4. The compression stress was isothermally applied in austenite and the specimen is cooled down to a temperature below M_f and then heated up to a temperature above A_f under constant applied stress. After the thermal cycle was completed, the applied stress level was increased to next level between 5 MPa and 175 MPa and thermal cycling was repeated. Upon cooling under 50 MPa, forward transformation started at 87.6 °C and during heating, martensite phase completely transformed back to austenite phase at 112.5 °C. Transformation strain of 1.2 % was observed under 50 MPa. By increasing the applied stress to 150 MPa, transformation temperatures (M_s = 97 °C, M_f = 20.4 °C, A_s = 57.2 °C and A_f = 136.2 °C) were shifted to higher temperatures. Transformation strain was increased to 5.2 % under 150 MPa. Irrecoverable strain was not observed during heating-cooling under stress levels up to 175 MPa.
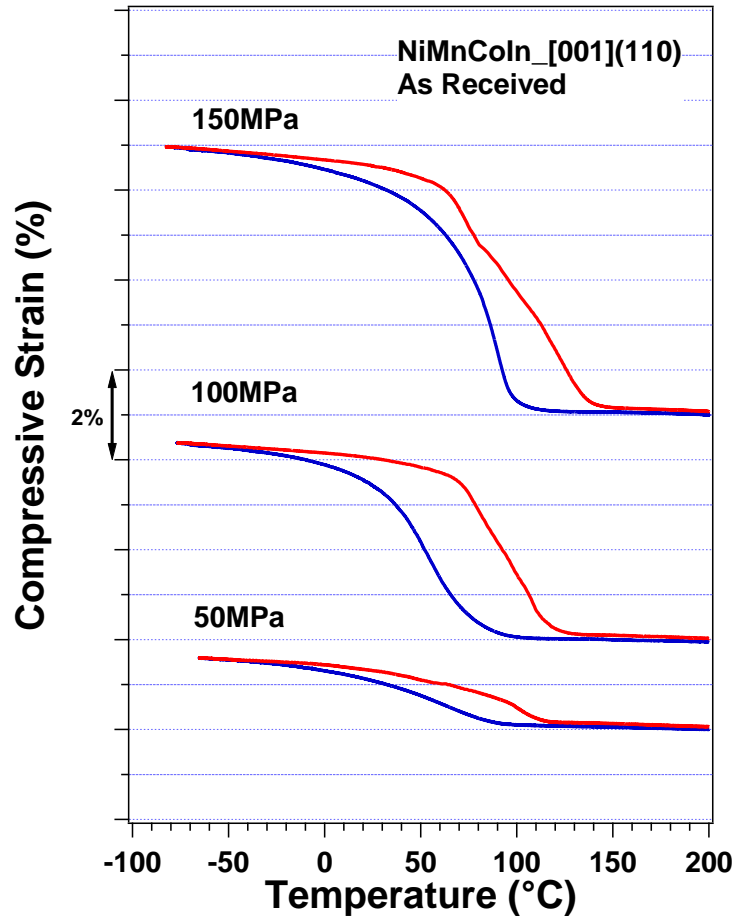
Figure 5.4 Thermal cycling under constant compression stress in the NiMnCoIn

single crystalline

5.5   Superelasticity Under Magnetic Field

Figure 5.5 shows the compressive superelastic response of NiMnCoIn single

crystals along the [001] orientation at 90 °C under selected constant magnetic fields. At the

selected temperature of 90 °C (close to A_f) to observe superelasticity with fully recoverable

strain, the magnetic field was applied parallel to the compressive stress direction from 0 T

to 9 T and was maintained to remain constant during compressive loading and unloading.

Compressive stress was applied till the strain of 2 % and then unloaded. It was clearly seen

that the superelastic loops shifted to higher stress levels with magnetic field. In other words,

an increase in critical stress for transformation was observed with applied magnetic field while the hysteresis was not affected.
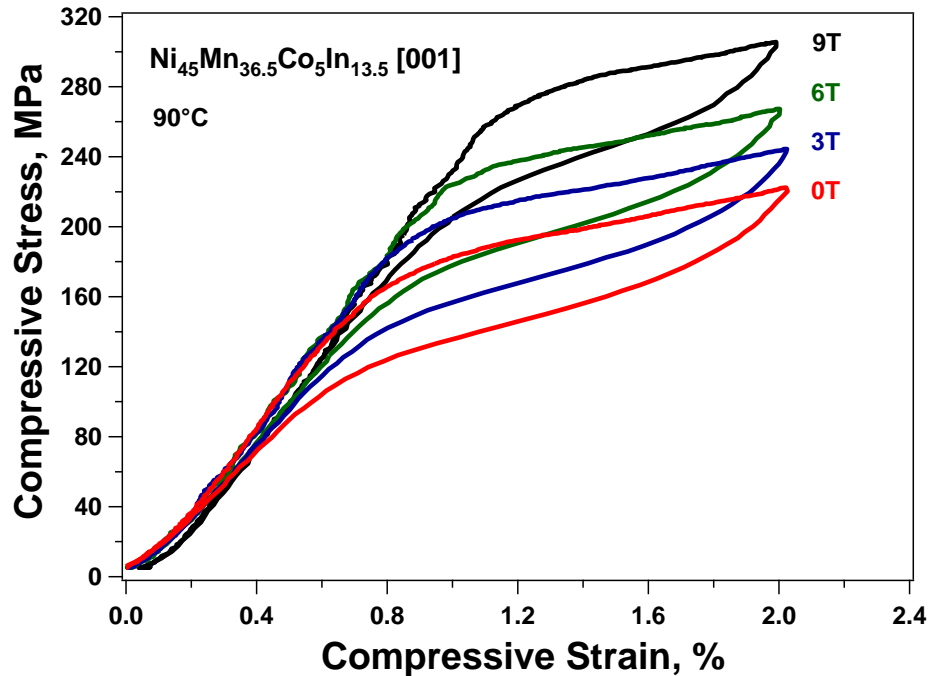
Figure 5.5 Superelastic behavior of [001]-oriented NiMnCoIn single crystals under selected magnetic fields

Since magnetic field favors parent phase due to its ferromagnetic behavior instead of non-magnetic martensite, higher stress levels are required for austenite to martensite phase transformation under magnetic field. Because of this, the superelastic behavior loops shifted to higher stress levels with increased applied magnetic field. On a different perspective, it can also be stated that magnetic field lowers the transformation temperatures and, accordingly higher stress levels are required for phase transformation at the selected temperature. Moreover, stress hysteresis did not significantly changed with applied magnetic field. The magnetostress was determined as the difference in the stress levels at 1.6 % strain from Figure 5.5. Magnetostress was 21 MPa under 3 T, which increased up to

85 MPa under 9 T. The magnetostress values were also increased linearly with magnetic field at a rate of 10.7 MPa/Tesla.

5.6   Phase Diagram

Figure 5.6 shows the superelasticity behavior of [001]-oriented NiMnCoIn single crystals at selected temperatures from 60 °C to 100 °C under 0, 3, 6 and 9 T magnetic fields. Critical stresses for phase transformation increased with temperature under selected magnetic fields. Since 60 °C and 70 °C were lower than A_f, perfect superelasticity was only obtained under high magnetic field levels such as 6 T and 9 T. It should be noted that the single crystal shows perfect superelastic behavior at 100 °C. Thus, the alloy can also be qualified as a high temperature magnetic shape memory alloy.
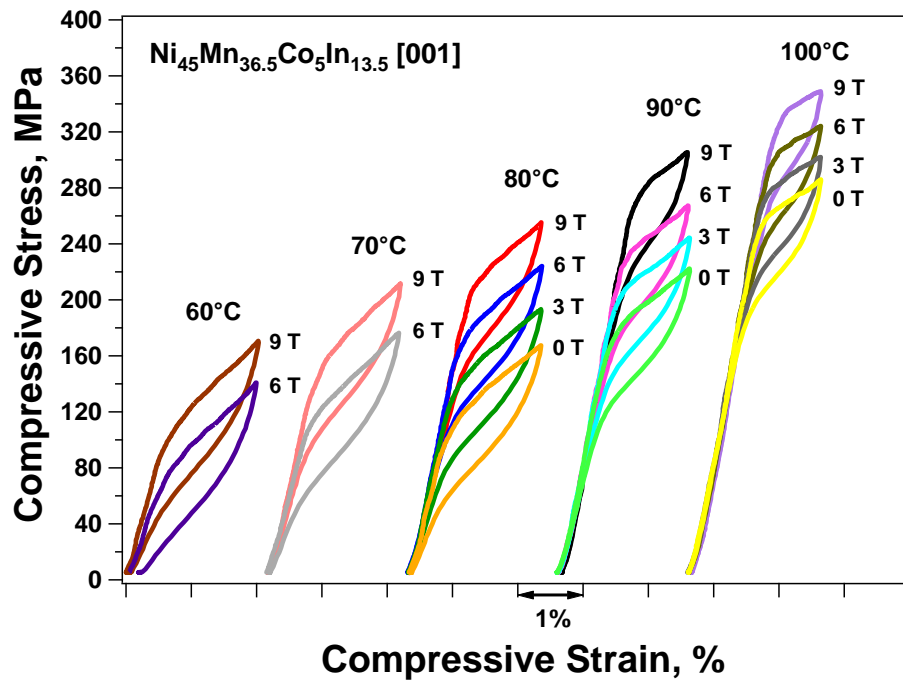
Figure 5.6 Superelastic behavior of [001]-oriented NiMnCoIn single crystals at various temperature under selected magnetic fields

Critical stress for forward transformation as a function of temperature and magnetic field levels, obtained from figure 5.6, were plotted in figure 5.7. M_s linearly increased with stress and C-C slopes under selected magnetic fields were 7.4 MPa/°C under 0 T and decreased to 5.6 MPa/°C at 9 T. It is worth mentioning that the increase in critical stress was more pronounced with a decrease in temperature. Since 100 °C is very close to curie temperature of austenite, the effects of magnetic field on critical stress diminishes due to decreased difference of the saturation magnetization of transforming phases.
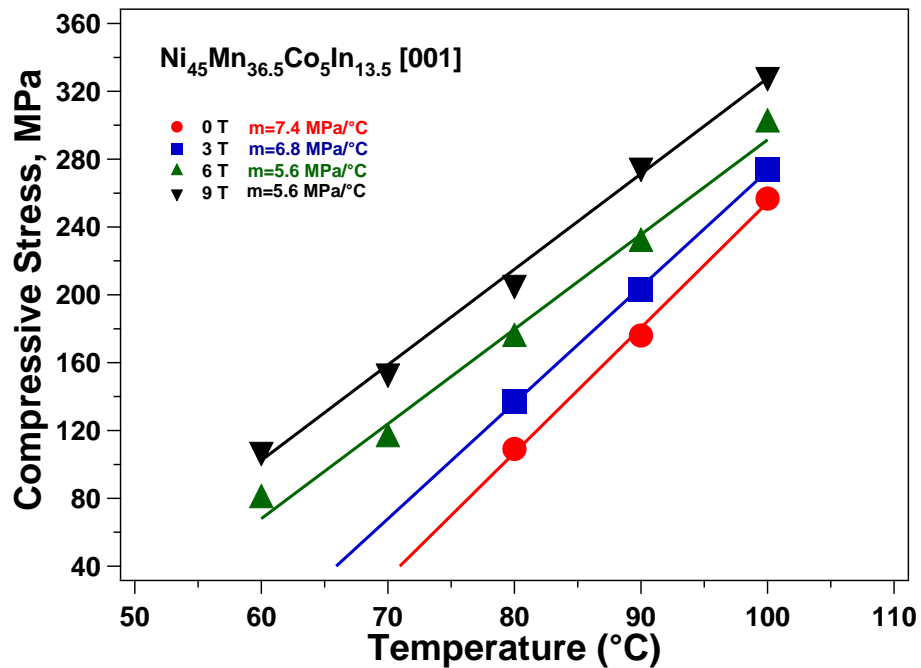
Figure 5.7 Stress – temperature phase diagram for each magnetic field levels

5.7 Thermal Cycling Under External Stress and Magnetic Field

In order to determine the effects of magnetic field on the shape memory effect, thermal cycling was conducted under 150 MPa under selected magnetic fields of 0, 3, 6 and 9 T, as shown in Figure 5.8. Transformation strain under 150 MPa was determined about 4 % and decreased slightly with applied magnetic field as a result of incomplete

martensitic transformation. It is clear that transformation temperatures shifted to lower temperatures with magnetic field. M_s was 97.8 °C under 0 T which decreased to 76.8 °C under 9 T. Thus, transformation temperatures were decreased by 19 °C when 9 T was applied.
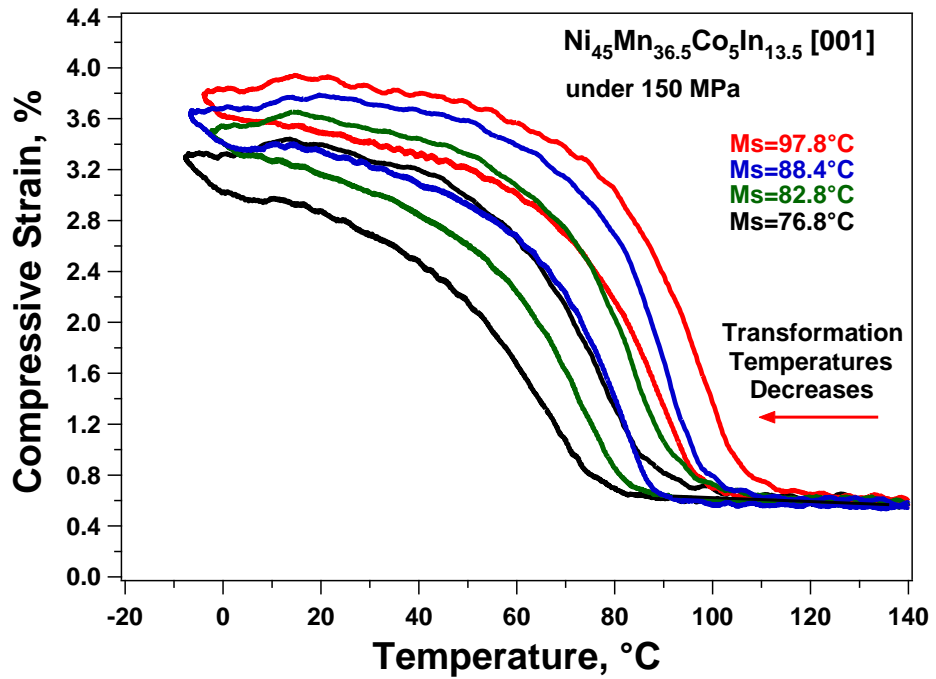
Figure 5.8 Thermal cycling under 150 MPa and at selected magnetic fields of [001]-oriented NiMnCoIn single crystal
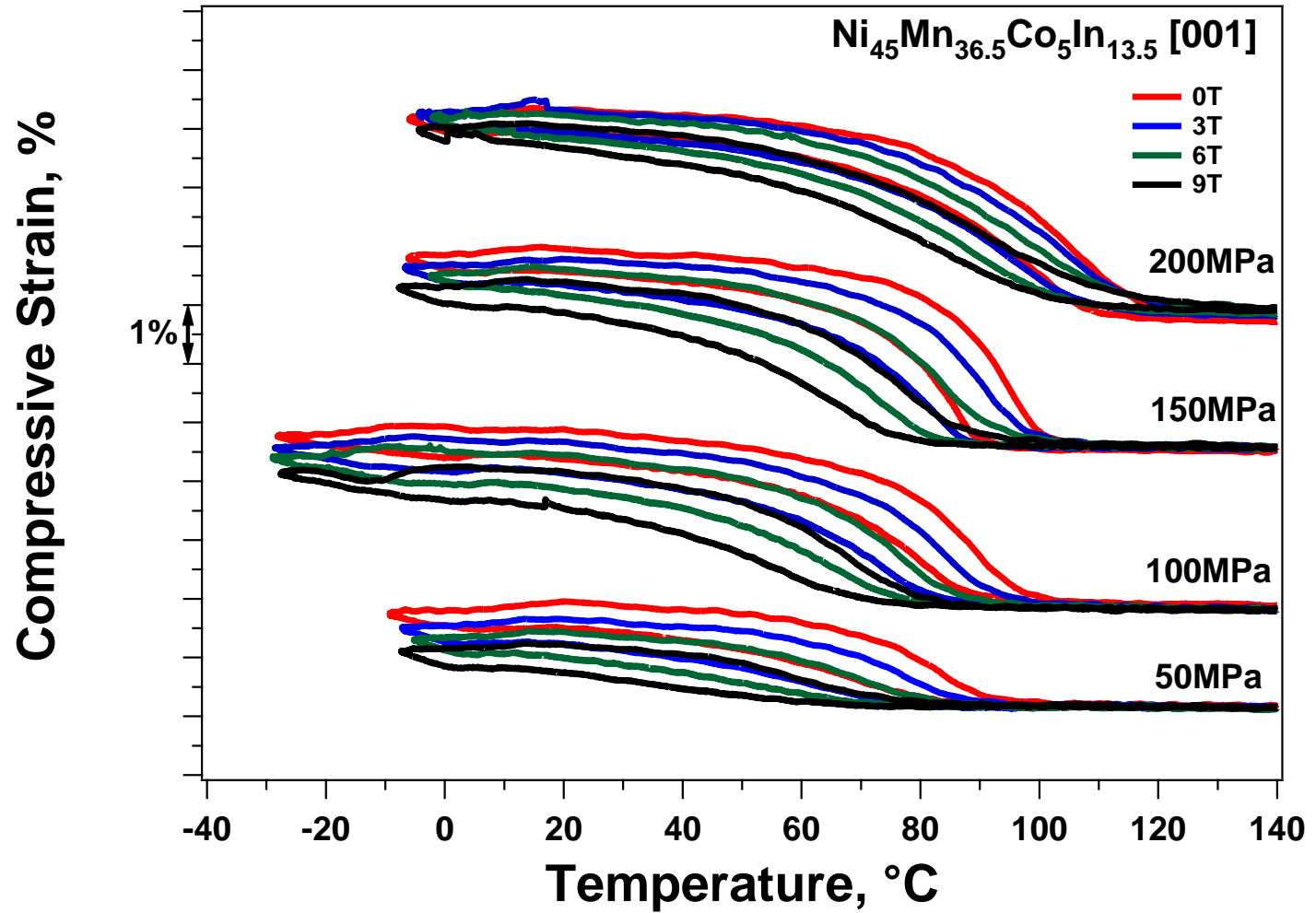
Figure 5.9 Thermal cycling at selected stresses and magnetic fields of [001]-oriented NiMnCoIn single crystal

Thermal cycling was carried out under stress from 50 MPa to 200 MPa at magnetic field from 0 T to 9T, as shown in figure 5.9. Applied stress increased TTs; however, magnetic field decreased TTs. Martensite start temperature as a function stress for each selected magnetic field was exhibited in figure 5.10. Stress-temperature curves that correspond to each magnetic field level were parallel each other. It should be noted that M_s increased to above 100 °C under 200 MPa and M_s shifted higher temperatures at 3T, 6T and 9T due to magnetization drop in curie temperature.
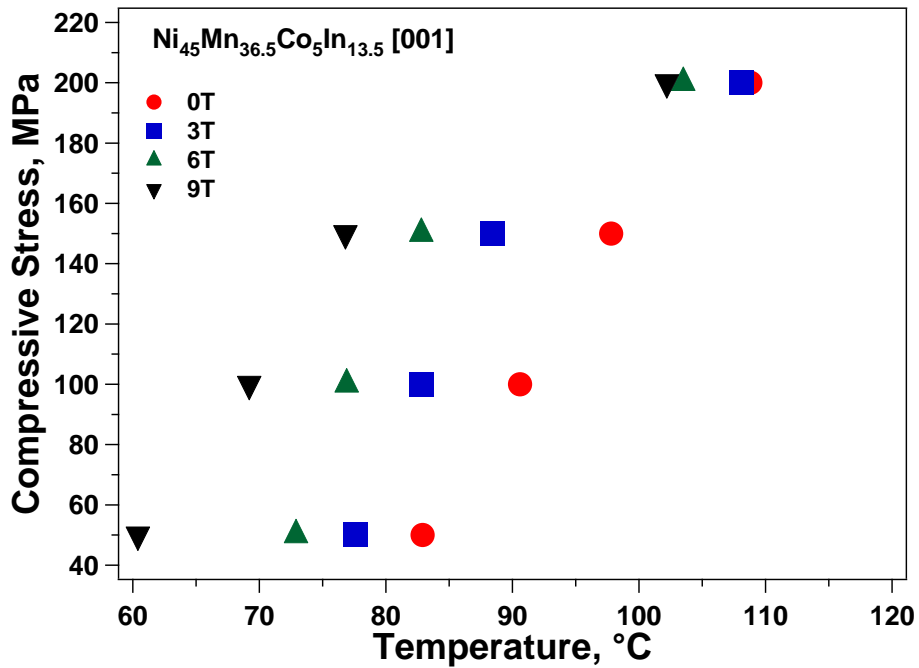
Figure 5.10 M_s as a function of applied stress and magnetic field

Figure 5.11 presents the magnetostress levels as a function of applied magnetic field obtained from the phase transformations in NiMnCoIn alloys, and both phase transformation and variant reorientation in the NiMnGa alloys along the [100] orientation [9, 11, 12]. In previous studies on NiMnGa alloys, magnetostress initially increases linearly with the applied magnetic field and then saturates above a certain magnetic field due to

limited MAE, resulting in magnetostress values of less than 10 MPa. In NiMnCoIn alloys, magnetostress increases with applied magnetic field since there is no limit for the Zeeman Energy. In the present study, NiMnCoIn single crystalline shows 85 MPa magnetostress under 9 T at 100 °C which is more than two times higher of the previous study in NiMnCoIn alloys (30 MPa at 0 °C) [12] and almost one order higher than other magnetic shape memory alloys (2–8 MPa for NiMnGa alloys) [9, 11, 79].
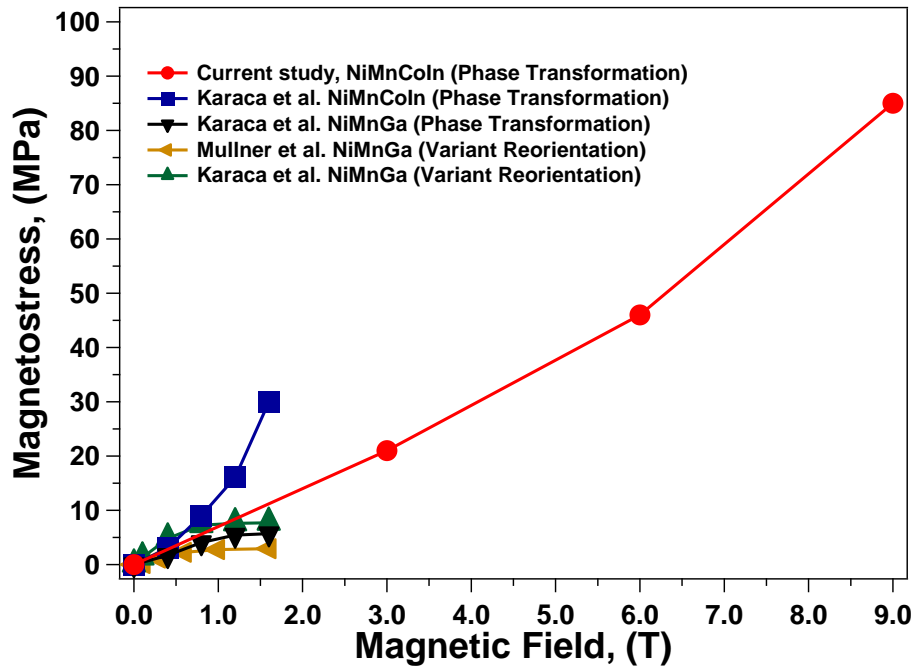
Figure 5.11 Magnetostress values of [001]-oriented NiMnCoIn single crystals as a function of applied magnetic field. For comparison, previously reported magnetostress values of NiMnGa and NiMnCoIn single crystals are also added to the graph [9, 11, 21, 47]

5.8 Theoretical Calculation of Field Induced TT Change

If the change in critical stress for phase transformation with temperature ($\Delta\sigma/\Delta T$) and the change in critical stress for martensitic transformation with applied field ($\Delta\sigma/\Delta H$) are known, the change in transformation temperature with applied magnetic field ($\Delta T/\Delta H$) can be calculated as follows;

$$\frac{\Delta T}{\Delta H} = \frac{\Delta T}{\Delta\sigma} X \frac{\Delta\sigma}{\Delta H} \tag{5.1}$$

It should be noted that at the temperatures close to Curie temperature where saturation magnetization is highly temperature dependent (Figure 5.2, ($\Delta\sigma/\Delta T$), it is also magnetic field dependent. Moreover, $\Delta\sigma/\Delta H$ is also temperature dependent (Figure 5.6 and 5.7). Given this information, equation 5.1 can only be used as an approximation to determine the changes in transformation temperatures with magnetic field when it is tested at vicinity of the temperatures where $\Delta\sigma/\Delta H$ is determined and saturation magnetization of phases are constant. However, it will still provide a good approximation for the calculated values.

($\Delta\sigma/\Delta T$) was determined as 6.7 MPa/°C from the thermal cycling under constant stress experiments under no magnetic field (Figure 5.8) and the change in critical stress for martensitic transformation with applied field ($\Delta\sigma/\Delta H$) was determined as 10.7 MPa/Tesla from superelasticity experiments under constant magnetic fields at 90 °C (Figure 5.5). Using Equation 5.1, the change in transformation temperature with applied magnetic field ($\Delta T/\Delta H$) can be calculated as -1.6 °C/Tesla which would change the TTs by -14.4 °C when 9 Tesla is applied. The calculated temperature shift of 14.4 °C is lower than the experimentally observed value of 19 °C obtained from thermal cycling under 150 MPa and

9 Tesla. The difference can be attributed to the changes in saturation magnetization of transforming phases with temperature and stress. It should be noted that saturation magnetization decreases drastically at temperatures close to Curie temperature where the current superelasticity tests were conducted.

5.9   Orientation Dependence

Temperature cycling response of NiMnCoIn single crystals along the [001], [110], and [111] orientations under 150 MPa compressive stress are shown in figure 5.12. Transformation strains were 5.2 % in [001], 1.7 % in [110] and 0.7 % in [111] oriented specimens. Irrecoverable strain was not observed in any oriented specimens under 150 MPa. Furthermore, temperature hysteresis was 20 °C, 40 °C and 17 °C in [001],   [110] and [111] oriented specimens, respectively.
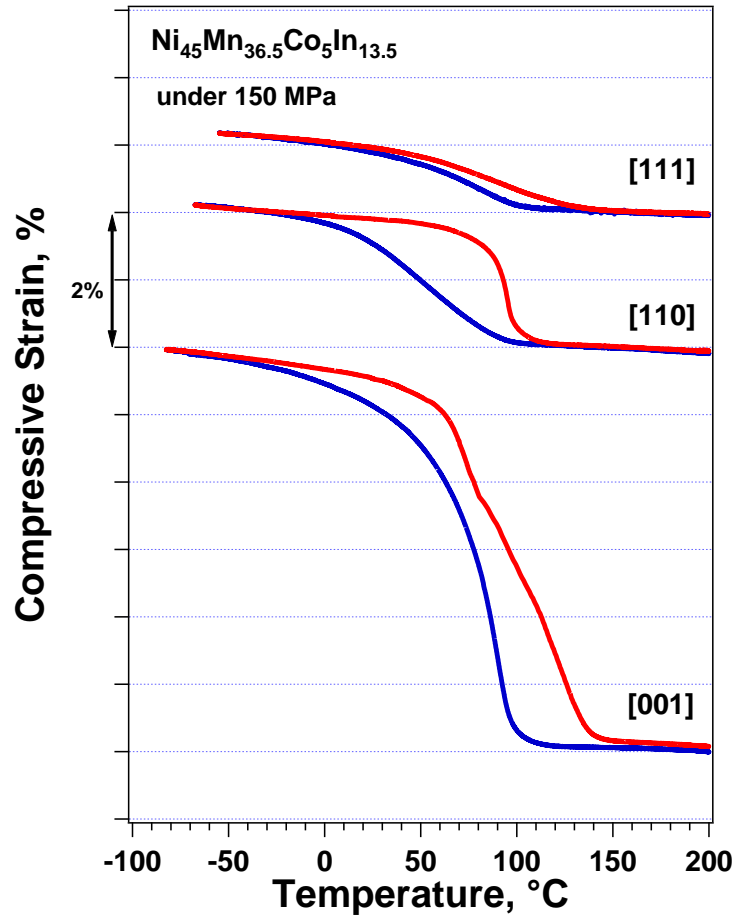
Figure 5.12 Thermal cycling of NiMnCoIn single crystals along the [001], [110] and [111] specimens under 150 MPa.

5.10 Superelasticty and SME Under Magnetic Field in [110]-Orientation

Superelastic response of NiMnCoIn single crystals along the [110] orientation at 90 °C under selected constant magnetic fields are shown in figure 5.13. The specimen was loaded until 2 % and then unloaded. The superelastic loops shifted to higher stress levels with applied magnetic field from 0T to 9T. Magnetostress value of 160 MPa was obtained under 9 T. Transformation continued up to 3.4 % after unloading (in force control) the specimen at strain of 2 % under 0 T due to plateau-type transformation. The retained strain of 2.2 % was fully recovered after heating above A_f.
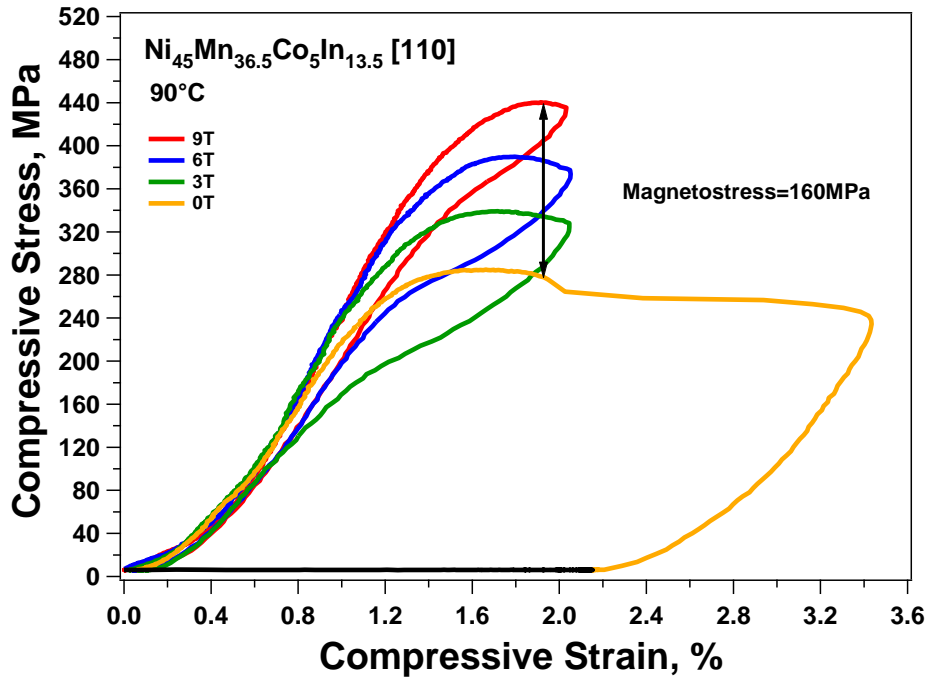
Figure 5.13 Superelastic response of NiMnCoIn single crystals along the [110] oriented specimen under magnetic field.

Figure 5.14 shows the thermal cycling of [110] oriented NiMnCoIn single crystal under 150 MPa and magnetic fields from 0 T to 9 T. Transformation strain was determined to be about 3.5 % under 150 MPa and decreased slightly with applied magnetic field due to incomplete martensitic transformation. Transformation temperatures decreased with applied magnetic field. M_s was 68.8 °C under 0 T which decreased to 40 °C under 9 T. Thus, transformation temperatures were decreased around 29 °C when 9 T was applied.
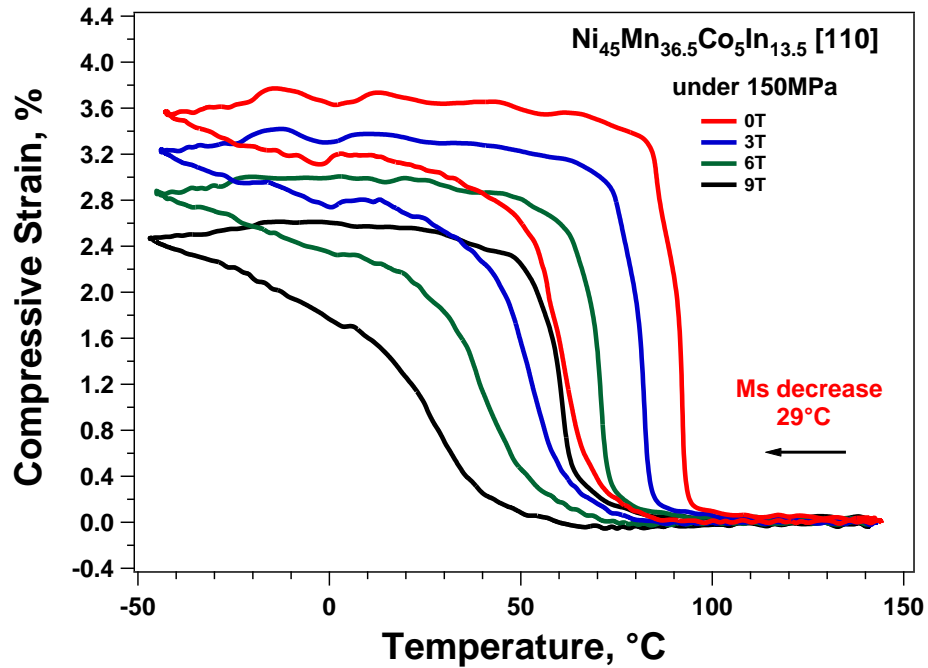
Figure 5.14 Thermal cycling response of NiMnCoIn single crystals along the [110] oriented specimen under stress and magnetic field.

5.11   Superelasticity and SME Under Magnetic Field in [111]-Orientation

Superelastic cycling was conducted at 90 °C under selected magnetic fields from 0 T to 9 T in [111] oriented NiMnCoIn single crystal, as shown in figure 5.15. The specimen was loaded until 1.5 % and then unloaded. Critical stress increased with applied magnetic field. Magnetostress of 106 MPa was obtained under 9 T in [111] oriented NiMnCoIn single crystalline.
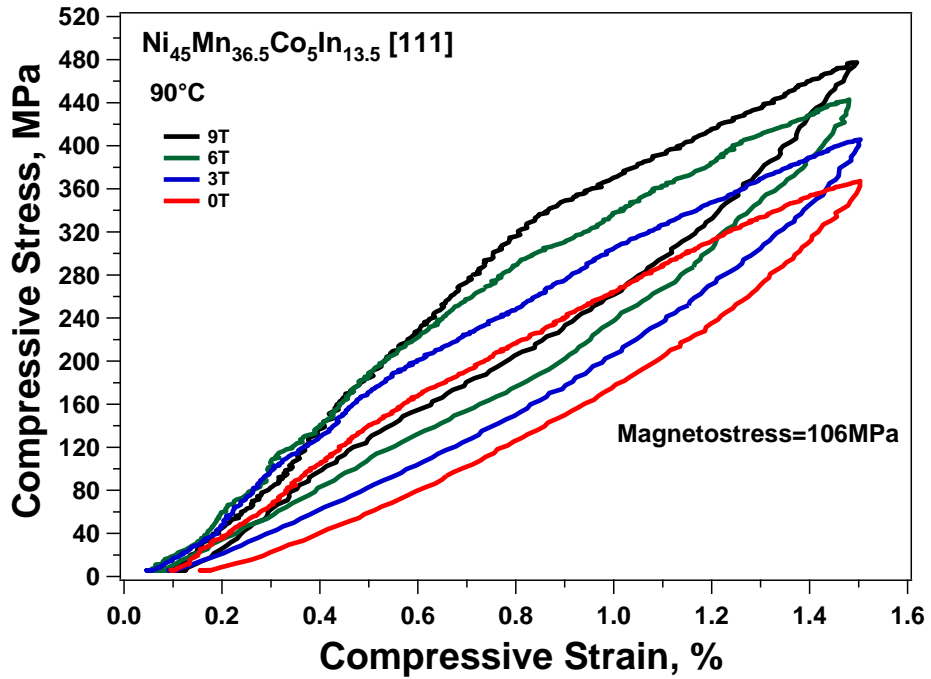
Figure 5.15 Superelastic cycling response of NiMnCoIn single crystals along the

[111] oriented specimen under selected magnetic fields.

Figure 5.16 exhibits thermal cycling of [111] oriented NiMnCoIn single crystal under 400 MPa and selected magnetic fields of 0 T and 9 T. Transformation strain was determined as 0.7 % under 400 MPa and decreased slightly with applied magnetic field due to incomplete martensitic transformation. Transformation temperatures decreased with applied magnetic field. M_s was 94 °C under 0 T which decreased to 79.2 °C under 9 T. Thus, transformation temperatures were decreased around 15 °C when 9 T was applied.
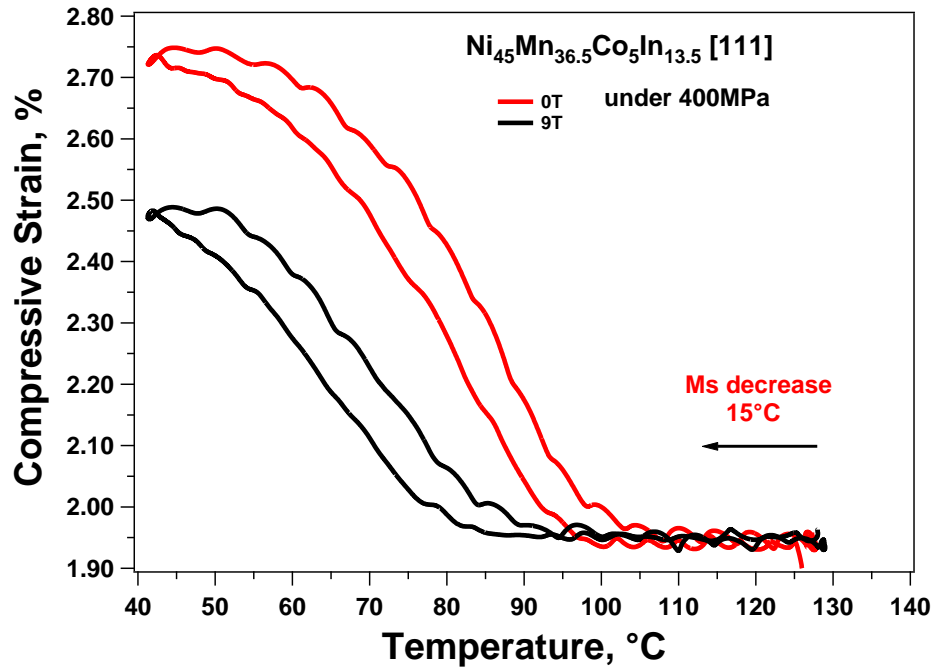
Figure 5.16 Superelastic cycling response of NiMnCoIn single crystals along the

[111] oriented specimen under selected magnetic fields.

Martensite start temperature as a function of applied stress from 100 MPa to 400 MPa, SME curve under 400 MPa was shown in figure 5.16), for 0 T and 9 T magnetic fields were plotted in figure 5.17. M_s increased linearly with stress and C-C slope of each magnetic field condition was almost same at around 46 MPa/°C. It should be note that C-C slope of [111] oriented NiMnCoIn single crystal is very high compared with [001] oriented specimens.
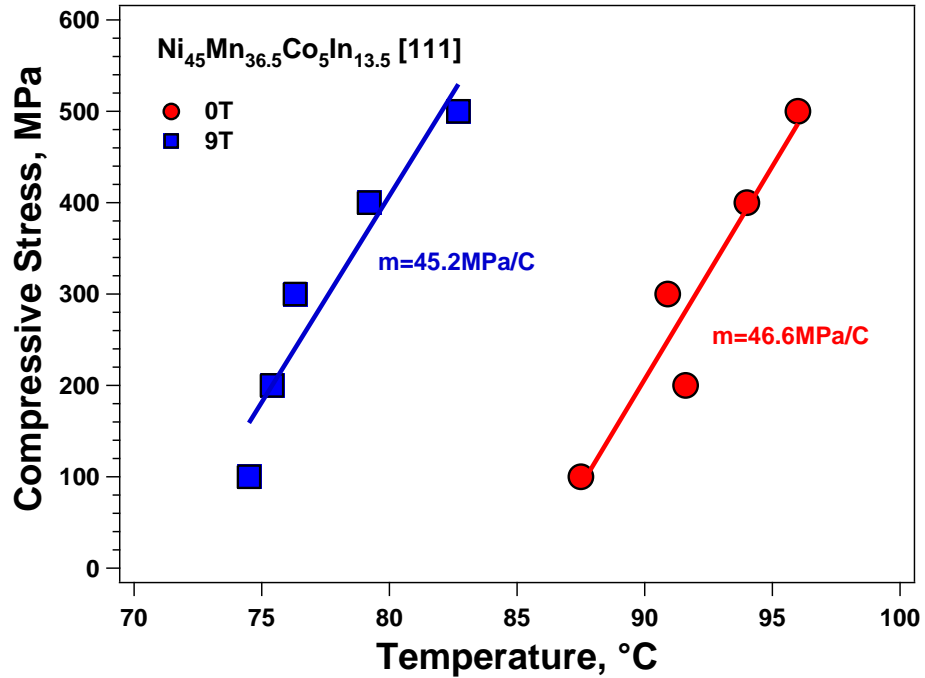
Figure 5.17 Ms as a function of applied stress in NiMnCoIn single crystals along

the [111] oriented specimen under selected magnetic fields.

Figure 5.18 shows the magnetostress as a function of magnetic field in NiMnCoIn single crystals along the [001], [110] and [111] orientations. Magnetostress values were collected from superelastic experiment of [001], [110] and [111] oriented specimens at 90 °C under magnetic field (Figure 5.5, figure 5.13 and figure 5.15). [110] orientation exhibited highest magnetostress of 160 MPa compared to 106 MPa in [111] and 85 MPa in [001] orientation at 90 °C under 9 T. Increment of 1 T magnetic field produced magnetostress of 17.6 MPa in [110], 11.6 MPa in [111] and 10.7 MPa in [001] orientations.
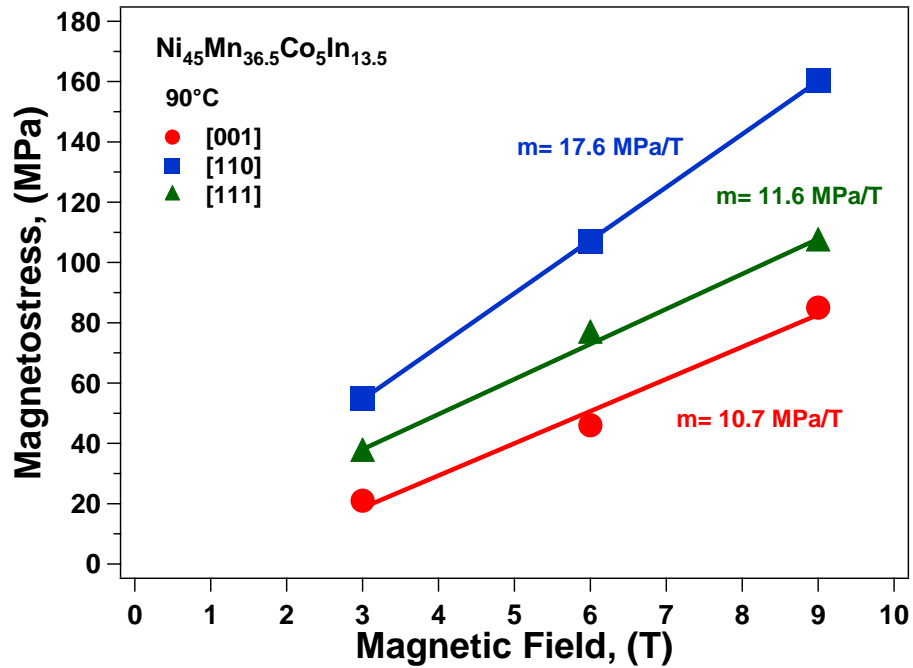
Figure 5.18 Magnetostress as a function of magnetic field in NiMnCoIn single

crystals along the [001], [110] and [111] orientations.

5.12   Conclusions

Effects of magnetic field on the magnetization and shape memory behavior on the

NiMnCoIn single crystalline along the [001], [110] and [111] orientations were studied in

this chapter. Results are summarized below:

1. Optical microscope results showed that second phase structure were created

    during the fabrication of NiMnCoIn single crystals. Chemical composition of

    matrix and second phase were determined by SEM and composition of the alloy

    was slightly different than as planned. M_s was found as 91.2 °C which is higher

    than literature due to second phase formation. Curie temperature of the alloy

    was 104.1 °C.

2. Magnetization behavior of transforming phases and transformation temperatures were measured. M_s decreased by 54 °C with applied magnetic field of 12 T by cause of ferromagnetic austenite. Kinetic arrest phenomena was observed under magnetic field of 3 T during cooling.

3. Perfect superelastic behavior of 2 % was observed at 90 °C under compression under selected magnetic fields and magnetostress of 85 MPa was observed under 9 T in [001] orientation. Furthermore, superelasticity experiments were conducted from 60 °C to 100 °C under magnetic fields of 0 T, 3 T, 6 T and 9 T to reveal the stress-temperature phase diagram under magnetic field. Effects of magnetic field on stress were decreased at 100 °C due to drastic magnetization drop at curie temperature.

4. Thermal cycling under stress and magnetic field experiments were performed and M_s decreased by an amount close to 21 °C with applied magnetic field of 9 T under 150 MPa in [001] orientation. The decrease of M_s was calculated theoretically and good agreement with experimental data. In addition, thermal cycling under magnetic field were conducted at selected stress levels from 50 MPa to 200 MPa and M_s as a function of stress phase diagram was created. TTs increased to above 100 °C under 200 MPa. From this, magnetic field was not effective on M_s at 200 MPa as a result of the curie temperature.

5. Orientation dependence on magnetostress and thermal cycling under stress and magnetic field were revealed in NiMnCoIn single crystalline along the [110] and [111] orientations. Huge magnetostress of 160 MPa was determined in [110] orientation where magnetostress of 106 MPa was obtained in [111]

orientation at 90 °C under magnetic field of 9 T. M_s decreased about 29 °C in [110] orientation under 150 MPa, and M_s decreased 15 °C with applied magnetic field of 9 T under 400 MPa. C-C slope of [111] orientation was 46.6 MPa/°C and almost same under 9 T.

6 Magnetic Field Effect on Shape Memory Behavior on NiMn-based Polycrystalline Metamagnetic Shape Memory Alloys

6.1 Introduction

In this chapter, effects of Co addition to polycrystalline NiMnGa alloys on their magnetic and shape memory properties were studied. Effects of composition on transformation temperatures were revealed by DSC experiment. Magnetization behavior of austenite and martensite in NiMnCoGa polycrystalline were determined. Effect of Co addition on the shape memory effect and superelastic behavior were investigated. In addition, two way shape memory behavior of NiMnGa and NiMnCoGa were determined. Magnetic field effects on the shape memory effect in NiMnCoGa were explored.

Magnetic Shape memory properties of $Mn_{49}Ni_{42}Sn_9$ and $Mn_{49}Ni_{39}Sn_9Fe_3$ polycrystalline alloys were also characterized under compressive stress. Transformation temperatures, magnetization behavior of transforming phases were characterized in MnNiSn and MnNiSnFe alloys. Thermal cycling under stress and stress cycling at constant temperature experiments were conducted to reveal shape memory effect and superelastic behavior. Furthermore, magnetic field effect on superelasticity was investigated.

6.2 DSC Results

6.2.1 NiMnCoGa Alloys

Figure 6.1 shows the DSC response of $Ni_{50-x}Co_xMn_{32}Ga_{18}$ (x=0,4,6,7,8) alloys. TTs were determined to be above 100°C which makes them qualify as high temperature SMAs. TTs slightly increased with Co addition, up to 6%, and then decreased. Peak thermal hysteresis was about 20°C for all the alloys and it is consistent with magnetization results.
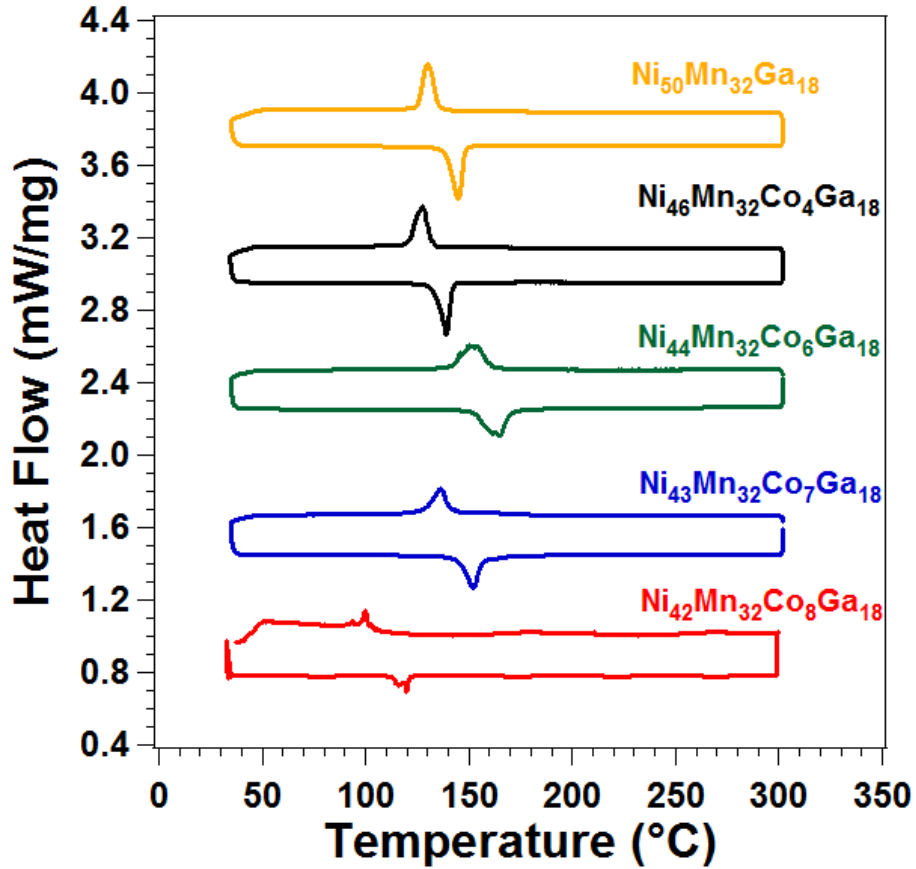
Figure 6.1 A comparison of DSC results showing the effect of Co doping on transformation temperatures of $Ni_{50-x}Co_xGa_{18}Mn_{32}$ (x=0,4,6,7,8) alloys

6.2.2 MnNiSn and MnNiSnFe Alloys

DSC responses of $Mn_{49}Ni_{42}Sn_9$ and $Mn_{49}Ni_{39}Sn_9Fe_3$ alloys are shown in figure 6.2. Austenite to martensite transformation was started at -6.4 °C and finished at -16.2 °C during cooling, while the back transformation was started at -6.1 °C and finished at 3.8 °C during heating for the $Mn_{49}Ni_{42}Sn_9$ alloy. Fe addition decreased the transformation temperatures where M_s, M_f, A_s and A_f were determined as -10.9 °C, -36 °C, -22.8 °C and 0.3 °C, respectively.
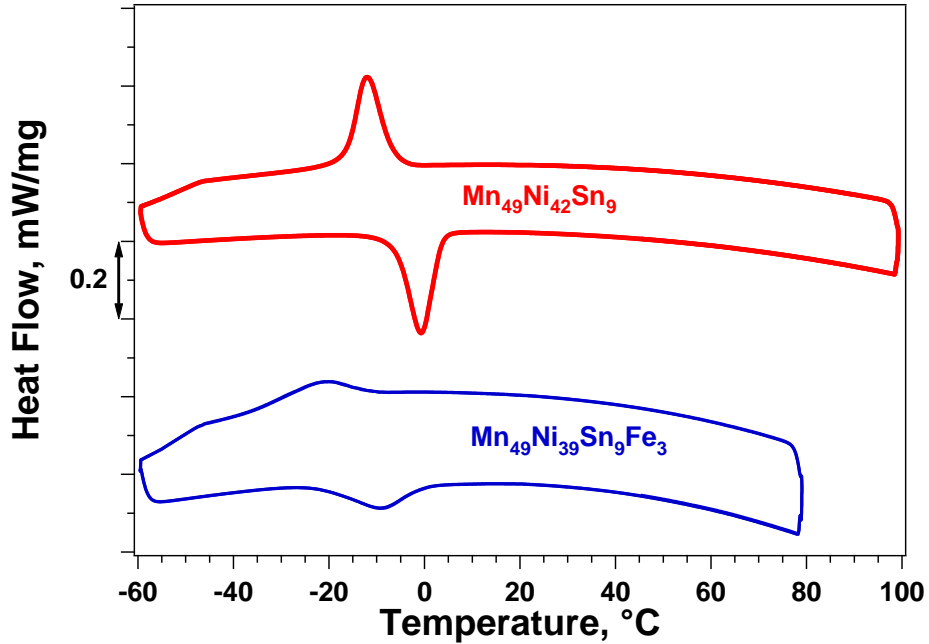
Figure 6.2 DSC responses of $Mn_{49}Ni_{42}Sn_9$ and $Mn_{49}Ni_{39}Sn_9Fe_3$ polycrystalline

alloys

6.3 Magnetic Measurements

6.3.1 NiMnCoGa Alloys

Figure 6.3 shows the magnetization response of $Ni_{42}Co_8Mn_{32}Ga_{18}$ alloy as a function of temperature. The sample was cooled down to 5 K under zero magnetic field and 0.1 Tesla was applied, then it was heated up to 400 K and cooled down to 5 K under 0.1 Tesla. During heating, ferromagnetic martensite became paramagnetic above 300 K, and transformed to ferromagnetic austenite above 380 K. Upon cooling, ferromagnetic austenite transformed to paramagnetic martensite initially, and then followed a magnetic transition where martensite became ferromagnetic. No thermal hysteresis was observed during magnetic transition in martensite phase while the first order austenite to martensite phase transformation was associated with a thermal hysteresis of about 20 K. When the

87

sample was heated from 5 K to 400 K under 5 Tesla, its magnetization increased and martensite to austenite TT decreased by 19 K compared to that under 0.1 Tesla.

Shift of TTs to lower temperature with applied field was a characteristic behavior observed in meta-magnetic SMAs and termed as austenite stabilization [12]. Reversible field-induced phase transformation became possible if TTs decreased to a level where the martensite finish temperature under zero field was higher than the austenite finish temperature under applied field. In general, thermal hysteresis does not change considerably with applied field. Thus, the critical field for reversible field induced phase transformation decreased with hysteresis. It has been found that (not shown in Figure 6.1) Curie temperature of martensite, T_{CM}, of $Ni_{50-x}Co_xMn_{32}Ga_{18}$ alloys decreased with increase in Co content from 315 K to 290 K for x=0 and x=8, respectively.

When martensite is ferromagnetic, field-induced strain can be obtained by variant reorientation, provided detwinning stress is low and the magnetocrystalline anisotropy energy is high. When the alloy is meta-magnetic, field-induced strain can be obtained through phase transformation. Therefore, in NiCoMnGa alloys, while field-induced strain might be obtained through variant reorientation at lower temperatures, it could be realized by phase transformation at higher temperatures.
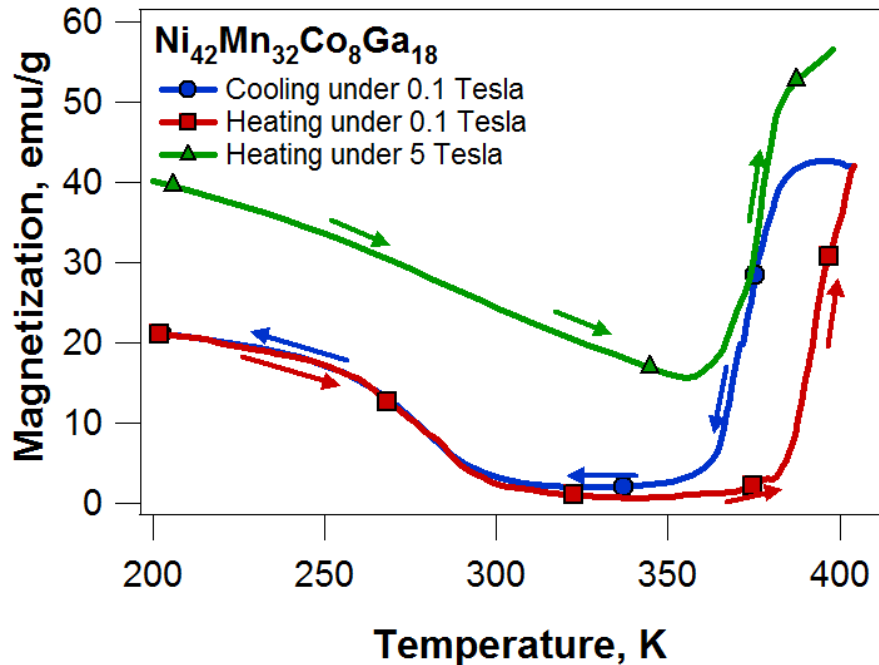
Figure 6.3 Magnetization response of $Ni_{42}Co_8Ga_{18}Mn_{32}$ alloy as a function of temperature under 0.1 and 5 Tesla fields.

6.3.2 MnNiSn and MnNiSnFe Alloys

The change of magnetization with temperature of $Mn_{49}Ni_{42}Sn_9$ and $Mn_{49}Ni_{39}Sn_9Fe_3$ alloys under various magnetic field from 0.005 T to 12 T, are shown in figure 6.4a and 6.4b, respectively. The transformation temperatures from ferromagnetic austenite to weakly magnetic martensite phase decreased with increased magnetic field. Difference between the saturated magnetization of austenite and martensite phases was around 15 emu g^{-1} under 5 T in $Mn_{49}Ni_{42}Sn_9$ while it was 40 emu g^{-1} in $Mn_{49}Ni_{39}Sn_9Fe_3$. It is clear that Fe addition increased the magnetization difference significantly. M_s, M_f, A_s, A_f of $Mn_{49}Ni_{42}Sn_9$ were determined as 323 K, 310 K, 319 K, 332 K under 5 T. Fe addition decreased the transition temperatures to M_s=257 K, M_f=243 K, A_s=256 K, A_f=269 K under 5 T in $Mn_{49}Ni_{39}Sn_9Fe_3$. Increasing magnetic field level also shifted transformation

temperatures to lower temperatures as 246 K, 230 K, 247 K, 260 K under 12 T. Decrease of transition temperatures with Fe addition was in good agreement with DSC results. The thermal hysteresis of the alloys are very small which is promising for magnetic field induced strain experiments.
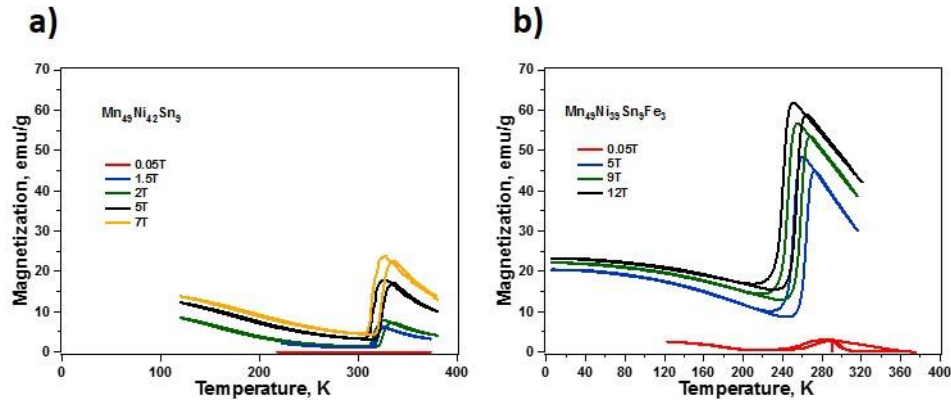
Figure 6.4 Magnetization vs. temperature response of a) $Mn_{49}Ni_{42}Sn_9$ and b) $Mn_{49}Ni_{39}Sn_9Fe_3$ polycrystalline alloys under selected magnetic fields

6.4 Thermal Cycling Under Constant External Stress

6.4.1 NiMnCoGa Alloys

Figures 6.5a and 6.5b demonstrate the isobaric thermal cycling response of $Ni_{50}Ga_{18}Mn_{32}$ (Co-free) and $Ni_{44}Co_6Ga_{18}Mn_{32}$ (Co-doped) alloys, respectively, as a function of applied stress. The samples were loaded to selected stress levels (increased incrementally up to 200 MPa) above their A_f, and thermally cycled between a temperature below M_f and a temperature above A_f. At the end of the cycle, applied stress is increased to the next level and thermal cycling is repeated.

As temperature decreases, certain martensite variants grow along the applied stress increasing the detected strain. Upon heating, they transform back to austenite. It is clear

that the transformation occurs above 100 °C which is in good agreement with DSC results. Compressive strain increased initially due to the increased volume fraction of oriented variants and then saturates with stress. Temperature hysteresis shows a similar trend to the transformation strain. Temperature hysteresis of $Ni_{50}Ga_{18}Mn_{32}$ is determined to be 19°C under 50 MPa, which is consistent with DSC and SQUID results. Temperature hysteresis increases from 19 °C to 32 °C as the applied stress increases from 15 MPa to 200 MPa. The transformation strain is 1.2 % and 1.7 % under 50 MPa and 2.4 % and 2.9 % under 200 MPa for the $Ni_{50}Ga_{18}Mn_{32}$ and $Ni_{44}Co_6Ga_{18}Mn_{32}$ alloys, respectively.

Irrecoverable strain increases with stress as a result of more pronounced generation of defects and dislocations at higher stress levels. The Co-free specimen showed full recovery up to 100 MPa, however, Co-doped specimen displayed a monotonously increasing trend in irrecoverable strain with increasing applied stress starting at 50 MPa. The amount of plastic strain Co-doped specimen increased from 0.35% to 0.8% when applied stress is increased from 50 MPa to 200 MPa. This tendency might be caused by the ductile gamma phase occurrence through Co addition which was reported to hamper reorientation or detwinning of the martensite variants, as well as promote defect generation such as dislocations [110]. Formation of second phases might also be responsible for the change of the shape of cooling curves as the transformation progresses. Whilst the Co-doped alloy demonstrates a smoother and more symmetrical transition, the Co-free specimen displays a sharper curve (almost like a corner) indicating a faster (burst type) transition. A smoother curve might be attributed to the increased elastic energy stored in the material due to the interaction of phase front with second phase or particles.
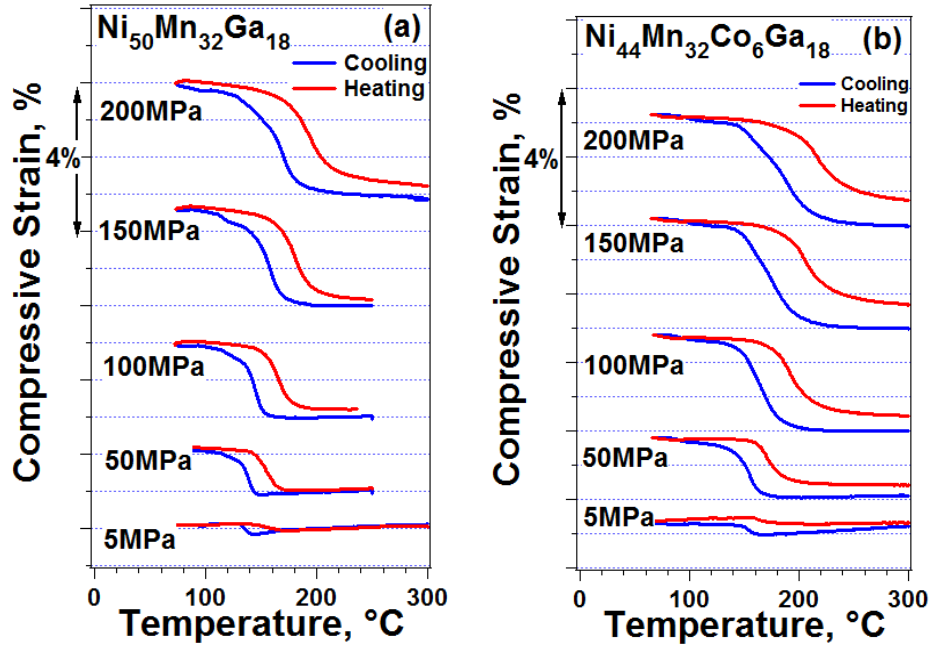
Figure 6.5 Shape memory behavior of a) $Ni_{50}Ga_{18}Mn_{32}$ and b) $Ni_{44}Co_6Ga_{18}Mn_{32}$ alloys under compression

6.4.2 MnNiSn and MnNiSnFe Alloys

Figure 6.6 shows the thermal cycling under selected constant compressive stress responses of $Mn_{49}Ni_{42}Sn_9$ and $Mn_{49}Ni_{39}Sn_9Fe_3$ alloys. In parent phase, compressive stress was applied isothermally and then the specimen was cooled down to below M_f and heated up to above A_f to under constant stress. Thermal cycling was repeated under selected stress levels from 5 MPa to 250 MPa.. M_s, M_f, A_s, A_f of $Mn_{49}Ni_{42}Sn_9$ were determined as -3 °C, -13.8 °C, -10.4 °C, 0.9 °C, respectively under 5 MPa, and they shift to higher temperatures of 41.2 °C, 12.9 °C, 29.5 °C, 56 °C under 250 MPa. Fe addition decreased the transition temperatures to M_s=-7 °C, M_f=-26 °C, A_s=-15.4 °C, A_f=2.3 °C under 5 MPa in $Mn_{49}Ni_{39}Sn_9Fe_3$. It should be note that thermal cycling under each selected stresses were fully reversible and irrecoverable strain was not observed even under 250 MPa for both compositions.
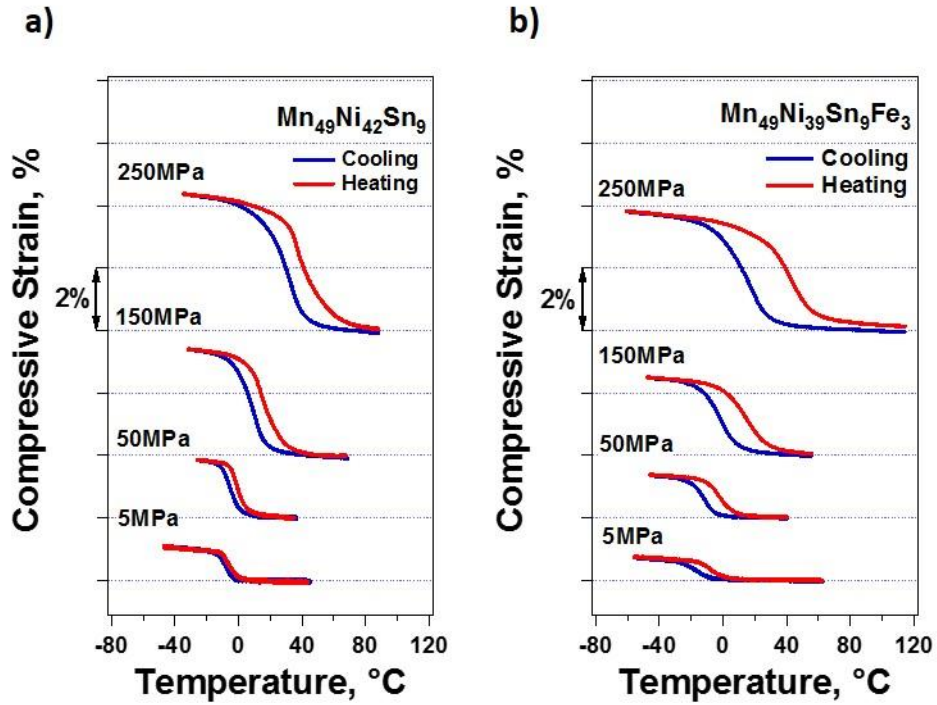
Figure 6.6 Thermal cycling under constant compressive stress response a)

$Mn_{49}Ni_{42}Sn_9$ and b) $Mn_{49}Ni_{39}Sn_9Fe_3$ polycrystalline alloys

Figure 6.7 shows transformation strain, irrecoverable strain and thermal hysteresis with respect to applied compressive stress were determined from heating and cooling under constant experiments (Figure 6.6). Transformation strain was initially increased and then saturated as with applied stress for both alloys. Maximum transformation strain was 3.8 % under 225 MPa for $Mn_{49}Ni_{42}Sn_9$ and 3.2 % under 250 MPa for $Mn_{49}Ni_{39}Sn_9Fe_3$. In addition, thermal hysteresis of $Mn_{49}Ni_{42}Sn_9$ and $Mn_{49}Ni_{39}Sn_9Fe_3$ alloys under 250 MPa were 10 °C and 28 °C, respectively. As a result, $Mn_{49}Ni_{42}Sn_9$ alloy exhibited higher transformation strain and lower thermal hysteresis compared with $Mn_{49}Ni_{39}Sn_9Fe_3$ alloy. It is worth the mention that low transformation hysteresis yields to lower critical magnetic field requirement for magnetic field induced phase transformation, which can broaden its practical uses.
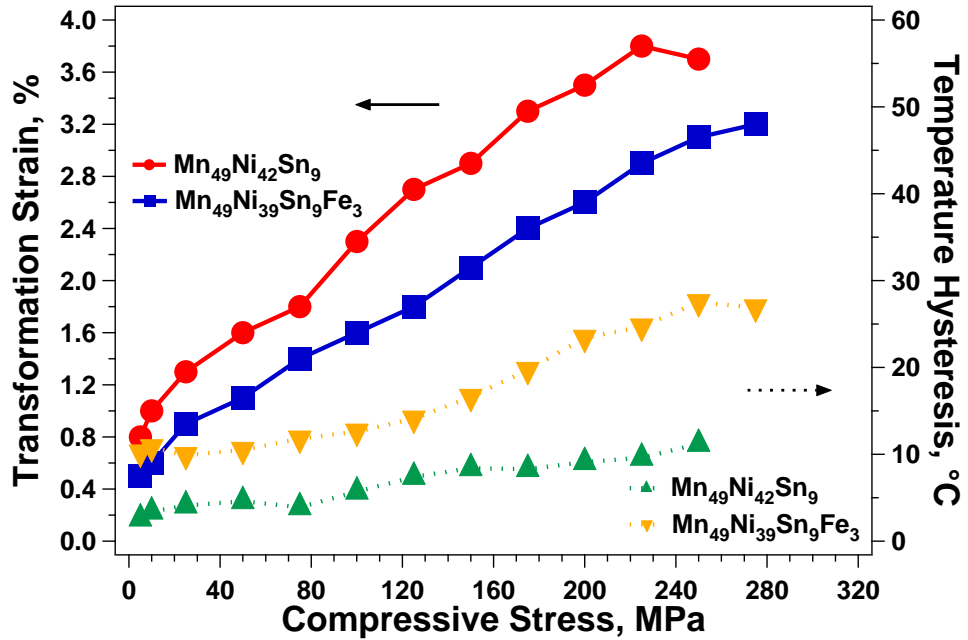
Figure 6.7 Transformation strain and temperature hysteresis change as a function of applied compressive stress in $Mn_{49}Ni_{42}Sn_9$ and $Mn_{49}Ni_{39}Sn_9Fe_3$ polycrystalline alloys

Figure 6.8 presents the change of M_s with applied compressive stress, extracted from figure 6.6. The C-C slopes of the $Mn_{49}Ni_{42}Sn_9$ and $Mn_{49}Ni_{39}Sn_9Fe_3$ alloys were found be very close; 5.6 MPa/°C and 5.9 MPa/°C, respectively. The C-C slope of [001] oriented $Ni_{51.1}Mn_{24}Ga_{24.9}$ and $Ni_{45}Mn_{36.5}Co_5In_{13.5}$ single crystalline was reported as 2.1 MPa/°C under compression [11, 12]. In addition, the slope of C-C curve as 4.2 MPa/°C, 2.1 MPa/°C for $CoNi_{34.5}Al_{28.3}$ and $Ni_{54}Fe_{19}Ga_{27}$ in polycrystalline form under compression, respectively [111, 112].
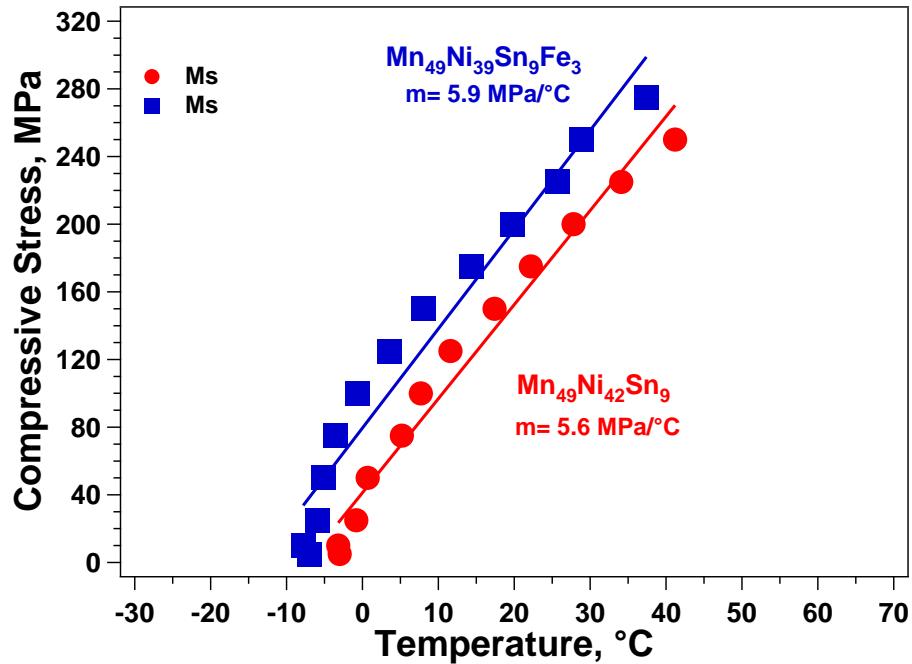
Figure 6.8 Applied constant compressive stress versus martensite start

temperature phase diagram of $Mn_{49}Ni_{42}Sn_9$ and $Mn_{49}Ni_{39}Sn_9Fe_3$ polycrystalline alloys

6.5   Isothermal Stress Cycling

6.5.1   NiMnCoGa Alloys

Figure 6.9 shows the superelastic behavior of Co-free and Co-doped specimens

above their A_f. Upon loading austenite transforms to martensite and martensite transforms

back to austenite during unloading. Near perfect superelasticity is observed with a total

strain of 3 % at 170 °C and 180 °C for Co-free and 3.5 % at 180 °C and 200 °C for Co-

doped samples. As evident by the fact that at the end of loading, the level of applied stress

reaches a maximum of 290 MPa, this alloy possesses fair strength for fracture.
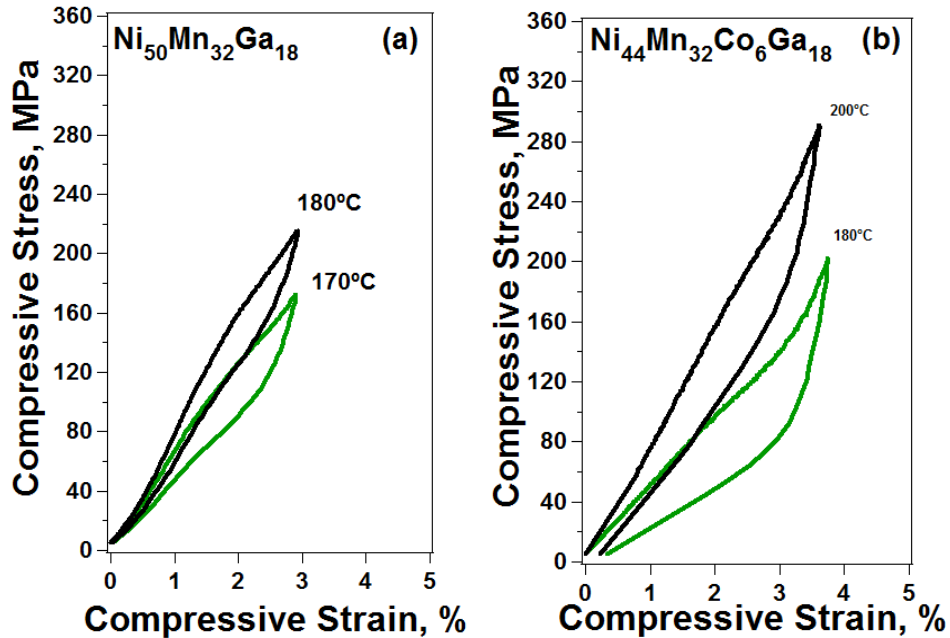
Figure 6.9 Superelasticity behavior of a) $Ni_{50}Ga_{18}Mn_{32}$ and b) $Ni_{44}Co_6Ga_{18}Mn_{32}$

(at%) alloys

6.5.2 MnNiSn and MnNiSnFe Alloys

Isothermal stress cycling experiments were performed at selected temperatures from 5 °C to 45 °C in order to observe superelastic response of $Mn_{49}Ni_{42}Sn_9$ and $Mn_{49}Ni_{39}Sn_9Fe_3$ alloys, as shown in Figure 6.10. Perfect superelasticity with recoverable strain of 4 % in $Mn_{49}Ni_{42}Sn_9$ and 3.5 % in $Mn_{49}Ni_{39}Sn_9Fe_3$ alloys were observed. The author strongly indicates that MnNiSn and MnNiSnFe alloys in polycrystalline form were presented promising mechanical experiment results to overcome general brittleness problem of magnetic shape memory alloys. In addition, critical stress for martensitic transformation increased with temperature. The result showed that mechanical hysteresis was lower in $Mn_{49}Ni_{42}Sn_9$ than $Mn_{49}Ni_{39}Sn_9Fe_3$ alloy which is similar behavior of temperature hysteresis in thermal cycling under stress experiment.
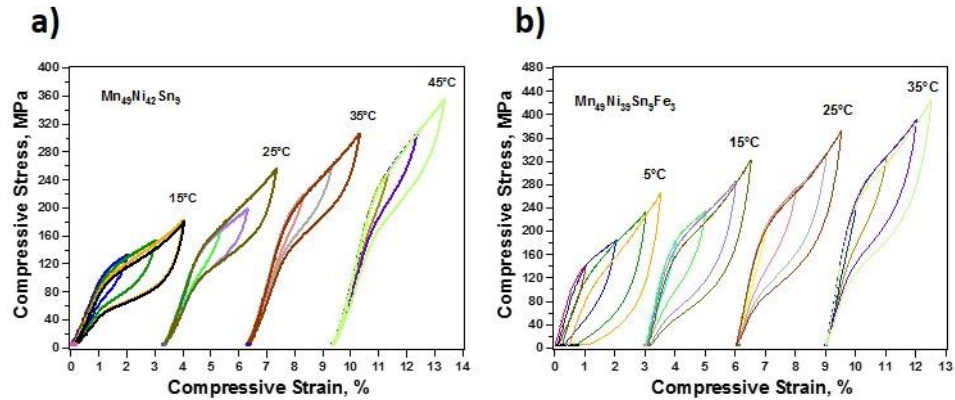
Figure 6.10 Superelastic response of a) $Mn_{49}Ni_{42}Sn_9$ and b) $Mn_{49}Ni_{39}Sn_9Fe_3$

polycrystalline alloys

6.6   Two Way Shape Memory Effect in NiMnCoGa Alloys

Figure 6.11 shows the two way shape memory effect (TWSME) in Co-doped and

Co-free alloys. The samples were cooled down before (untrained) and after (trained) the

tests shown in Figures 6.9 and 6.11 under 5 MPa. 5 MPa is applied to keep the grips in

contact wth the specimen for strain measurements. It is clear that after training both alloys

demonstrated more than 3 % transformation strain upon cooling while it was about 0.2 %

before training. The high transformation strain upon training indicates that internal stress

fields to select certain martensite variants upon transformation are formed upon training.

This is a very useful tool to oberve strain during field-induced phase trasformations. Since

martensite is non magnetic, there is no driving force for the selection of variants during

field-induced phase transformation. However, if the material can be trained then austenite

will transform to martensite with selected variants that will result in macroscopic strain.
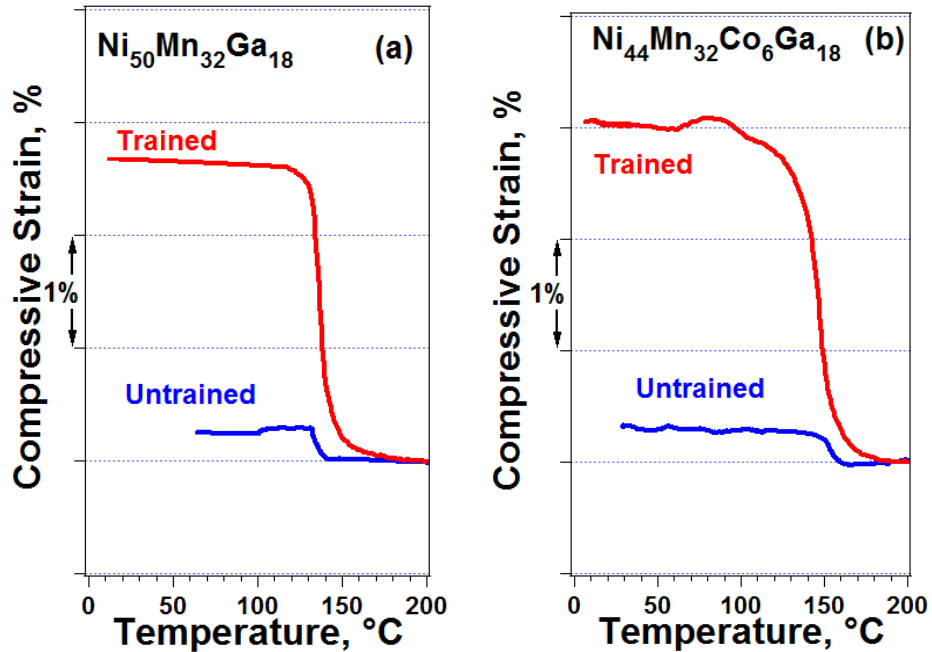
Figure 6.11 TWSME behavior under 5 MPa of a) $Ni_{50}Ga_{18}Mn_{32}$ and b) $Ni_{44}Co_6Ga_{18}Mn_{32}$ alloys in untrained and trained conditions.

6.7 Thermal Cycling Under External Stress and Magnetic Field in NiMnCoGa Alloys

In order to determine the effects of magnetic field on the shape memory effect in $Ni_{46}Co_4Ga_{19}Mn_{31}$ polycrystalline shape memory alloy, thermal cycling was conducted under 50 MPa under selected magnetic fields of 0 T and 9 T, as shown in Figure 6.12. Transformation strain under 150 MPa was determined to be about 4 %, and decreased slightly with applied magnetic field due to irrecoverable strain. It is clear that transformation temperatures shifted to lower temperatures with magnetic field. M_s was 122 °C under 0 T which decreased to 117 °C under 9 T. Thus, transformation temperatures were decreased by 5 °C when 9 T was applied.
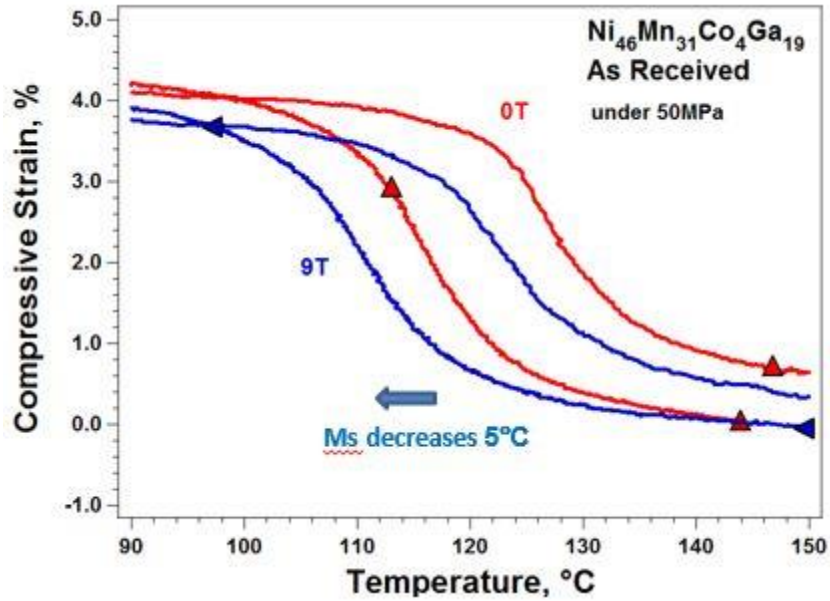
Figure 6.12 Thermal cycling under 50 MPa and at selected magnetic fields of

$Ni_{46}Co_4Ga_{19}Mn_{31}$ alloys

6.8 Superelasticity Under Magnetic Field in MnNiSn and MnNiSnFe Alloys

Magnetic field effects on the superelastic response of $Mn_{49}Ni_{42}Sn_9$ and $Mn_{49}Ni_{39}Sn_9Fe_3$ alloys were shown in Figure 6.13. The samples were loaded, up to a total strain of 3.5 %, and then unloaded at room temperature under 0 and 9 Tesla. It can be seen that applied magnetic field shifts the superelastic loops to higher stress levels. In other words, applied magnetic field stabilizes austenite and make it harder to transform to martensite. The change of the stress with magnetic field, which is called magnetostress in metamagnetic shape memory alloys, was measured at the strain level of 2.5 %. Magnetostress values of $Mn_{49}Ni_{42}Sn_9$ and $Mn_{49}Ni_{39}Sn_9Fe_3$ were determined to be 21 MPa and 27 MPa, respectively. It should be noted that, Zeeman energy was higher in $Mn_{49}Ni_{39}Sn_9Fe_3$ (see Figure 6.4) since Fe addition increased the magnetization difference

between the transforming phases drastically. Therefore, magnetostress of $Mn_{49}Ni_{39}Sn_9Fe_3$ alloy was higher than the magnetostress of $Mn_{49}Ni_{42}Sn_9$.
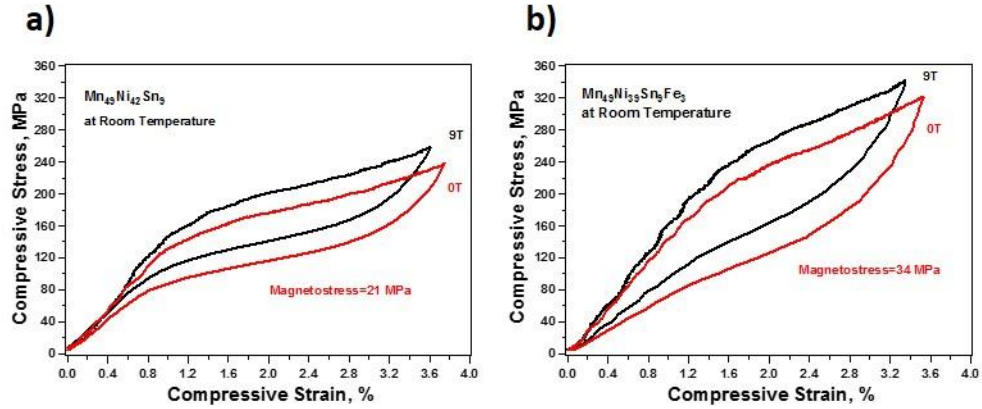
Figure 6.13 Superelastic response under magnetic field a) $Mn_{49}Ni_{42}Sn_9$ and b) $Mn_{49}Ni_{39}Sn_9Fe_3$ polycrystalline alloys

6.9   Conclusion

Effect of Co addition as a quaternary element on shape memory behavior and magnetic properties in NiMnGa polycrystalline and effect of Fe addition in MnNiSn polycrystalline were investigated in this chapter. Important points are summarized below:

1. Transformation temperatures of NiMnCoGa alloys were obtained above 100 °C, so these alloys can be qualified as high temperature shape memory alloys. TTs were slightly increased with Co addition, up to 6 %, and decreased. Temperature hysteresis was found around 20 °C.

2. Magnetization measurement showed that NiCoMnGa alloys can be utilized as meta-magnetic shape memory alloys in their polycrystalline form due to phase transformation from ferromagnetic parent phase to paramagnetic martensite.

3. NiCoMnGa alloys demonstrated good shape memory behavior under stress levels up to 200 MPa in polycrystalline form and can also be classified as high temperature SMAs with perfect superelasticity of 3.5 % above 150 °C.

4. NiMnCoGa can also be trained easily to show good TWSME of 3 % that would result in high strain upon field-induced transformations.

5. Applying magnetic field of 9 T decreased transformation temperatures 5 °C under 50 MPa for poly-crystalline of NiMnCoGa alloys. Polycrystalline of NiMnCoGa can be used as a High temperature magnetic actuator.

Shape memory and pseudoelastic behaviors of $Mn_{49}Ni_{42}Sn_9$ and $Mn_{49}Ni_{39}Sn_9Fe_3$ metamagnetic shape memory alloys were investigated under compressive stress and magnetic field. Results can be summarized:

1. Fe addition on MnNiSn decreased the transformation temperatures and increase magnetization difference between austenite and martensite.

2. Thermal cycling under constant compressive stress and pseudoelastic response showed that $Mn_{49}Ni_{42}Sn_9$ and $Mn_{49}Ni_{39}Sn_9Fe_3$ alloys exhibited fully recoverable transformation strain around 4 % and 3.5 %, respectively. Thermal hysteresis of $Mn_{49}Ni_{42}Sn_9$ and $Mn_{49}Ni_{39}Sn_9Fe_3$ alloys under 250 MPa were 10 °C and 28 °C, respectively. Temperature and mechanical hysteresis of $Mn_{49}Ni_{42}Sn_9$ was lower than $Mn_{49}Ni_{39}Sn_9Fe_3$ alloy.

3. C-C slope of $Mn_{49}Ni_{42}Sn_9$ and $Mn_{49}Ni_{39}Sn_9Fe_3$ was determined around 5.6 MPa/°C and 5.9 MPa/°C, respectively.

4. Superelasticity tests under compressive stress and magnetic field were performed at room temperature, and magnetostress of $Mn_{49}Ni_{42}Sn_9$ and $Mn_{49}Ni_{39}Sn_9Fe_3$ was around 21 MPa and 27 MPa, respectively.

7 Characterization of FeNiCoAlNb Shape Memory Alloy with Ultra Large Transformation Strain

7.1 Introduction

The shape memory properties of a ferrous single crystalline alloy, FeNiCoAlNb, are investigated along the [100] orientation by thermal cycling under constant stress and superelasticity tests in both tension and compression in this chapter. XRD and TEM studies were conducted to obtain crystal structure of transforming phases, precipitation characteristics and lattice parameters. Superelasticity at various temperatures were tested under tension and compression to determine the phase diagram. Thermal cycling under compressive stress were conducted to reveal shape memory effect. The specimen was loaded until failure to determine its ductility and strength. Moreover, magnetization behavior of austenite and martensite phases were investigated. Lastly, effects of magnetic field effect on the superelasticity was revealed.

7.2 XRD and TEM Results

Figure 7.1 shows the XRD response of solutionized FeNiCoAlNb single crystals. The single crystal was found to be austenite (γ, FCC) at room temperature. Shape memory behavior was not observed in solutionized FeNiCoAlNb single crystals upon DSC and mechanical tests. It is well known that in FeSMAs, precipitation is a requirement to observe thermoelastic martensitic transformation. FeSMAs without aging exhibit non-thermoelastic forward transformation from high-temperature face-centered cubic (fcc) γ phase to α martensite phase which is either body-centered cubic (bcc) or body centered tetragonal (bct) crystal structure. After the precipitation, thermoelastic martensitic transformation γ / α' (bct) occurs with the precipitation of γ′phase with L1$_2$. Precipitation

formation alters the strength of parent phase, tetragonality of martensite and decrease the thermal hysteresis [47].
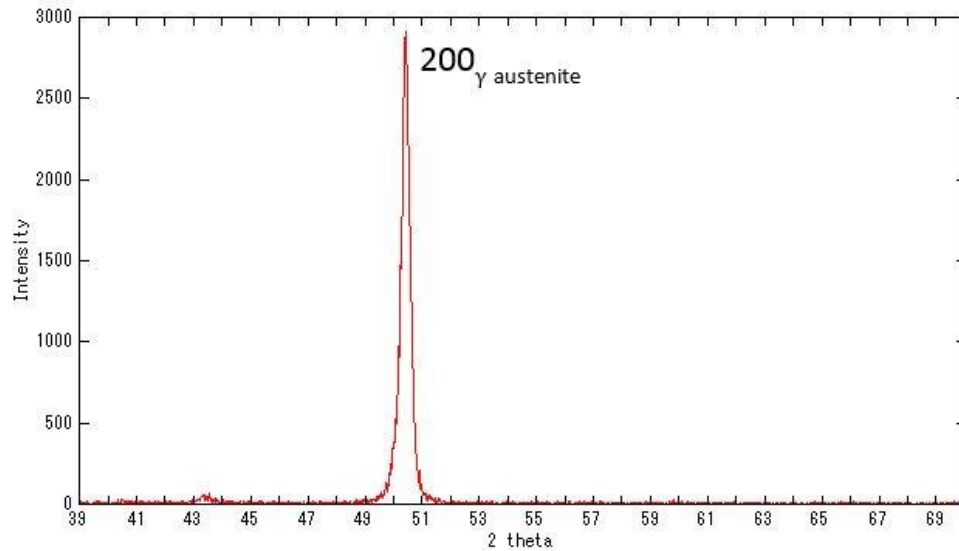
Figure 7.1 The XRD response of solutionized FeNiCoAlNb single crystal at room temperature

In order to observe shape memory behavior, the samples were aged at selected conditions to form coherent precipitates. Figure 7.2 shows the dark field TEM image and the corresponding diffraction pattern taken from the circled diffraction spot of 700C-3h aged FeNiCoAlNb single crystal. It is found that after 700C-3h aging, the alloy is austenite (γ, FCC) at room temperature and precipitates (γ', $L1_2$) of approximately 5 nm in diameter are formed in the matrix. The DSC tests confirmed that no transformation is observed in aged samples when they are cooled down to -150°C. Thus, even after aging, the transformation temperatures are still very low.
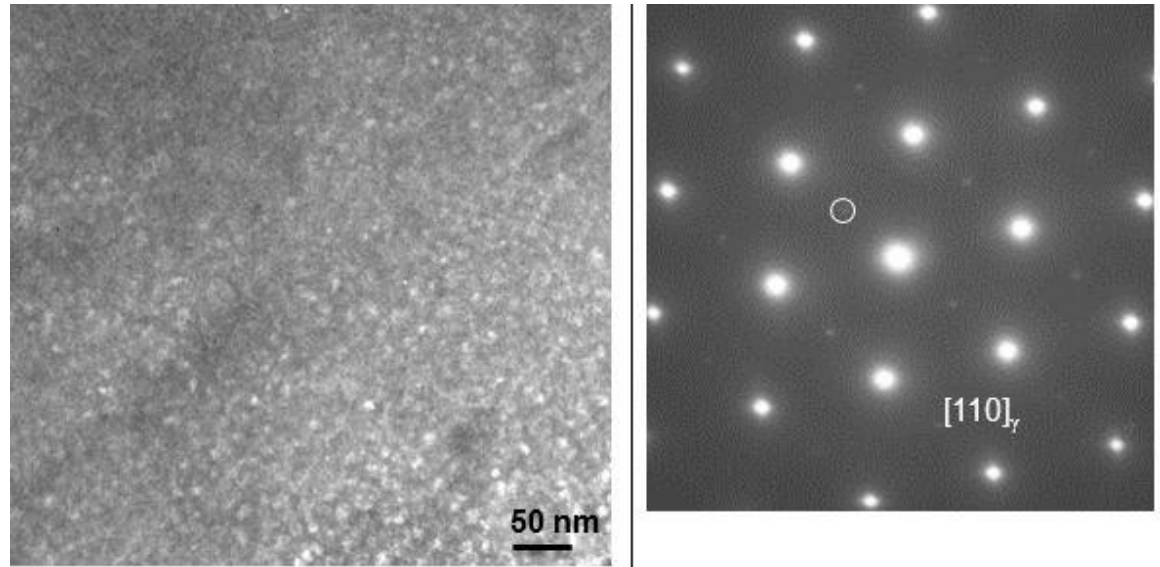
Figure 7.2 The dark field TEM image and the corresponding diffraction pattern taken from the circled diffraction spot of 700C-3h aged FeNiCoAlNb single crystal.

In order to observe martensite at TEM and XRD, [001]-oriented FeNiCoAlNb single crystal was compressed until 8% (stress induced phase transformation was observed) and then unloaded at room temperature where the mechanical response is shown in Figure 7.3a. Fig 7.3b shows the dark field TEM image and the corresponding diffraction pattern from the [110] zone axis of 700C-3h aged and deformed single crystal. The precipitates improve the strength of the matrix and results in thermoelastic martensitic transformation in this alloy. When the images are analyzed, it was found that austenite, martensite (α', BCT) and nanosize precipitates (γ') are available in the microstructure. The lattice parameters of γ and α' phases are determined as a_0=0.3625nm, a=0.2761 nm and c=0.3047nm at room temperature. Figure 7.3c shows the XRD response of deformed single crystal which confirms the formation of martensite.
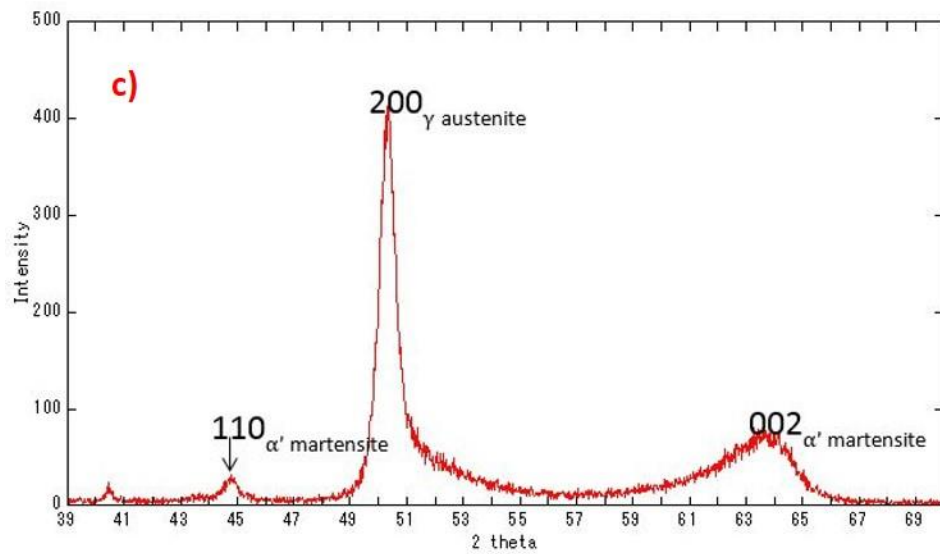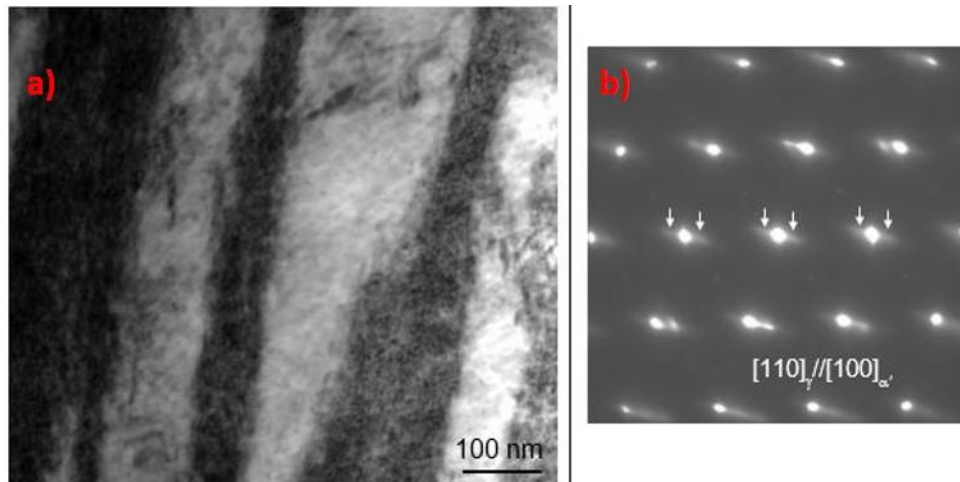
Figure 7.3 a) The compressive response of 700C-3h aged FeNiCoAlNb single crystal along the [001] orientation at room temperature. b) The dark field TEM image and the corresponding diffraction pattern from the [110] zone axis and c) XRD response of deformed single crystal at room temperature.

7.3 Magnetic Measurements

Thermomagnetization response of [100] oriented FeCoNiAlNb alloy were revealed under 1 T and 9 T magnetic field, as shown in figure 7.4. Martensite phase exhibited higher magnetization compared to parent phase, and both phases are ferromagnetic
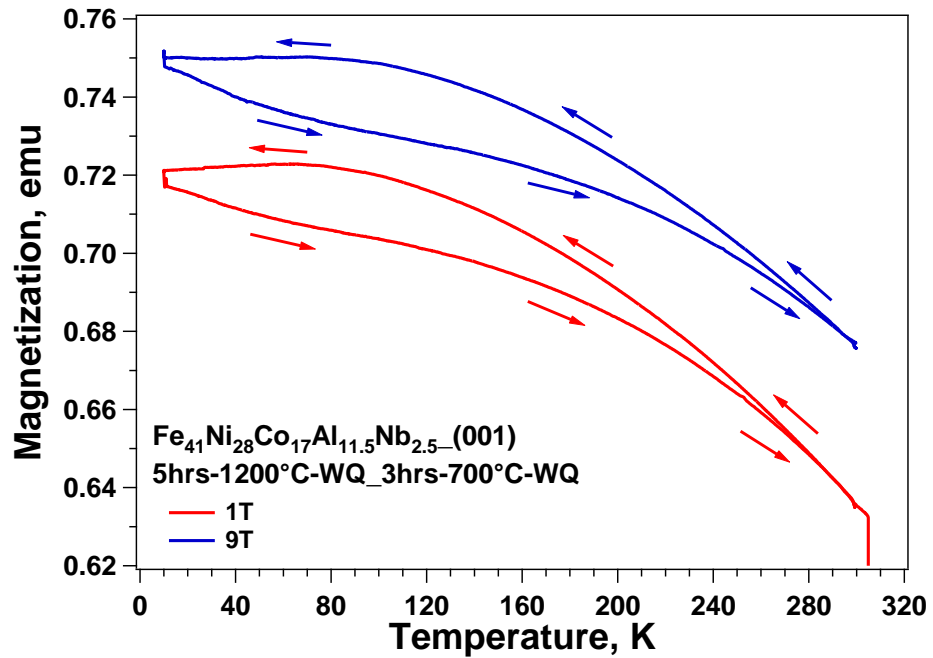
Figure 7.4 Magnetization curve of [100] oriented FeCoNiAlNb alloy under 1 T

and 9 T magnetic field

7.4 Mechanical Characterization

7.4.1 Isothermal Stress Cycling under Compression

Figure 7.5a shows compressive responses of [001]-oriented FeNiCoAlNb single crystal after aging at 700 °C for 30 minutes. Superelasticity under compression experiment was conducted at -100 ˚C, and reversible superelastic strain of about 14 % is observed. It is clear that in compression stress hysteresis increases with compressive strain. When the sample is loaded until 16 %, it did not recover back after unloading, due to large stress

hysteresis and an unrecovered strain of 12 % was observed. However, the compressive strain of 10 % was recovered upon heating, as shown in figure 7.5b. The transformation strain of 14 % in compression is the maximum recoverable strain ever observed in FeNiCo-based SMAs.
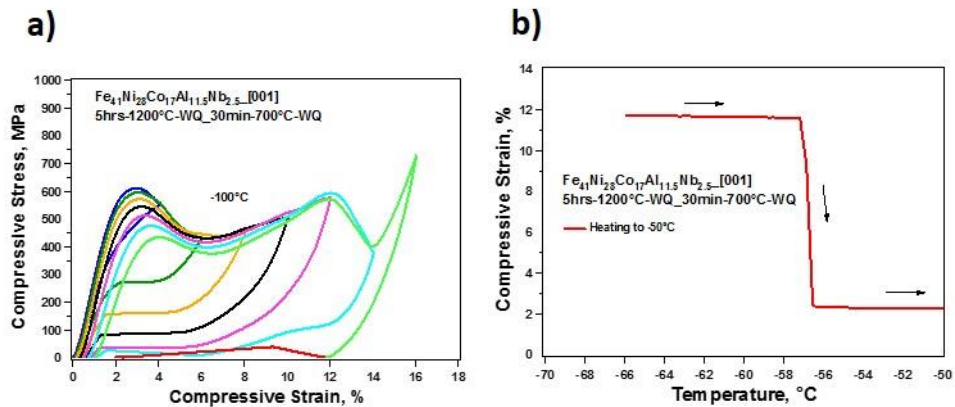
Figure 7.5 a) Compressive responses of [001]-oriented FeNiCoAlNb single crystal after aging at 700 °C for 30 minutes, b) Heat induced shape recovery of retained martensite during back transformation after the deformation in figure 7.5b

Figure 7.6a shows the compressive response at -130 °C of [001]-oriented FeNiCoAlNb after 700 °C-3h aging. The response is similar to the one observed after 700 °C-30min aging where almost perfect superelasticity is observed initially. Further loading resulted in substantial increase in hysteresis and irrecoverable strain upon unloading. When the sample is loaded until 11 %, there is a retained strain of 6.5 % which is recovered upon heating as shown by figure 7.6b. From this, it can be seen that the irrecoverable strain upon unloading can be attributed to retained martensite. It should be noted that there is a drop in stress during loading at a compressive strain of about 8.5 %. The reasons for this load drop will be discussed in the next section.
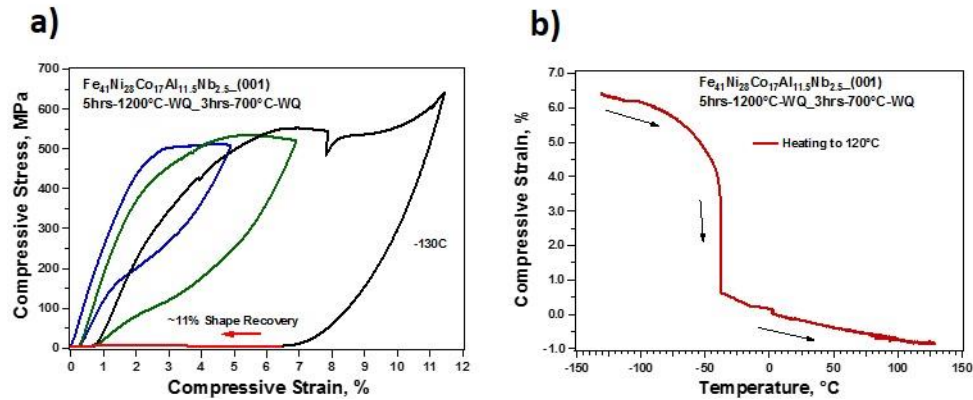
Figure 7.6 a) Compressive response of [001]-oriented and 700 °C-3h aged FeNiCoAlNb single crystal at -130 °C b) Heating curve up to 120 °C after the deformation at -130 °C

Figure 7.7 a and b show the superelastic responses of 700-3h aged samples at selected temperatures in tension and compression, respectively. In tension, perfect superelasticity with low stress hysteresis is observed from -130 °C to -20 °C under stress levels reaching to 900 MPa. In compression, superelasticity is also observed for a large temperature window but at high temperatures, there is some retained strain upon unloading. Stress hysteresis in compression is higher than the stress hysteresis observed tension. It should also be noted that stress hysteresis is strain dependent in compression while it is stress-independent in tension. It is clear that superelasticity is observed for a very large temperature window of about 150 °C in both cases.
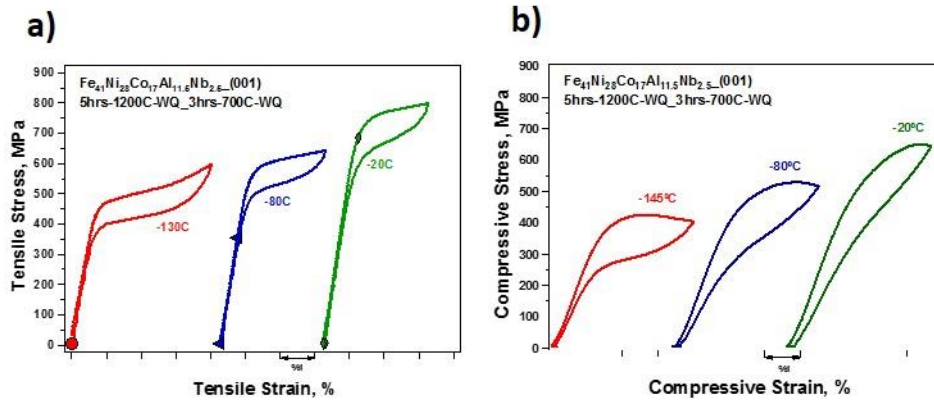
Figure 7.7 Superelastic responses of [001]-oriented and 700 °C-3h aged FeNiCoAlNb single crystal at selected temperatures in a) tension and b) compression.

7.4.2 Thermal Cycling Under Compressive Stress

Figure 7.8 a and b illustrates the thermal cycling under stress responses of 700 ˚C-30m aged FeNiCoAlNb single crystals along the [001] orientation. Since transformation temperatures are low and critical stress for transformation does not change significantly with temperature, high stress levels are applied. The compressive stress of 800 MPa was isothermally applied when the material was austenite at room temperature (1 to 2) and then the sample was cooled to – 100 ˚C (2 to 5) to observe forward transformation. Explosive type phase transformation with strain of 9 % was obtained around – 60 ˚C during cooling. (3 to 4). Unloading the specimen from 800 MPa to 5 MPa at -100 ˚C resulted in back transformation with recovery strain of 5 % (5 to 6). In order to determine the recovery caused by back transformation, the specimen was heated up to 30 ˚C (6 to 8). Explosive type back transformation with strain of 4 % occurred at 10 ˚C (7 to 8). During the thermal cycling, recoverable strain of 13.6 % and irrecoverable strain of 0.6 % were determined.
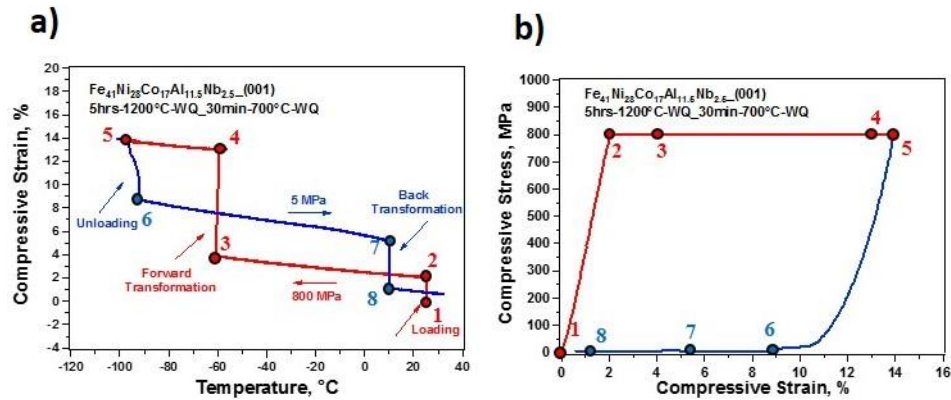
Figure 7.8 a) Thermal cycling response of [001]-oriented and 700 ˚C -30 min aged FeNiCoAlNb single crystal in b) Stress vs strain curve of thermal cycling

7.4.3 Failure Test

Figure 7.9 shows the compression response of aged (600 ˚C-15h) and trained FeCoNiAlNb alloy along the [001] orientation at room temperature. The specimen was initially trained by conducting superelasticity experiments at various temperature from -130 ˚C to room temperature. The alloy shows stress induced phase transformation to martensite at around 1200 MPa and fails at 3200 MPa after ~20 % compressive deformation. Its elastic modulus was determined to be 40 GPa and its elastic modulus to yield strength ratio (E/σ_y) is calculated, to be 12.5. The low ratio indicates that the alloy's actual strength is closer to its theoretical strength. The stress required for plastic deformation (3 GPa) is truly remarkable and higher than most of the high strength steels.
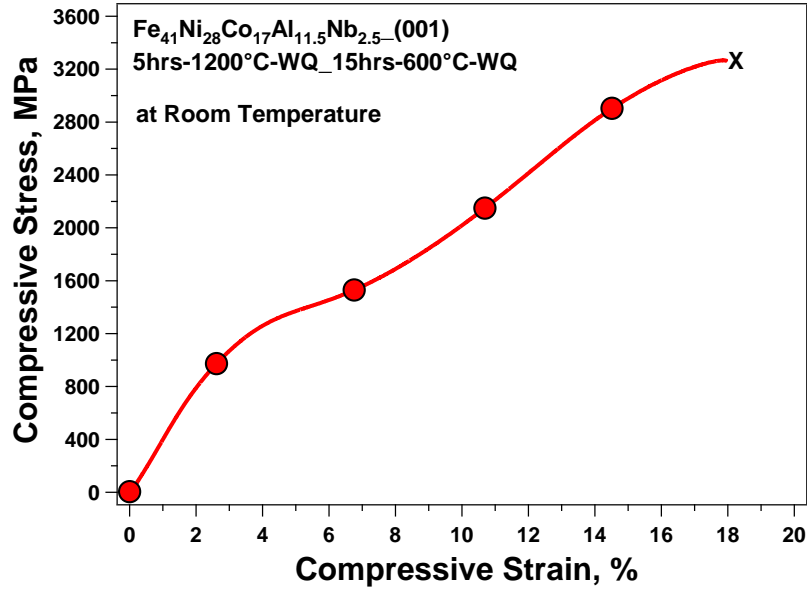
Figure 7.9 Compressive response of aged and trained [100] oriented

FeCoNiAlNb alloy at room temperature

7.5   Orientation Dependence

Effects of orientation on the mechanical properties of FeNiCoAlNb single crystals

along the [001], [110], [012], and [113] orientations were investigated under compressive

stress, as shown figure 7.10. Each specimen was aged at 700 ˚C for 30min and quenched

in water after the homogenization. The specimens were loaded until failure at -100 ˚C. The

critical stress of martensitic transformation in [110] oriented alloy is high at around 1210

MPa compared with critical stress of 705 MPa in [001] oriented specimen. [001] and [113]

oriented specimens exhibited better ductility with deformation of 19.8 % and 23.4 % than

[110] and [012] oriented specimens with deformation of 11.8 % and 13.5 %, respectively.
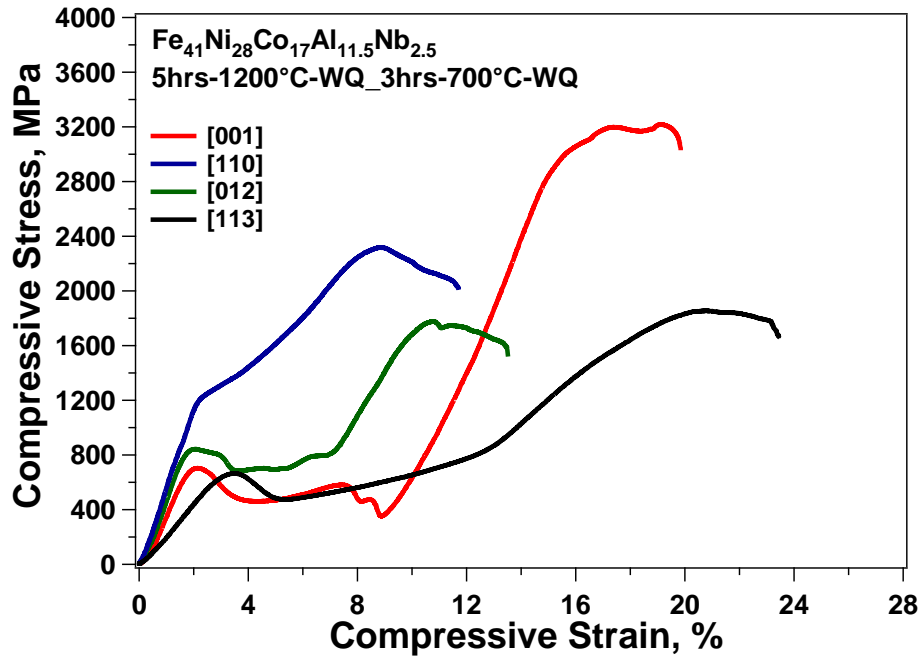
Figure 7.10 Failure test of FeNiCoAlNb along the [001], [110], [012] and [113] orientations for tension and compression

Figure 7.11 shows the compressive superelastic response of FeNiCoAlNb single crystals along the [001] orientation at -60 °C under 0 and 9 T. The magnetic field was applied parallel to the compressive stress direction and was maintained to remain constant during compressive loading and unloading. Compressive stress was applied until it reached a strain of 3.5 % and then unloaded. It is clear that the superelastic loops shifted to lower stress levels with magnetic field. In other words, a decrease in critical stress for transformation was observed with applied magnetic field while the hysteresis was not affected. Magnetostress of 23 MPa was obtained under 9 T magnetic field.
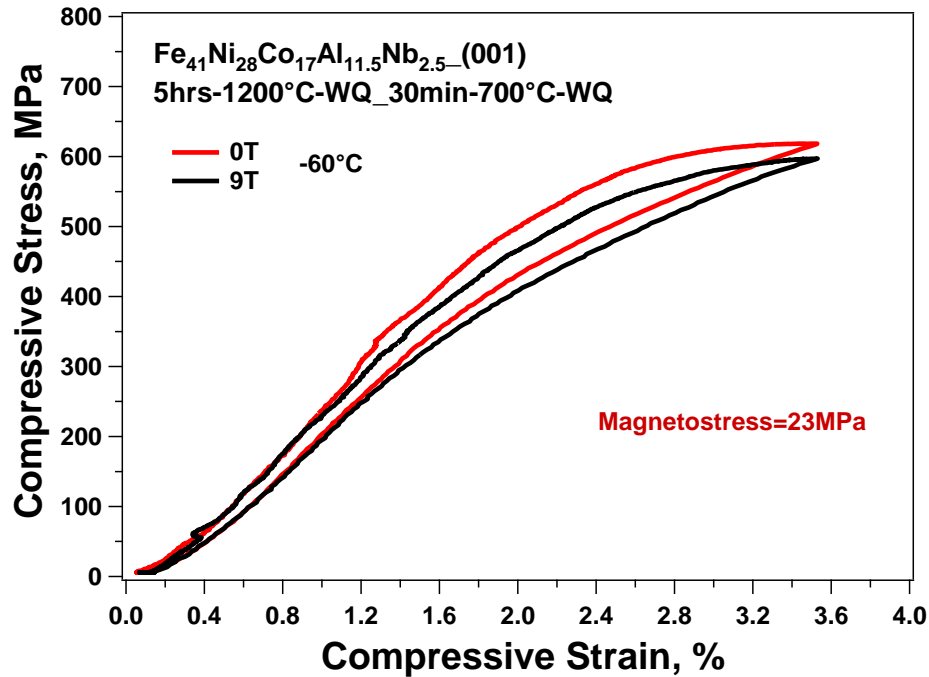
Figure 7.11 Superelastic behavior of [001]-oriented FeNiCoAlNb single crystal

under selected magnetic fields

7.5.1   Theoretical Calculation of Transformation Strain and Phase Diagram

It is well-known that transformation strain of SMAs is strongly dependent on the

lattice parameters of transforming phases. Transformation strains can be theoretically

estimated by the Energy Minimization [113] and the Lattice Deformation Theories [114].

The energy minimization theory considers the existence of the invariant plane (habit plane)

between austenite and martensite phases. The martensite plates consist of twin-related

correspondence variants pairs (CVPs) to form habit planes. In the energy minimization

theory, active CVPs are selected depending on the resolved shear stress on the most

favorable CVPs under stress. The details of the calculation procedure of transformation

strains can be found in work done by Sehitoglu et al. [115].

For [001] orientation, the CVP and single variant (detwinned CVP) strains were both calculated to be 8.31 % in tension by using the Energy Minimization Theory. In compression, the CVP and detwinned CVP strains were determined to be 7.9 % and 14.3 %, respectively.

The lattice deformation theory does not consider the existence of habit planes. The theory assumes that the austenite transforms into a single crystal of martensite without twins. The transformation strain along the [001] orientation can be calculated in compression and tension as:

$$\varepsilon^C = \frac{(\sqrt{2} \times c) - a_0}{a_0} \times 100 = -15.5 \% \text{ and } \varepsilon^T = \frac{c - a_0}{a_0} \times 100 = 8.3 \%$$

The calculated compression strain is in good agreement with the experimental findings shown in Figure 7.5.

Table 7.1 shows CVP, CVP and detwin and single variant strain of FeNiCoAlNb along the [001], [110], [012] and [113] orientations for tension and compression. Single variant strain of [113] orientation was calculated as 6.4 % where it is 8.3 % and same for other orientations under tension. In compression, single variant strain of [012] and [113] orientations exhibited around 10 %, which is lower than [001] orientation (15.5 %) and much higher than [110] orientation (2.8 %). Failure test (figure 7.10) provided deformation behavior of each orientation in terms of maximum capable of strain. Single variant strain of [001], [110], [012] and [113] was measured by excluding the elastic strain from the figure 7.10 as 8.7 %, 2.6 %, 5.6 % and 9.2 %, respectively. Values of single variant strain do not match, but the tendency of the deformation behaviors were close. For instance, [110]

orientation presented the lowest strain compare to other orientations from theoretical and experimental results.

Table 7.1 Theoretically calculated strain of FeNiCoAlNb along the [001], [110], [012] and [113] orientations for tension and compression

	Crystal Orientation	CVP Strain	CVP and Detwin Strain	Single Variant Strain
Tension	[001]	8.7	8.7	8.3
	[011]	4.2	8.7	8.3
	[012]	6.9	8.7	8.3
	[113]	6.6	6.6	6.4
Compression	[001]	7.9	14.3	15.5
	[011]	5.3	2.8	2.8
	[012]	7.4	9.7	10.2
	[113]	6.4	10.1	10.7

From Figure 7.7, it can be observed that the critical stress for transformation increases linearly with temperature in both compression and tension. The C-C slopes of [001]-oriented FeNiCoAlNb single crystals are determined to be 2.8 and 1.4 MPa/°C in tension and compression, respectively. It should be noted that C-C slope is inversely proportional to transformation strain. Thus, it is expected that transformation strain of tension should be half of the transformation strain in compression. This is in good agreement with the theoretical findings where the transformation strain was calculated to be 8.5% in tension and 15.5% in compression.

Figure 7.12 shows the critical stress for transformation as a function of temperature of FeNiCoAlNb in tension and compression. For comparison, the C-C curves of selected alloys are also added. The C-C slope of FeNiCoAlNb is 1.4-2.8 MPa/°C which is lower than the C-C slopes of NiTi (12 MPa/°C in compression and 8 MPa/°C in tension), comparable to FeNiCoAlTa (3.1 MPa/°C) and higher than (0.5 MPa/°C) alloys [54, 57, 116]. Low C-C is useful for applications that require stable superelastic behavior for a large temperature window. [001]-oriented FeNiCoAlNb alloys provides large strain, low C-C slope and large superelastic temperature window that would be very beneficial for actuator applications
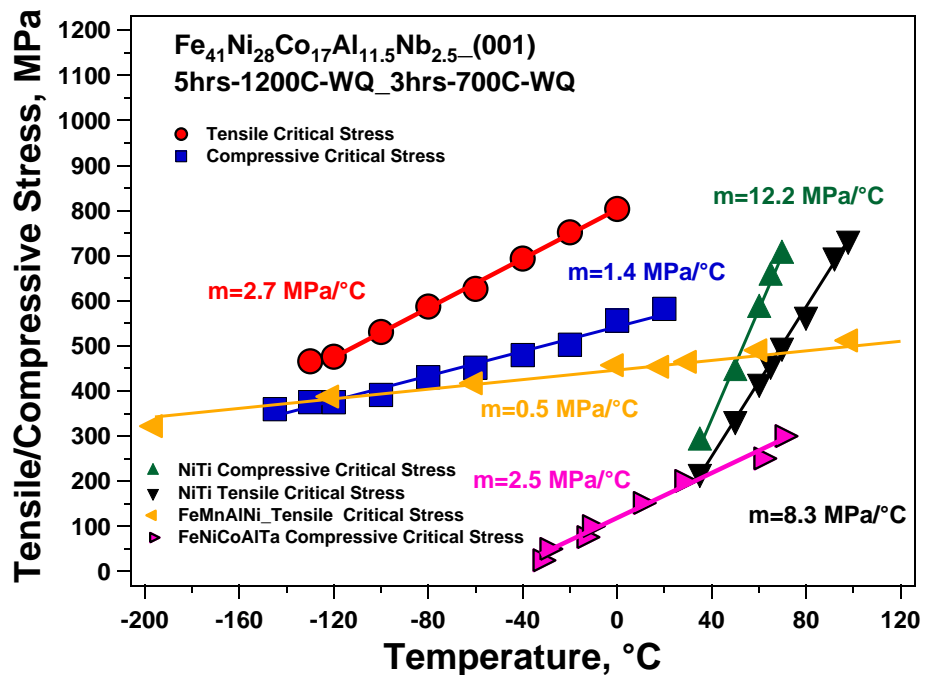
Figure 7.12 The critical stress for transformation as a function of temperature of FeNiCoAlNb in tension and compression. For comparison, the C-C curves of NiTi, FeMnAlNi and FeNiCoAlTa are added.

It should be noted that in Figure 7.6, there is a stress drop during loading at around 7.5 % compressive strain. Additionally, during heating, the remained strain is recovered very steeply at around -40 ˚C. This behavior could be attributed to the burst-type transformation. Since loading was done with strain control, the grips do not allow the fast transformation and applied force drops since the stress needed to nucleate the transformation is less than the stress needed to move the phase front. Another possibility for the load drop might be the fact that the stress required to detwin the martensite variants might be less than the stress required to form CVPs. As it was mentioned before that according to the energy minimization theory, the CVP strain along the [001] orientation is 7.9 % in compression that corresponds to the strain where the load drop is observed. The third and the least likely possibility for the load drop could stem from the multi-phase transformation where austenite might transform to one type of martensite and then that formed martensite might undergo intermartensitic transformation.

Although single crystals along the [100] orientation of FeCoNiAlNb alloys are used in this study, it is well known that polycrystals can be textured to mimic their single crystalline behavior. Previously, FeNiCoAlTaB was cold rolled to have a texture along the [100] orientation to show good superelasticity. Therefore, it is expected that polycrystalline of FeCoNiAlNb alloys can also be textured to mimic the results presented here.

Ferrous FeCoNiAlNb alloys have many advantages when they are compared to NiTi alloys. FeCoNiAlNb alloys have low temperature dependent superelastic behavior, higher strain and strength than NiTi alloys. They can be used as inexpensive replacement of NiTi alloys for large scale applications or utilized as compact actuators. Their ultra high

strength can make these alloys suitable for applications in extreme environments such as oil and gas industry applications. Although it has not been focused in this study, in general, high strength is associated with longer fatigue life that is useful for cyclic applications.

The main disadvantage of FeCoNiAlNb alloys is the low transformation temperatures. However, it should be noted that shape memory properties of FeCoNiAlNb alloys can be adjusted with aging treatments and composition alterations. Keeping this in mind, in the future, composition and thermomechanical treatments can be optimized to use these alloys at higher temperature ranges.

7.6 Conclusions

In this chapter, mechanical and magnetic properties of FeCoNiAlNb single crystals were investigated. Important results are summarized below:

1. XRD and TEM results showed that crystal structure of austenite was (γ, FCC) at room temperature and crystal structure of precipitates (γ', $L1_2$) of about 5 nm in diameter were formed in the matrix. Crystal structure of martensite was found (α', BCT). The lattice parameters of γ and α' phases were determined as a_0=0.3625nm, a=0.2761 nm and c=0.3047nm at room temperature.

2. Martensite phase presented higher magnetization than austenite as opposed to NiMn-based metamagnetic shape memory alloys.

3. Recoverable strain of 14 % was determined from superelasticity test at -100 ˚C in the [001] oriented specimen aged at 700 ℃ for 30min. Single variant strain was calculated theoretically as 15. 5% under compression and had good agreement with experimental findings. Mechanical hysteresis increased as a function of strain.

4. FeNiCoAlNb alloys presents 11% shape recovery in compression and perfect superelasticity (4%) at various temperatures in tension and compression, due to thermoelastic martensitic transformation in the [001] oriented specimen aged at 700 °C for 3h. Moreover, FeNiCoAlNb ferromagnetic shape memory alloys exhibit low C-C slope (1.4 MPa/°C) in compression, and 2.7 MPa/°C in tension which provides high SE temperature intervals.

5. FeNiCoAlNb single crystals along the [001] orientation showed ultra high strength with failure stress of 3 GPa.

6. Orientation dependence on mechanical properties were explored. The critical stress of martensitic transformation in [110] oriented alloy is the highest of around 1210 MPa at room temperature. [001] and [113] oriented specimens exhibited better ductility than [110] and [012] oriented specimens.

7. Superelasticty under magnetic field was performed. Critical stress was shifting down with applied magnetic field of 9 T. Magnetostress of 23 MPa was obtained at -100 °C

8   Conclusions and Future Work

Metamagnetic shape memory alloys have been widely investigated for actuators and sensors applications due to large magnetic field induced strain and high output stress. Effects of magnetic field on superelasticity and shape memory effect on single and polycrystalline metamagnetic shape memory alloys were explored in this study.

Effects of heat treatment temperature and cooling rate on shape memory behavior such as transformation temperatures, magnetic and mechanical properties in [001] oriented NiMnCoIn single crystalline metamagnetic shape memory alloys were investigated. Transformation temperatures were decreased drastically by changing cooling rate from water quenching to furnace cooling. Transformation temperatures were increased with increasing heat treatment temperature and saturated. Heat treatment at 600 °C for 3 hours, followed by water quenching, decreased the temperature hysteresis around 34 °C under 25 MPa. Applied magnetic field of 7 T recovered strain of 3.8 % after the deformation of martensite at 10 °C. Back transformation started at 2.6 T and recovery completed at 4.2 T. 1.5 % magnetic field induced reversible strain was obtained under 90 MPa. Reversible MFIS of 1.5 % is five times higher than achievement of previous studies in magnetic shape memory alloys. Furthermore, M_s decreased 39 °C with applied magnetic field of 9 T under 25 MPa compressive stress.

The effects of the magnetic field on the shape memory behavior of [001]-oriented metamagnetic NiMnCoIn shape memory single crystals were investigated. Thermal cycling under constant stress and magnetic field, and superelasticity under constant magnetic field tests were conducted to understand their magneto-thermo-mechanical behavior. Magnetostress of 85 MPa was determined in superelasticity experiment at 90 °C

under 9 T. In addition, stress-temperature phase diagrams were created under magnetic field. The decreased of M_s was calculated theoretically and showed good agreement in experimental data. In addition, superelasticity as a function temperature and magnetic field were conducted. Large magnetostress of 160 MPa was obtained in NiMnCoIn single crystal along the [110] orientation in superelasticity experiment at 90 °C. Also, M_s decreased 29 °C with applied magnetic field of 9 T during thermal cycling under 1500 MPa. In [111] orientation, magnetostress of 106 MPa was determined at 90 °C under magnetic field of 9 T. M_s decreased about 15 °C under 400 MPa.

The effects of quaternary element, Co, addition to polycrystalline NiMnGa alloys on their magnetic and shape memory properties have been investigated. NiCoMnGa polycrystalline alloys have displayed good shape memory and superelasticity behavior under compression at temperatures above 100 °C with about 3% transformation strain and low temperature hysteresis. It is also possible to train the material to demonstrate large two-way shape memory effect. Transformation temperatures decreased by 5 °C with applied magnetic field of 9 T under 50 MPa in poly-crystalline form. Polycrystalline of NiMnCoGa can be used as a high temperature magnetic actuator.

Magnetic Shape memory properties of $Mn_{49}Ni_{42}Sn_9$ and $Mn_{49}Ni_{39}Sn_9Fe_3$ polycrystalline alloys were also characterized under compressive stress and magnetic field where ferromagnetic austenite transforms to weakly magnetic martensite. Magnetization difference between the transforming phases increased drastically while transformation temperature decreased with Fe addition. $Mn_{49}Ni_{42}Sn_9$ and $Mn_{49}Ni_{39}Sn_9Fe_3$ alloys presented perfect superelastic response with recoverable strain of 4 % and 3.5 % under compression

at room temperature in polycrystalline form. $Mn_{49}Ni_{39}Sn_9Fe_3$ exhibited a high magnetostress of 27 MPa under 9 Tesla.

The shape memory properties of a ferrous single crystalline alloy, FeNiCoAlNb, are investigated along the [100] orientation by thermal cycling under constant stress and superelasticity tests in both tension and compression. Aging was used to form nano-size precipitates to demonstrate shape memory behavior and tailor the shape memory properties. It was found that after proper heat treatments, [011] oriented FeNiCoAlNb show compressive strain of 15 %, low temperature dependent superelastic behavior, high compression-tension asymmetry and high compressive strength (~3 GPa). This ferrous alloy has great potential for high strength, temperature independent and large scale actuator applications. In order to reveal ductility and strength, a failure test was conducted at room temperature. The critical stress of martensitic transformation in [110] oriented alloy is high around 1210 MPa compared with critical stress of 705 MPa in [001] oriented specimen. [001] and [113] oriented specimens exhibited better ductility than [110] and [012] oriented specimens. Magnetization of martensite was higher than parent phase; however, both phase were ferromagnetic. Superelasticty under magnetic field was performed and magnetostress of 23 MPa was obtained at -100 °C

In this study, effect of magnetic field on shape memory behavior were mainly investigated in NiMnCoIn and FeNiCoAlNb single crystals and NiMnCoGa and MnNiSnFe polycrystalline. According to results of this study, future study plan would be:

1. Explore energy harvesting potential of NiMnCoIn and other metamagnetic shape memory alloys

2. Determine magnetic field induced stress generation of NiMnCoIn alloys by using displacement control after pre-strain

3. Characterize magnetic field induced forward transformation in FeNiCoAlNb single crystalline and orientation dependence on magnetostress

4. Search new metamagnetic alloy system which has high magnetization difference between transforming phase, low hysteresis and ductile in polycrystalline form

References

[1] T. Duerig, A. Pelton, D. Stöckel, Materials Science and Engineering: A, 273 (1999) 149-160.

[2] N. Morgan, Materials Science and Engineering: A, 378 (2004) 16-23.

[3] G. Song, N. Ma, H.-N. Li, Engineering Structures, 28 (2006) 1266-1274.

[4] Y. Fu, H. Du, W. Huang, S. Zhang, M. Hu, Sensors and Actuators A: Physical, 112 (2004) 395-408.

[5] R.D. James, M. Wuttig, Philosophical Magazine A, 77 (1998) 1273-1299.

[6] R.C. OHandley, Journal of Applied Physics, 83 (1998) 3263-3270.

[7] A. Sozinov, A. Likhachev, N. Lanska, K. Ullakko, Applied Physics Letters, 80 (2002) 1746-1748.

[8] K. Ullakko, J. Huang, C. Kantner, R. O'handley, V. Kokorin, Applied Physics Letters, 69 (1996) 1966.

[9] H. Karaca, I. Karaman, B. Basaran, Y. Chumlyakov, H. Maier, Acta Materialia, 54 (2006) 233-245.

[10] H. Karaca, I. Karaman, B. Basaran, D. Lagoudas, Y. Chumlyakov, H. Maier, Scripta materialia, 55 (2006) 803-806.

[11] H. Karaca, I. Karaman, B. Basaran, D. Lagoudas, Y. Chumlyakov, H. Maier, Acta materialia, 55 (2007) 4253-4269.

[12] H.E. Karaca, I. Karaman, B. Basaran, Y. Ren, Y.I. Chumlyakov, H.J. Maier, Advanced Functional Materials, 19 (2009) 983-998.

[13] J.-h. Kim, T. Fukuda, T. Kakeshita, Scripta materialia, 54 (2006) 585-588.

[14] I. Karaman, H. Karaca, B. Basaran, D. Lagoudas, Y. Chumlyakov, H. Maier, Scripta materialia, 55 (2006) 403-406.

[15] H.E. Karaca, B. Basaran, I. Karaman, Y.I. Chumlyakov, Smart Mater. Struct., 21 (2012) 9.

[16] K. Oikawa, W. Ito, Y. Imano, Y. Sutou, R. Kainuma, K. Ishida, S. Okamoto, O. Kitakami, T. Kanomata, Applied Physics Letters, 88 (2006) 122507-122507.

[17] K. Koyama, K. Watanabe, T. Kanomata, R. Kainuma, K. Oikawa, K. Ishida, Applied physics letters, 88 (2006) 132505-132505-132503.

[18] S. Yu, L. Ma, G. Liu, Z. Liu, J. Chen, Z. Cao, G. Wu, B. Zhang, X. Zhang, Applied physics letters, 90 (2007) 242501-242501-242503.

[19] R. Kainuma, Y. Imano, W. Ito, Y. Sutou, H. Morito, S. Okamoto, O. Kitakami, K. Oikawa, A. Fujita, T. Kanomata, Nature, 439 (2006) 957-960.

[20] T. Krenke, E. Duman, M. Acet, E.F. Wassermann, X. Moya, L. Mañosa, A. Planes, E. Suard, B. Ouladdiaf, Physical Review B, 75 (2007) 104414.

[21] J. Liu, S. Aksoy, N. Scheerbaum, M. Acet, O. Gutfleisch, Applied Physics Letters, 95 (2009) 232515.

[22] F.G. R. Kainuma, Y. Sutou, I. Ohnuma, K. Ishida, Materials Transactions, JIM, 41 (2000) 943-949.

[23] W. Ito, M. Nagasako, R. Umetsu, R. Kainuma, T. Kanomata, K. Ishida, Applied Physics Letters, 93 (2008) 232503-232503-232503.

[24] S. Kustov, M. Corró, J. Pons, E. Cesari, Applied Physics Letters, 94 (2009) 191901.

[25] V. Sánchez-Alarcos, V. Recarte, J.I. Pérez-Landazábal, E. Cesari, J.A. Rodríguez-Velamazán, Entropy, 16 (2014) 2756-2767.

[26] J. Pérez-Landazábal, V. Recarte, V. Sánchez-Alarcos, C. Gómez-Polo, E. Cesari, Applied Physics Letters, 102 (2013) 101908.

[27] F. Chen, H. Wang, Y. Zheng, W. Cai, L. Zhao, Journal of materials science, 40 (2005) 219-221.

[28] A. Cherechukin, I. Dikshtein, D. Ermakov, A. Glebov, V. Koledov, D. Kosolapov, V. Shavrov, A. Tulaikova, E. Krasnoperov, T. Takagi, Physics Letters A, 291 (2001) 175-183.

[29] H. Karaca, A. Turabi, B. Basaran, A. Pathak, I. Dubenko, N. Ali, Y. Chumlyakov, P. Li, Journal of Materials Engineering and Performance, (2013) 1-4.

[30] Y. Ma, S. Yang, Y. Liu, X. Liu, Acta Materialia, 57 (2009) 3232-3241.

[31] J. Wang, C. Jiang, Scripta Materialia, 62 (2010) 298-300.

[32] Y. Aydogdu, A.S. Turabi, M. Kok, A. Aydogdu, H. Tobe, H.E. Karaca, Applied Physics A, 117 (2014) 2073-2078.

[33] S. Fabbrici, F. Albertini, A. Paoluzi, F. Bolzoni, R. Cabassi, M. Solzi, L. Righi, G. Calestani, Applied Physics Letters, 95 (2009).

[34] V. Sanchez-Alarcos, J.I. Perez-Landazabal, V. Recarte, C. Gomez-Polo, J.A. Rodriguez-Velamazan, Acta Materialia, 56 (2008) 5370-5376.

[35] K. Oikawa, T. Ota, F. Gejima, T. Ohmori, R. Kainuma, K. Ishida, Materials Transactions, 42 (2001) 2472-2475.

[36] K. Oikawa, L. Wulff, T. Iijima, F. Gejima, T. Ohmori, A. Fujita, K. Fukamichi, R. Kainuma, K. Ishida, Applied Physics Letters, 79 (2001) 3290-3292.

[37] K. Oikawa, T. Ota, T. Ohmori, Y. Tanaka, H. Morito, A. Fujita, R. Kainuma, K. Fukamichi, K. Ishida, Applied Physics Letters, 81 (2002) 5201-5203.

[38] G. Liu, J. Chen, Z. Liu, X. Dai, G. Wu, B. Zhang, X. Zhang, Applied Physics Letters, 87 (2005) 262504-262504-262503.

[39] H. Xuan, Q. Cao, C. Zhang, S. Ma, S. Chen, D. Wang, Y. Du, Applied Physics Letters, 96 (2010) 202502-202502-202503.

[40] H. Xuan, S. Ma, Q. Cao, D. Wang, Y. Du, Journal of Alloys and Compounds, 509 (2011) 5761-5764.

[41] Z. Wu, Z. Liu, H. Yang, Y. Liu, G. Wu, Applied Physics Letters, 98 (2011) 061904.

[42] S. Kajiwara, T. Kikuchi, Acta Metall Mater, 38 (1990) 847-855.

[43] A. Sato, E. Chishima, Y. Yamaji, T. Mori, Acta Metallurgica, 32 (1984) 539-547.

[44] A. Sato, E. Chishima, K. Soma, T. Mori, Acta Metallurgica, 30 (1982) 1177-1183.

[45] K. Ando, T. Omori, I. Ohnuma, R. Kainuma, K. Ishida, Applied Physics Letters, 95 (2009).

[46] O.M. Shevchenko, G.V. Gavrilyuk, V.V. Kokorin, V.A. Chernenko, Powder Metall Met C+, 36 (1997) 71-76.

[47] T. Maki, K. Kobayashi, M. Minato, I. Tamura, Scripta Metallurgica, 18 (1984) 1105-1109.

[48] T. Kakeshita, K. Shimizu, T. Maki, I. Tamura, S. Kijima, M. Date, Scripta Metallurgica, 19 (1985) 973-976.

[49] V.V. Kokorin, L.P. Gunko, O.M. Shevchenko, Scr. Metall. Materialia, 28 (1993) 35-40.

[50] H. Sehitoglu, I. Karaman, X.Y. Zhang, Y. Chumlyakov, H.J. Maier, Scripta Materialia, 44 (2001) 779-784.

[51] E. Hornbogen, N. Jost, J. Phys. IV, 1 (1991) 199-210.

[52] H. Sehitoglu, X.Y. Zhang, T. Kotil, D. Canadinc, Y. Chumlyakov, H.J. Maier, Metallurgical and Materials Transactions A: Physical Metallurgy and Materials Science, 33 (2002) 3661-3672.

[53] Y. Tanaka, Y. Himuro, R. Kainuma, Y. Sutou, T. Omori, K. Ishida, Science, 327 (2010) 1488-1490.

[54] T. Omori, K. Ando, M. Okano, X. Xu, Y. Tanaka, I. Ohnuma, R. Kainuma, K. Ishida, Science, 333 (2011) 68-71.

[55] I.V. Kireeva, Y.I. Chumlyakov, V.A. Kirillov, I. Karaman, E. Cesari, Tech Phys Lett+, 37 (2011) 487-490.

[56] I.V. Kireeva, Y.I. Chumlyakov, V.A. Kirillov, I.V. Kretinina, Y.N. Danil'son, I. Karaman, E. Cesari, Russ Phys J+, 53 (2011) 1103-1106.

[57] J. Ma, B. Kockar, A. Evirgen, I. Karaman, Z.P. Luo, Y.I. Chumlyakov, Acta Materialia, 60 (2012) 2186-2195.

[58] A. Evirgen, J. Ma, I. Karaman, Z. Luo, Y. Chumlyakov, Scripta Materialia, 67 (2012) 475-478.

[59] T. Omori, S. Abe, Y. Tanaka, D.Y. Lee, K. Ishida, R. Kainuma, Scripta Materialia, 69 (2013) 812-815.

[60] J. Ma, I. Karaman, R.D. Noebe, Int. Mater. Rev., 55 (2010) 257-315.

[61] G. Park, M.T. Bement, D.A. Hartman, R.E. Smith, C.R. Farrar, International Journal of Machine Tools and Manufacture, 47 (2007) 2189-2206.

[62] J. Fan, W. Stoll, C. Lynch, Acta materialia, 47 (1999) 4415-4425.

[63] J. Li, R. Rogan, E. Üstündag, K. Bhattacharya, Nature materials, 4 (2005) 776-781.

[64] M. Wun-Fogle, J. Restorff, K. Leung, J. Cullen, A. Clark, Magnetics, IEEE Transactions on, 35 (1999) 3817-3819.

[65] P.K. Kumar, D.C. Lagoudas, Introduction to Shape Memory Alloys, Shape Memory Alloys, Springer US, 2008, pp. 1-51.

[66] K. Otsuka, C.M. Wayman, Shape memory materials, Cambridge university press, 1999.

[67] P. Wollants, J. Roos, L. Delaey, Progress in Materials Science, 37 (1993) 227-288.

[68] E. Panchenko, Y. Chumlyakov, I. Kireeva, A. Ovsyannikov, H. Sehitoglu, I. Karaman, Y. Maier, The Physics of Metals and Metallography, 106 (2008) 577-589.

[69] K. Otsuka, X. Ren, Progress in materials science, 50 (2005) 511-678.

[70] H. Sehitoglu, C. Efstathiou, H.J. Maier, Y. Chumlyakov, Mechanics of Materials, 38 (2006) 538-550.

[71] R.F. Hamilton, H. Sehitoglu, Y. Chumlyakov, H.J. Maier, Acta Materialia, 52 (2004) 3383-3402.

[72] K. Kus, T. Breczko, Materials Physics and Mechanics, 9 (2010).

[73] G. Della Gatta, M.J. Richardson, S.M. Sarge, S. Stølen, Pure and applied chemistry, 78 (2006) 1455-1476.

[74] O. Benafan, R. Noebe, S. Padula II, A. Garg, B. Clausen, S. Vogel, R. Vaidyanathan, International Journal of Plasticity, 51 (2013) 103-121.

[75] A. Sozinov, A.A. Likhachev, N. Lanska, K. Ullakko, V.K. Lindroos, Proceedings of SPIE, 2002, pp. 195-205.

[76] C. Henry, D. Bono, J. Feuchtwanger, S. Allen, R. OHandley, Journal of Applied Physics, 91 (2002) 7810-7811.

[77] S.J. Murray, M. Marioni, S. Allen, R. O'handley, T. Lograsso, Applied Physics Letters, 77 (2000) 886.

[78] M. Marioni, R. O'Handley, S. Allen, S. Hall, D. Paul, M. Richard, J. Feuchtwanger, B. Peterson, J. Chambers, R. Techapiesancharoenkij, Journal of Magnetism and Magnetic Materials, 290 (2005) 35-41.

[79] P. Müllner, V. Chernenko, G. Kostorz, Journal of Magnetism and Magnetic Materials, 267 (2003) 325-334.

[80] T. Kakeshita, T. Takeuchi, T. Fukuda, M. Tsujiguchi, T. Saburi, R. Oshima, S. Muto, Applied Physics Letters, 77 (2000) 1502.

[81] S. Muto, R. Oshima, F.E. Fujita, Scripta metallurgica, 21 (1987) 465-468.

[82] H. Karaca, I. Karaman, Y. Chumlyakov, D. Lagoudas, X. Zhang, Scripta Materialia, 51 (2004) 261-266.

[83] H. Karaca, I. Karaman, D. Lagoudas, H. Maier, Y. Chumlyakov, Scripta Materialia, 49 (2003) 831-836.

[84] K. Oikawa, T. Ota, Y. Imano, T. Omori, R. Kainuma, K. Ishida, Journal of Phase Equilibria and Diffusion, 27 (2006) 75-82.

[85] Y. Liu, W. Zhou, X. Qi, B. Jiang, W. Wang, J. Chen, G. Wu, J. Wang, C. Feng, H. Xie, Applied Physics Letters, 78 (2001) 3660-3662.

[86] K. Oikawa, T. Ota, Y. Sutou, T. Ohmori, R. Kainuma, K. Ishida, Materials Transactions, 43 (2002) 2360-2362.

[87] Y. Imano, T. Omori, K. Oikawa, Y. Sutou, R. Kainuma, K. Ishida, Materials Science and Engineering: A, 438 (2006) 970-973.

[88] L. Straka, O. Heczko, K. Ullakko, Journal of Magnetism and Magnetic Materials, 272 (2004) 2049-2050.

[89] O. Heczko, L. Straka, S.-P. Hannula, Materials Science and Engineering: A, 438 (2006) 1003-1006.

[90] A.K. Pathak, B.R. Gautam, I. Dubenko, M. Khan, S. Stadler, N. Ali, Journal of Applied Physics, 103 (2008) 07F315.

[91] V. Sharma, M. Chattopadhyay, K. Shaeb, A. Chouhan, S. Roy, Applied Physics Letters, 89 (2006) 222509-222509-222503.

[92] B. Wang, Y. Liu, L. Wang, S. Huang, Y. Zhao, Y. Yang, H. Zhang, Journal of Applied Physics, 104 (2008) 043916-043916-043914.

[93] S. Yu, Z. Liu, G. Liu, J. Chen, Z. Cao, G. Wu, B. Zhang, X. Zhang, Applied Physics Letters, 89 (2006) 162503-162503-162503.

[94] J. Du, Q. Zheng, W. Ren, W. Feng, X. Liu, Z. Zhang, Journal of Physics D: Applied Physics, 40 (2007) 5523.

[95] P. Bhobe, K. Priolkar, A. Nigam, Applied Physics Letters, 91 (2007) 242503-242503-242503.

[96] Z. Han, D. Wang, C. Zhang, S. Tang, B. Gu, Y. Du, Applied Physics Letters, 89 (2006) 182507.

[97] Z. Han, D. Wang, C. Zhang, H. Xuan, B. Gu, Y. Du, Applied Physics Letters, 90 (2007) 042507.

[98] Z. Han, D. Wang, C. Zhang, H. Xuan, J. Zhang, B. Gu, Y. Du, Solid State Communications, 146 (2008) 124-127.

[99] T. Krenke, E. Duman, M. Acet, E.F. Wassermann, X. Moya, L. Mañosa, A. Planes, Nature materials, 4 (2005) 450-454.

[100] X. Moya, L. Mañosa, A. Planes, S. Aksoy, M. Acet, E.F. Wassermann, T. Krenke, Physical Review B, 75 (2007) 184412.

[101] A.K. Pathak, I. Dubenko, S. Stadler, N. Ali, Journal of Physics D: Applied Physics, 41 (2008) 202004.

[102] V. Sharma, M. Chattopadhyay, R. Kumar, T. Ganguli, P. Tiwari, S. Roy, Journal of Physics: Condensed Matter, 19 (2007) 496207.

[103] V. Sharma, M. Chattopadhyay, S. Roy, Journal of Physics D: Applied Physics, 40 (2007) 1869.

[104] H. Xuan, D. Wang, C. Zhang, Z. Han, B. Gu, Y. Du, Applied Physics Letters, 92 (2008) 102503-102503-102503.

[105] X. Zhang, B. Zhang, S. Yu, Z. Liu, W. Xu, G. Liu, J. Chen, Z. Cao, G. Wu, Physical Review B, 76 (2007) 132403.

[106] W. Ito, Y. Imano, R. Kainuma, Y. Sutou, K. Oikawa, K. Ishida, Metallurgical and Materials Transactions A, 38 (2007) 759-766.

[107] B. Bilby, A. Crocker, Proceedings of the Royal Society of London. Series A. Mathematical and Physical Sciences, 288 (1965) 240-255.

[108] W. Ito, K. Ito, R.Y. Umetsu, R. Kainuma, K. Koyama, K. Watanabe, A. Fujita, K. Oikawa, K. Ishida, T. Kanomata, Applied Physics Letters, 92 (2008) 021908-021908-021903.

[109] R. Kainuma, Y. Imano, W. Ito, H. Morito, Y. Sutou, K. Oikawa, A. Fujita, K. Ishida, S. Okamoto, O. Kitakami, Applied Physics Letters, 88 (2006) 192513.

[110] S.Y. Yang, Y.Q. Ma, H.F. Jiang, X.J. Liu, Intermetallics, 19 (2011) 225-228.

[111] C. Efstathiou, H. Sehitoglu, A.W. Johnson, R. Hamilton, H. Maier, Y. Chumlyakov, Scripta materialia, 51 (2004) 979-985.

[112] F. Masdeu, J. Pons, R. Santamarta, E. Cesari, J. Dutkiewicz, Materials Science and Engineering: A, 481 (2008) 101-104.

[113] J.M. Ball, R.D. James, Arch. Ration. Mech. Anal., 100 (1987) 13-52.

[114] T. Saburi, S. Nenno, Solid to Solid Phase Transformations, (1981) 1455-1479.

[115] H. Sehitoglu, I. Karaman, R. Anderson, X. Zhang, K. Gall, H.J. Maier, Y. Chumlyakov, Acta Materialia, 48 (2000) 3311-3326.

[116] L. Orgéas, D. Favier, Acta Materialia, 46 (1998) 5579-5591.

VITA

Ali Sadi Turabi was born in 1984 in Amasya, Turkey. He received his bachelor degree from Kocaeli University, Izmit, Turkey. He worked as an engineer on Unmanned Air Vehicle (UAV) Project for a year in KALEKALIP Machinary and Moulding Industry in Turkey. He has been a Ph.D. student at University of Kentucky since 2010. His research area was characterization of magnetic field effect on shape memory alloys in magnetic shape memory alloys. He published two journal papers during his graduate tenure. In addition, he has two journal article under review and four journal articles to be submitted.